Characterization of Cerebral Hemodynamics Using a Computational Fluid Dynamics and Arterial Spin Labeling MRI Strategy: Applications in Cerebrovascular Occlusive Disease

by

Jonas Schollenberger

A dissertation submitted in partial fulfillment
of the requirements for the degree of
Doctor of Philosophy
(Biomedical Engineering)
in the University of Michigan
2021

Doctoral Committee:

Professor C. Alberto Figueroa, Co-Chair
Research Professor Luis Hernandez-Garcia, Co-Chair
Professor Douglas C. Noll
Assistant Professor Nicholas H. Osborne

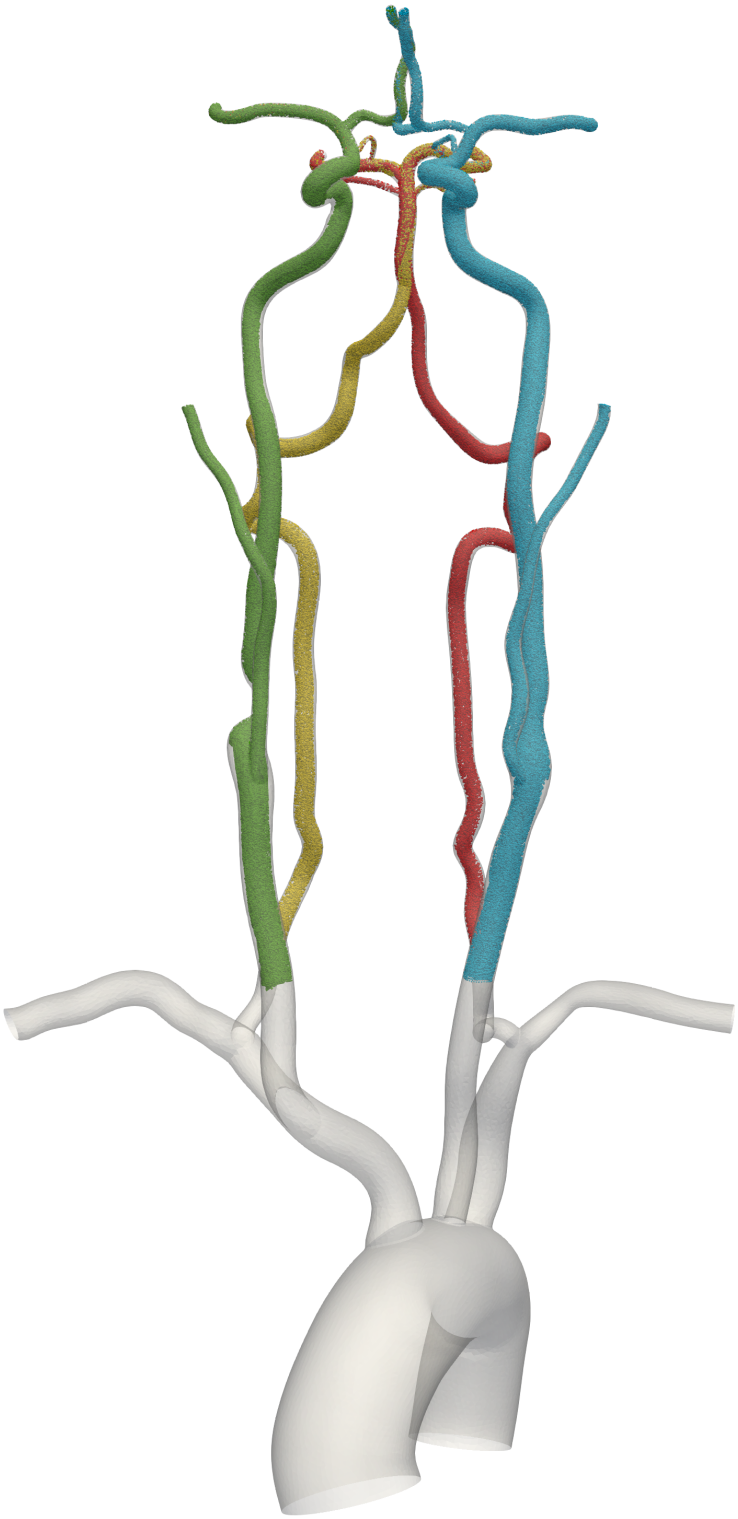

Jonas Schollenberger

scjonas@umich.edu

ORCID iD: 0000-0002-9245-3984

Acknowledgements

I am eternally grateful of the support that I have received from my PhD advisor Prof. Alberto Figueroa. He took a chance on me when I came to Michigan as a visiting scholar during my master's studies in Germany and offered me the opportunity to pursue a PhD. It has been a long journey together since the early days of the Figueroa lab in Michigan. I appreciate all the guidance and insight he has provided me with in my research project. I especially admire his eye for details and his profound understanding for computational modeling of the cardiovascular system. One of the biggest lessons he taught me is the importance of careful and concise scientific communication, especially when presenting the results of research projects. I consider him a mentor and a friend, and I hope to continue our relationship in the future.

I was immensely fortunate to have Prof. Luis Hernandez-Garcia as my co-advisor on this journey. I didn't know much about MRI when I started my PhD and Luis helped me profoundly to succeed with the MRI part of my project. He always had an open door and ear for me when I was stuck. I absolutely admire his creativity and ability to come up with new ideas and solutions for problems. Besides work, Luis has also been a great running mate and friend. But most of all, I want to thank Luis for his never-ending willingness to volunteer for MRI scans whenever I needed a test subject. After all these hours together in the scanner, I feel like I know him inside out, quite literally!

I would like to provide a special thank you to Prof. Nicholas Osborne for being my clinical collaborator and mentor. It is easy to sometimes get lost in the engineering details, but conversations with Nick always helped me to remind me of the clinical importance of my work and to see the bigger picture of my project.

I am grateful to Prof. Douglas Noll for his support and knowledge throughout the years. Doug's immense knowledge and intuition in the field of MRI has been a constant source of inspiration.

I want to give a special thank you to all the past and current members of the Figueroa Lab: Kevin Lau, Nan Xiao, Miquel Aguirre, Federica Cuomo, Sabrina Lynch, Chris Arthurs, Sabrina Ben

Ahmed, Nitesh Nama, Vasilina Filonova, Kritika Iyer, Christopher Tossas, Hamid Gharahi, Jonathan Primeaux, and Sara Hopper. I was very fortunate to be working in such a great lab environment with so many great people who have inspired me, shared laughs with me, and provided me with moral support. I will miss our impromptu lab s'mores, trips up north, and most of all our puzzle sessions.

I want to thank all the clinical members who have joined the Figueroa Lab from the Netherlands over the years: Foeke Nauta, Diederik van Bakel, Ignas Houben, Yunus Ahmed, and Pieter van Bakel. I appreciate all the support and the good times we had together.

I am very grateful to all the members of the fMRI lab, my second home on campus. Thank you to all the past and current graduate students: Sydney Williams, Kathleen Ropella Panagis, Anish Lahiri, Tianrui Luo, Michelle Karker, Shouchang Guo, and Amos Cao. Thank you for all the help and fun moments with had together. I want to give a special thank you to Prof. Jon-Fredrik Nielsen who always had an open door for me and helped me quite a lot with technical questions. I also want to thank all the staff members of the fMRI lab who make research possible: Scott Peltier, Ryan Smith, Dina Salhani, Barb Hibbard, and Krisanne Litinas.

I am very grateful for all the close friendships I have made in Ann Arbor over the years. Thank you Fede, Sydney, Sabrina, Romulo, Jack, Marianna, Rachel, Hamid, Ati, Jonathan, Nitesh, Priya, Hazel, Tyler, Dan, Alex, Megan, James, and many more…thank you so much for your friendship and all the good times we had together. I am looking forward to keeping in touch.

Lastly, I want to thank my family in Germany for all their love and support. I know it has been hard to live 4000 miles apart and in different time zones for all these years. My parents have been my biggest supporters along this journey and have always provided me with encouragement and praise throughout the ups and downs. My brother David has helped to keep me sane and grounded throughout this journey.

Table of Contents

List of Tables

List of Figures

List of Abbreviations

AComA Anterior communicating artery

ASL Arterial spin labeling MRI

CAS Carotid angioplasty with stenting

CEA Carotid endarterectomy

CFD Computational fluid dynamics

CoW Circle of Willis

CTA Computed tomography angiography

CVOD Cerebrovascular occlusive disease

DSA Digital subtraction angiography

DUS Duplex ultrasound

FBS Fractional blood supply

FF Fractional flow index

FFR Fractional flow reserve

LPT Lagrangian particle tracking

NS-ASL Non-selective arterial spin labeling MRI

PC-MRI Phase contrast magnetic resonance imaging

PCASL Pseudo-continuous arterial spin labeling

RACA/LACA Right/left anterior cerebral artery

RICA/LICA Right/left internal carotid artery

RMCA/LMCA Right/left middle cerebral artery

RPCA/LPCA Right/left posterior cerebral artery

RSCA/LSCA Right/left superior cerebellar artery

RVA/LVA Right/left vertebral artery

SNR Signal-to-noise ratio

SS-PCASL Super-selective Pseudo-continuous arterial spin labeling

TCD Transcranial doppler ultrasound

TIA Transient ischemic attack

TOF Time-of-flight

VS-ASL Vessel-selective arterial spin labeling MRI

Abstract

Cerebrovascular occlusive disease (CVOD) is a major risk factor for ischemic stroke and is characterized by the presence of stenosis in the arteries supplying the brain. The cerebral vasculature has an innate ability to compensate for flow reductions, caused by the presence of CVOD, through a network of collateral pathways in the circle of Willis (CoW). However, flow compensation is highly patient-specific and dependents on anatomy, patency of collateral pathways, degree of stenosis, and the condition of the cerebral microcirculation and its autoregulatory response. Unfortunately, clinically available imaging tools only provide limited information on flow compensation and the underlying cerebral hemodynamics. Given the complexity of the cerebral vasculature, better tools are necessary to characterize cerebral hemodynamics and guide the risk assessment of CVOD.

Image-based computational fluid dynamics (CFD) provides a powerful tool for non-invasively analyzing cerebral hemodynamics with high spatial and temporal resolutions. However, CFD modeling of cerebral hemodynamics is challenging due to the need for patient-specific data to calibrate outflow boundary conditions in the brain. In this thesis, we explore a novel strategy to quantitatively characterize cerebral hemodynamics using CFD in combination with tissue perfusion from arterial spin labeling (ASL) MRI.

Firstly, we quantified territorial perfusion in the cerebral circulation by implementing and optimizing a vessel-selective arterial spin labeling (VS-ASL) sequence. VS-ASL is generally limited by its low labeling efficiency causing poor signal-to-noise ratio. We investigated the effects of off-resonance, pulsatility, and vessel movement, and evaluated methods to maximize labeling efficiency and overall image quality. We found that an off-resonance calibration scan in combination with cardiac-triggering significantly improved labeling efficiency and image quality. Vessel movement during the MRI protocol occurred in most study subjects and needs to be accounted for to maximize labeling efficiency.

Secondly, we developed a strategy to calibrate patient-specific CFD models of cerebral blood flow. The calibration consisted of estimating the total inflow to the CoW from PC-MRI and the flow

splits in the CoW from non-selective ASL perfusion images. The outflow boundary conditions were iteratively tuned to match the estimated flow splits, and the ASL-calibrated CFD model was then validated against territorial perfusion maps from VS-ASL by calculating the blood supply to each cerebral territory using Lagrangian particle tracking (LPT). We found an overall good match across study subjects; particularly, the flow compensation between hemispheres was captured well by the calibrated CFD models.

Thirdly, we investigated the impact of two outflow boundary condition strategies, an ASL-based and allometric-based calibration, on cerebral hemodynamics. The ASL-based calibrated CFD analysis captured the flow compensation between hemispheres as measured with VS-ASL and lead to an approximately symmetrical flow distribution in the CoW. In contrast, the allometric-based calibrated CFD analysis was unable to capture the collateral flow compensation, which resulted in large differences in flow between hemispheres.

Finally, the clinical feasibility and capabilities of our proposed CFD analysis was demonstrated in two CVOD patients. The CFD analysis showed significant differences in cerebral hemodynamics between the patients despite similar degrees of stenosis severity, highlighting the importance of a patient-specific assessment. Comparison of pre-operative and post-operative hemodynamics in one patient resulted in only minor changes following revascularization despite severe carotid stenosis. We demonstrated that our CFD analysis can provide detailed and quantitative information about hemodynamic impact of carotid stenosis and collateral flow compensation in the CoW.

Chapter 1: Introduction

1.1 Motivation

The clinical assessment of patients with cerebrovascular occlusive disease (CVOD) generally relies on measurements of degree stenosis to determine the risk of future ischemic stroke. However, it is important to point out that the pathophysiology of CVOD is highly complex and includes other key contributing factors beyond the degree of stenosis. Cerebral hemodynamics play a particular important role in the risk assessment of stenosis due to the vasculature's ability to compensate flow distally in the circle of Willis. Cerebral flow compensation however is highly patient-specific due to the large variability in cerebrovascular anatomy, disease progression, patency of collateral pathways, and cerebral vascular flow reserve. To further investigate the role of flow compensation in CVOD, a patient-tailored analysis of cerebral hemodynamics is needed.

Currently available clinical imaging tools provide only a snapshot of cerebral hemodynamics, mostly limited to information on velocity. However, to obtain a detailed description of cerebral hemodynamics, quantitative data on the velocity and pressure in the large arteries, as well as the blood supply in the main vascular territories of the brain is needed.

The goal of this thesis was to develop a novel modeling and imaging strategy, which combines the complementary strengths of computational fluid dynamics (CFD) and arterial spin labeling MRI (ASL) to characterize cerebral hemodynamics. While CFD provides a description of velocity and pressure in the large cerebral arteries with high spatial and temporal resolution, ASL provides information on the function of the distal vasculature by measuring tissue perfusion. We hypothesize that our proposed strategy can provide a detailed insight in the complex cerebral hemodynamics of patients with cerebrovascular disease and guide clinical assessment in the future.

1.2 Cerebral vasculature

The brain requires a constant supply of oxygen, representing approximately one fifth of the body's entire oxygen consumption. The main arteries in the neck responsible for the blood supply to the brain are the right and left internal carotid arteries (ICA) (~80% of total cerebral blood flow) in the anterior of the neck and the right and left vertebral arteries (VA) (~20% of total cerebral blood flow) in the posterior of the neck. These arteries originate from the aortic arch and reach all the way up into the cranium. At the base of the brain, the internal carotid and vertebral arteries form an anastomotic circular structure called the circle of Willis (CoW) (Fig. 1.1). Branching off the CoW, six main cerebral arteries supply all parts of the brain, namely the anterior, middle, and posterior cerebral arteries (ACA, MCA, and PCA). The circular structure is completed in the front of the brain by the anterior communicating artery, connecting the right and left hemispheres and in the back of the brain through the right and left posterior communicating arteries, connecting the ICAs with the posterior circulation. This system of communicating arteries functions as a network of collateral pathways to maintain adequate blood supply to the brain in cases of flow reductions in one of the main neck arteries. However, there is high variability in the anatomy of the CoW among the population, with only approximately 50% having a complete circular structure[1]. Anatomical variations can have significant effects on the vasculature's capacity to compensate for changes in blood supply to the brain. Augmenting the collateral flow compensation, the cerebral vasculature has the innate ability to maintain adequate blood supply to the tissue over a wide range of cerebral perfusion pressures through cerebral autoregulation. Cerebral autoregulation controls blood flow by dilating or constricting the arteriolar diameter, which changes the resistance of the distal vascular.

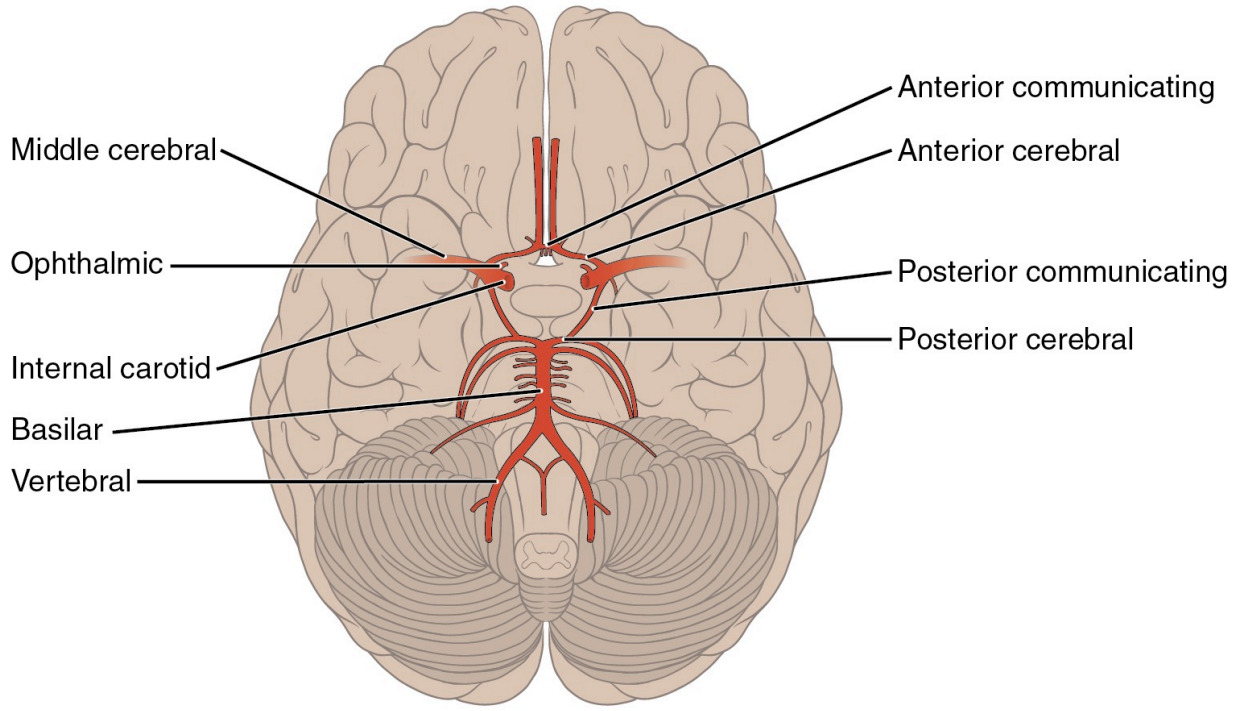

Fig. 1.1 Anatomy of the main cerebral arteries of the circle of Willis at the base of the brain[1].

1.3 Cerebrovascular occlusive disease

Strokes are the third most common cause of death in the US, with cerebrovascular occlusive disease (CVOD) being implicated in the pathology of 20-25% of all strokes [2]. CVOD is characterized by the buildup of plaque inside the main brain-supplying arteries in the neck, typically located at the carotid bifurcation. The buildup of plaque, also referred to as atherosclerosis, is caused by the gradual deposit of fatty material and cholesterol on the inner lining of the artery wall. With the progression of the disease, the affected arteries may become stiffer and the vessel lumen reduces, thereby restricting blood flow to the brain (Fig. 1.2). A significant reduction in luminal cross-sectional area, or stenosis, increases the risk of stroke through several mechanisms. First, the stenosed vessel itself can result in a critical reduction in blood flow to the ipsilaterally supplied tissue, especially in the absence of collateral blood supply, and result in brain ischemia. Second, the rough surface of the plaque can cause the formation of thrombus, which can block the remaining lumen or break off and block a small downstream vessel. Third, instable

[1] Image: https://cnx.org/contents/GqYHW4Z4@3/Circulatory-Pathways

plaque can rapture and travel downstream to lodge in one of the smaller arteries, thereby blocking flow to the brain tissue (emboli).

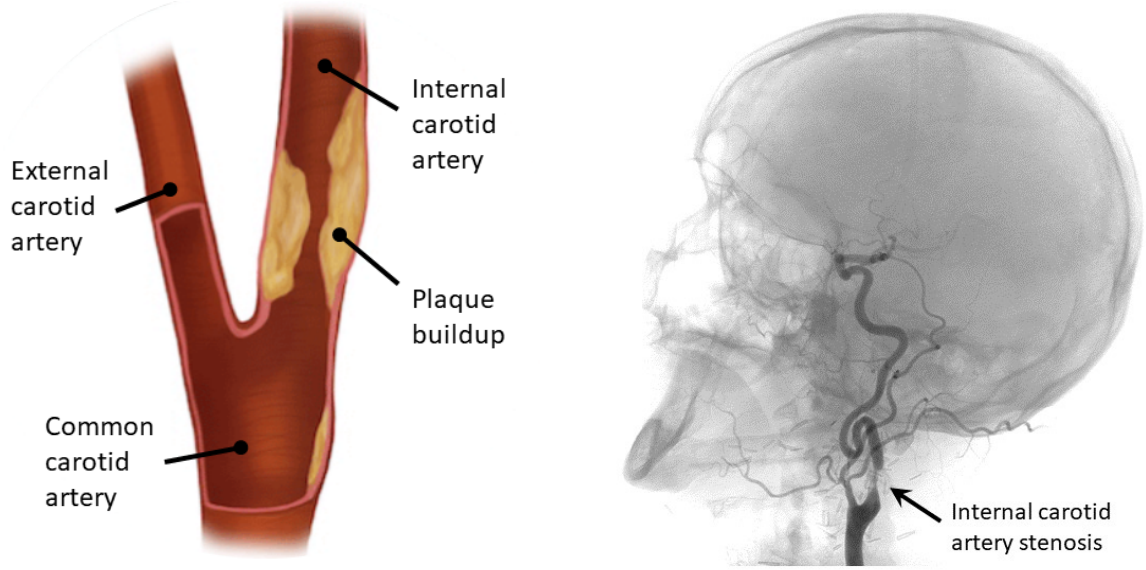

Fig. 1.2 **Left:** Schematic of a typical internal carotid artery stenosis above the carotid bifurcation[2]. **Right:** Cerebral angiogram of a carotid artery with stenosis[3].

The diagnosis of CVOD is based on imaging the stenosed vascular segment with either doppler ultrasound or CTA/MRA and calculating the degree of diameter reduction in the stenosis. The degree of diameter reduction is calculated based on either the NASCET criteria (North American Symptomatic Carotid Endarterectomy Trial) or ECST criteria (European Carotid Surgery Trial) (Fig. 1.3). The stenosis based on NASCET is defined as $stenosis_{NASCET} = (A - B)/A$, where A is the patent vessel diameter distally to the stenosis and B is the minimum vessel diameter in peak stenosis. The stenosis based on ECST is defined as $stenosis_{ECST} = (C - B)/C$, where C is the diameter of the original (unstenosed) vessel in peak stenosis. Alternatively, the degree of stenosis can be derived from velocity measurements in peak stenosis using doppler ultrasound, where a peak systolic velocity of 125 - 230 cm/s or an end diastolic velocity of 40-100 cm/s corresponds to a diameter reduction of 50-69% (NASCET).

[2] Image: https://iveivascular.com/en/ictus-prevention-treatment-of-carotid-stenosis
[3] Image: Courtesy of Dr. Criado, University of Michigan

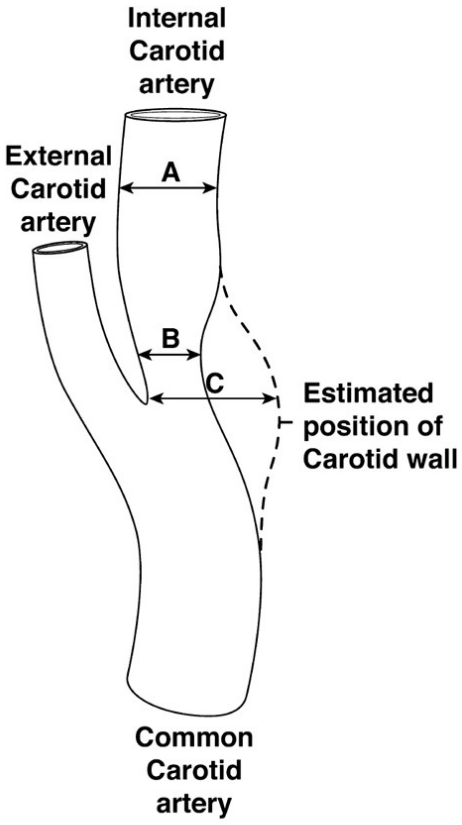

Fig. 1.3 Schematic describing the location of the diameter measurements used to calculate the degree stenosis based on the NASCET and ECST[4].

Treatment options for patients with CVOD range from medical therapy to revascularization, depending on the severity of the stenosis and the presence/absence of symptoms. Symptomatic patients with a history of transient ischemic attacks (TIAs) or ipsilateral stroke, who have a stenosis of > 50% (NASCET) are recommended for revascularization [3][4][5]. In asymptomatic patients, the stenosis threshold for revascularization is increased to > 60% (NASCET) [6][7]. Patients without symptoms in combination with low-grade stenosis of less than 50% are treated with medical therapy, which includes antiplatelet medication (e.g. aspirin), cholesterol-lowering statins, and antihypertensive medication (e.g. beta blockers). For patients who are recommended for revascularization, two options are available: Carotid endarterectomy (CEA) and carotid angioplasty with stenting (CAS) (Fig. 1.4). CEA is an open surgery to remove the plaque. After clamping the carotid artery proximal and distal to the stenosis, an incision is made, and the plaque is peeled out. The artery is then closed with sutures and in some cases the closing is performed in

[4] Image: https://link.springer.com/chapter/10.1007/978-1-60327-125-7_18

combination with patch angioplasty. In contrast, CAS is a minimally invasive endovascular procedure, in which a catheter is inserted through the femoral artery. At the location of the stenosis, a balloon is inflated to open the artery and compress the plaque towards the vessel wall. To keep the artery open, a stent is placed over the compressed plaque. The efficacy of CEA versus CAS was evaluated in the CREST study (Carotid Revascularization Endarterectomy vs. Stenting Trial) and resulted in no significant difference in the estimated 4-year rates of the primary end points (CAS = 7.2% and CEA = 6.8%, P=0.51) for both symptomatic and asymptomatic patients [8]. However, CAS is the preferred method in patients who are at high surgical risk.

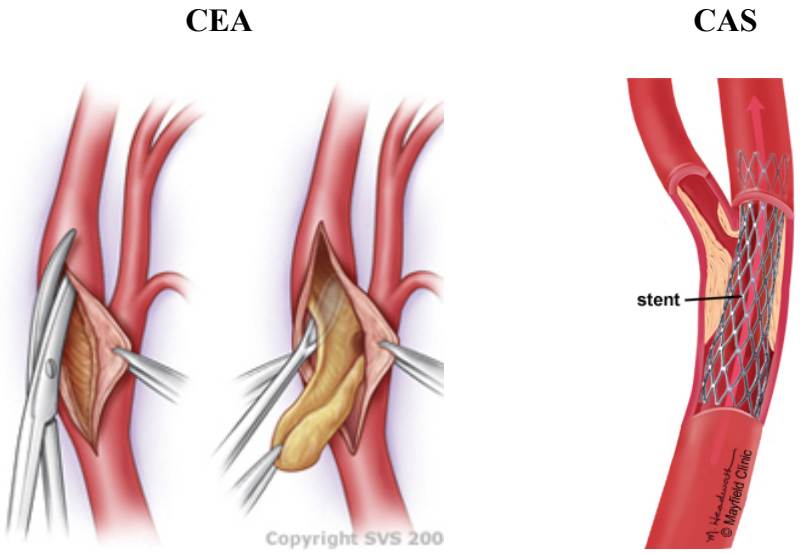

Fig. 1.4 Schematic illustration of carotid endarterectomy (CEA)[5] and carotid angioplasty with stenting (CAS)[6]

However, these guidelines for revascularization are based on randomized controlled trials dating back 20 years. Especially in asymptomatic patients, the benefits of revascularization are highly debated among physicians. Significant advancements have been made since in the fields of medical therapy and carotid revascularization, prompting a re-evaluation of the guidelines. Ongoing trials to investigate the benefits of revascularization versus medical therapy again include CREST-2 (Carotid Revascularization and Medical Management for Asymptomatic Carotid Stenosis Trial-2) and ACST-2 (Asymptomatic Carotid Surgery Trial-2).

[5] Image: https://www.circulationfoundation.org.uk/help-advice/carotid/carotid-endarterectomy
[6] Image: https://mayfieldclinic.com/pe-carotidstenosis.htm

1.4 Medical imaging of cerebral blood flow

A number of imaging tools for acquiring data on cerebral hemodynamics are available in the clinical setting. The most commonly used tools include transcranial doppler ultrasound (TCD) and phase contrast /4D flow MRI for measuring velocity, and digital subtraction angiography (DSA) for imaging the intracranial blood supply. Information on blood pressure in the intracranial arteries is generally not clinically available. Following, the advantages and limitations of these most imaging tools are discussed in more detail.

1.4.1 Intracranial doppler ultrasound

TCD is a non-invasive method of measuring blood flow velocities in the main cerebral arteries. Using the principle of the Doppler effect, ultrasound waves are transmitted through the skull and reflected back by the moving blood cells inside the vessels. The frequency difference of the transmitted and reflected waves is proportional to the velocity of the blood cells. The specific parameters obtained from TCD in the large cerebral arteries include the peak systolic and end-diastolic velocities and pulsatility index. Clinical applications of TCD include the diagnosis of intracranial stenosis [9], detection of microembolic events [10], and prognostication of acute ischemic stroke [11]. Furthermore, TCD in combination with acetazolamide-induced arteriolar dilatation has been used to measure the cerebral vascular flow reserve in patients with carotid stenosis [12]. While TCD provides velocity measurements with high temporal resolution, measurements are limited to a velocity spectrum at selected locations along the vessel. Furthermore, peak velocity measurements are highly sensitive to the angle between the ultrasound probe and the vessel and can lead to significant errors (operator-dependency).

1.4.2 Phase-contrast/4D flow MRI

In phase-contrast (PC) MRI, velocity-encoded images are acquired by taking advantage of the relationship between blood flow velocity and the phase of blood spins in the presence of a magnetic gradient. Spins moving along the direction of a pair of bipolar gradients accumulate phase proportional to their velocity. In standard 2D PC-MRI, spins are encoded orthogonal to the image slice and time-resolved data is collected over multiple cardiac cycles using ECG-gating. More recently, PC-MRI has been extended to include velocity encoding in all three spatial dimensions in a volume of slices throughout the cardiac cycle, thus resulting in a time-resolved 3D velocity field or 4D flow data. Clinical applications of 4D flow in the cerebral vasculature include the

evaluation of intracranial aneurysm [13][14], cerebral arteriovenous malformation [15], and intracranial stenosis [16]. Beyond velocity, 4D flow data has also been utilized to derived a relative pressure gradients in the cerebral arteries [17]. The main drawbacks of 4D flow for intracranial applications are the long acquisition times necessary to cover the entire brain (5-20 min) and the limited spatial resolution (~ 1 mm^3) causing partial volume effects when imaging the small cerebral arteries (2-3 mm in diameter).

1.4.3 Digital subtraction angiography (DSA)

DSA is a fluoroscopic technique used to visualize the anatomy of blood vessels. DSA is performed by injecting a contrast agent via catheter into a target artery while acquiring x-ray images of the distal vasculature. For intracranial applications, the catheter is typically placed in either the carotid or vertebral arteries to visualize the blood supply in the brain. DSA is considered the gold standard for detecting intracranial aneurysm [18], arteriovenous malformations [19], and collateral flow patterns in the presence of stenosis [20]. While providing images with high spatial resolution, DSA is an invasive procedure which has been associated with an increase in neurologic complications. Furthermore, image analysis is typically limited to a qualitative assessment.

1.5 Arterial spin labeling MRI

Complementary to measuring cerebral hemodynamics at the level of the large cerebral arteries, perfusion measurements at the level of the brain tissue provide valuable information about the distal vasculature and the overall blood supply to the brain. Perfusion is defined as the process of blood flow to a capillary bed in an organ tissue and subsequent exchange of oxygen across a semipermeable wall. Perfusion is measured as volume of blood per unit of time and tissue mass. In the brain, perfusion measurements provide important information about the functional and metabolic status of the tissue. Traditional imaging techniques for clinical measurements of brain perfusion include perfusion CT, single-photon emission computed tomography (SPECT), and positron emission tomography (PET). However, all these methods are invasive and require the injection of an exogenous tracer. Over the last decade, arterial spin labeling (ASL) has gained popularity as a non-invasive MRI alternative. Relevant clinical applications of ASL include neurovascular (e.g. stroke) [21][22][23] and neurodegenerative (e.g. Alzheimer's, Parkinson's) disorders [24][25][26]. In ASL, the arterial blood itself is used as an endogenous tracer by inverting the magnetization of blood spins in the region of the neck. After a short transit delay to give the

bolus sufficient time to travel to the brain tissue, a volume of images is acquired in the brain. The acquired "label" images contain signal from both the labeled blood water and the static water in the brain. To extract the labeled blood water signal from the images, a set of "control" images is acquired without prior labeling of the blood. Subtraction of the label from the control images removes the signal from the static water and yields perfusion-weighted images (Fig. 1.5). The signal of the labeled blood represents only about 1% of the total signal contained in the control images. As a result, ASL images are generally low in signal-to-noise ratio (SNR). To ensure adequate SNR, ASL is typically acquired with multiple averages and low resolution.

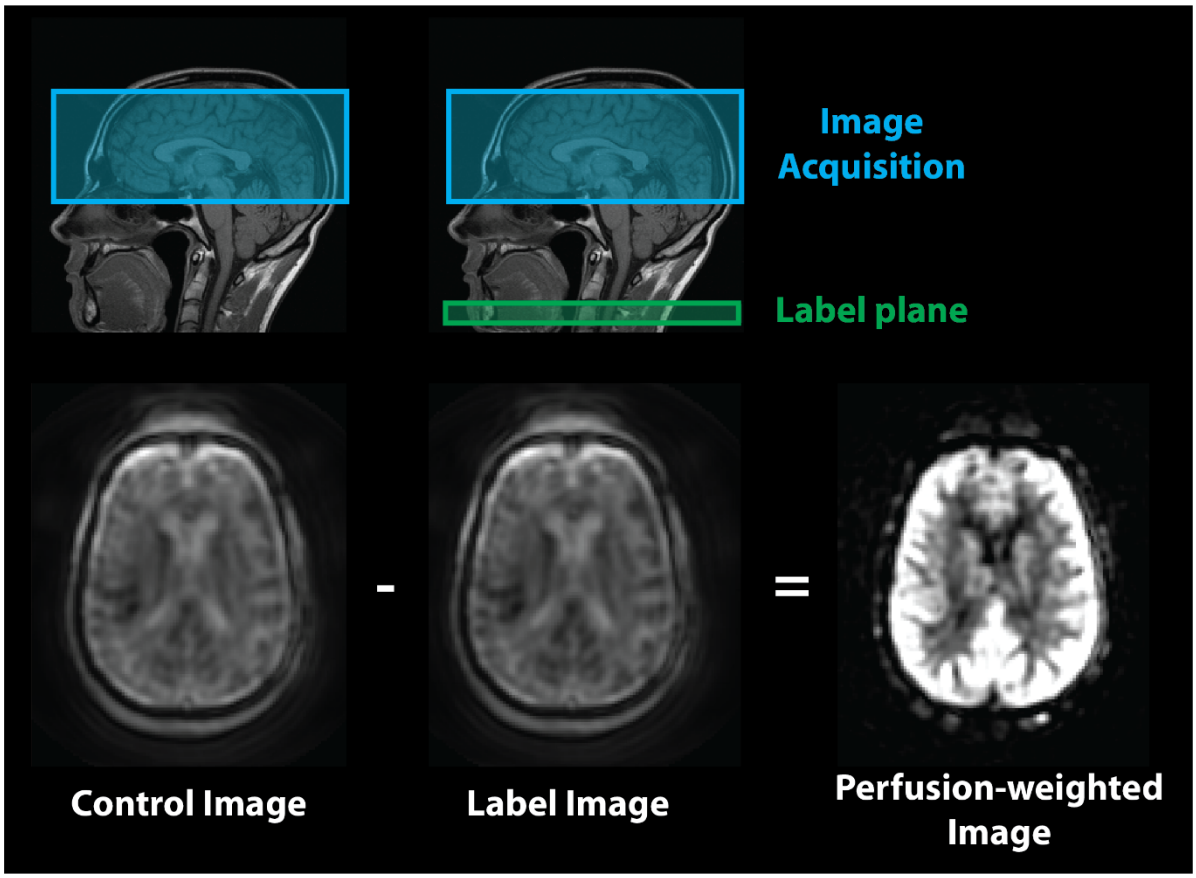

Fig. 1.5 Acquisition of ASL images. Perfusion-weighted images are generated by subtracting control (stationary spins) and label (stationary spins + labeled blood) images.

1.5.1 Non-selective PCASL

There are two methods available for labeling the blood spins in the neck: pulsed ASL (PASL) and pseudo-continuous ASL (PCASL). In PASL, a thick slab of blood spins is inverted simultaneously using a short radiofrequency pulse (RF) [27]. However, the maximum bolus size in PASL is limited by the available slab thickness, which significantly affects SNR. In contrast, PCASL

overcomes this limitation by labeling blood spins continuously as they travel across a thin labeling plane in the neck [28]. As a result, PCASL is the preferred labeling scheme for clinical applications and will be the focus of this project. Please note that whenever the acronym ASL was used in this thesis to describe perfusion imaging, it refers to a PCASL labeling scheme.

In PCASL, spins are labeled using the principle of flow-driven adiabatic inversion. During the labeling period, a train of RF pulses is played in combination with a train of slice-selective gradient pulses pointing in the direction of blood flow (Fig. 1.6a). The mean gradient amplitude between RF pulses is non-zero, resulting in the accumulation of phase as the spins travel through the label plane. In order to achieve inversion, spins need to maintain a spin-lock with the effective magnetic vector of the RF pulse and the gradient vector. To achieve a spin-lock at the label plane location, the phase of the *n*th RF pulse needs to match the accumulated phase of the spins

$$\phi_n = \sum_n \gamma \, \bar{G}_z \Delta t \, z \qquad \textbf{(1.1)}$$

with the gyromagnetic ratio γ, the mean gradient in z-direction $\bar{G}_z$, the spacing between RF pulses Δt, and the distance between the isocenter of the magnet and the label plane z. The same label train is applied in the control acquisition, but the phase of the RF is shifted π every other pulse to avoid a spin-lock but maintain the same magnetic transfer in the imaging volume. In this PCASL label train, all spins traveling through the label plane regardless of their position within the label plane, are inverted. The resulting perfusion images are a "non-selective" and represent the total perfusion in each voxel in the brain from both vertebral and internal carotid arteries (Fig. 1.6b).

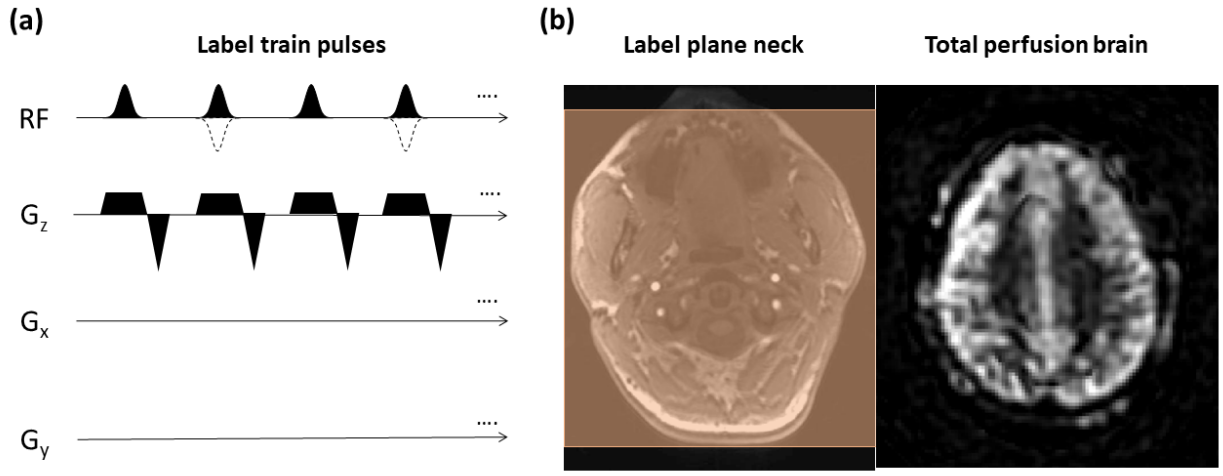

Fig. 1.6 Non-selective PCASL sequence. **(a)** RF and gradient waveforms of the non-selective label train. The control RF pulses are represented by the dotted line. **(b)** Generated label plane in the neck and the resulting total perfusion in a slice of the brain.

1.5.2 Vessel-selective PCASL

The PCASL label train can be further modified to acquire territorial perfusion maps by including vessel-selective labeling properties to the label train. Territorial perfusion maps provide information about the blood supply from individual arteries in the neck to the main brain territories. Previous clinical applications include the measurement of collateral flow patterns in cerebrovascular occlusive disease [29] and the identification of emboli sources in stroke [30]. Vessel-selective labeling is achieved by including additional in-plane gradient blips in the x- and y-direction. To invert the spins at a target location within the label plane, the phase of the *n*th RF pulse needs to account for the additional accumulated phase of the spins as following:

$$\phi_n = \gamma \sum_n \left(\bar{G}_z \Delta t \; z + \; \bar{G}_{x,n} \Delta t \; x + \; \bar{G}_{y,n} \Delta t \; y \right) \qquad \textbf{(1.2)}$$

where $\bar{G}_{x,n}$ and $\bar{G}_{y,n}$ are the mean gradients in x- and y- direction for the *n*th RF pulse and *x* and *y* are the target location within the label plane. In vessel-encoded PCASL [31], the amplitude of the additional gradient blips is kept constant throughout the label train to create a "stripe" pattern across the label plane. Pairs of arteries are placed in label and control condition by creating a π-phase shift between the arteries. Multiple combinations of artery pairs are acquired based on a Hadamard encoding scheme to extract the perfusion contributions of each individual artery. More

recently, super-selective PCASL (SS-PCASL) was introduced to directly label an individual artery and to avoid complex post-processing [32][33]. In SS-PCASL, the additional gradient blips are rotated each RF pulse, thereby creating a circular label spot, which can be moved to any artery within the label plane (Fig. 1.7). By labeling all main neck arteries individually, combined territorial perfusion maps can be created showing the contributions of each neck artery to the total perfusion in the brain on a voxel-by-voxel basis. Furthermore, labeling in SS-PCASL is not restricted to the neck and can be performed intracranially.

This thesis focuses on the SS-PCASL scheme for territorial perfusion imaging. The terms vessel-selective (VS)-ASL and SS-PCASL are being used interchangeably in the remainder of the manuscript.

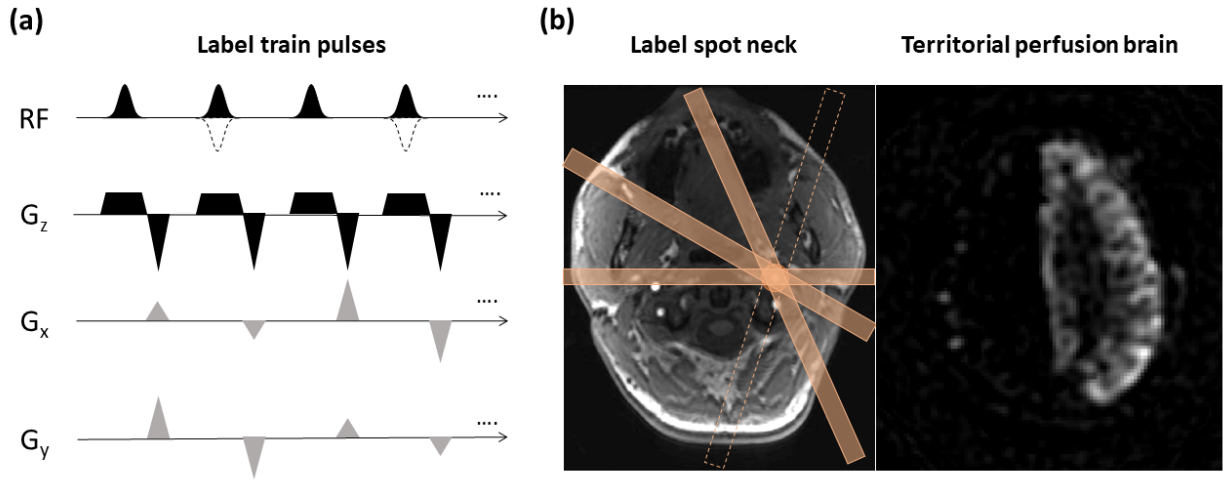

Fig. 1.7 SS-PCASL sequence. **(a)** RF and gradient waveforms of the super-selective label train. The control RF pulses are represented by the dotted line. **(b)** Rotation of the in-plane gradient blips creates rotating stripe pattern which effectively only labels spins at the intersection of all stripes and hence creates a circular label spot. The resulting images show the perfusion territory of the labeled artery.

1.6 Computational modeling of cerebral blood flow

Computational modeling has become an increasingly popular method of quantifying cardiovascular hemodynamics and augment or in some cases even replace medical imaging. The physics of blood flow in the cardiovascular system are governed by the pulsatile incompressible Navier-stokes equations, which can be written as:

$$\rho\left(\frac{\partial \boldsymbol{v}}{\partial t} + \boldsymbol{v} \cdot \nabla \boldsymbol{v}\right) = -\nabla p + \mu \nabla^2 \boldsymbol{v} + \boldsymbol{f}$$
$$\nabla \cdot \boldsymbol{v} = 0 \qquad \textbf{(1.3)}$$

Where $\boldsymbol{v}$ is the velocity vector, p the pressure, ρ the density, μ the dynamic viscosity, and $\boldsymbol{f}$ is the body force. The first equation describes the conservation of momentum and the second equation the conservation of mass.

Different formulations of the Navier-stokes equations, ranging in complexity from 0D to 3D, have been used for computational fluid dynamics (CFD) modeling cerebral blood flow. In the following, a brief overview over these different modeling strategies and their applications in the cerebral vasculature is presented.

1.6.1 0D models

0D models or "lumped parameter" models are derived from the analogy between electrical circuits and blood flow. Electrical elements including the resistance *R*, the capacitance *C*, and the inductance *L* can be used to describe the effects of vessel resistance, vessel compliance, and the inertia of blood flow. These elements can be then used to model different segments of the arterial tree, the compartments of the heart, the venous system, and the pulmonary system. 0D network models have for example been used to study the effects of intracranial stenosis [34] and the compensatory capabilities of the CoW [35]. 0D models have also been used in combination with control mechanism to study the dynamic response of the cerebral vasculature in response to a posture change [36].

1.6.2 1D models

In contrast to 0D models, 1D models can capture the pulse wave propagation and hemodynamic changes along the arteries. 1D models use a simplified version of the Navier-stokes equations by solving for cross-sectionally averaged velocity and pressure along the axial direction of the artery. To make the system of equations solvable, an explicit algebraic relationship between pressure and cross-sectional area needs to be defined [37]. Examples of 1D application in the cerebral vasculature include the study of collateral recruitment patterns in the CoW [38], anatomical variations on flow compensation [39], and cerebral vasospasm [40].

1.6.3 3D models

While 0D/1D formulations of the Navier-Stokes equations allow to simulate the overall flow distribution in the vascular system, a 3D formulation is needed to resolve local flow phenomena. 3D formulations are especially important when modeling the hemodynamics of stenosis or aneurysm. A solution for velocity and pressure can be approximated by using the finite element method (FEM). However, solving the full 3D formulations of the Navier-stokes equations requires substantially higher computing effort compared to 0D or 1D formulations and are typically performed on high performance computing systems. 3D applications in the cerebral vasculature include studies of intracranial stenoses [41][42] and aneurysms [43][44][45].

In this work, we will be using the 3D formulation of the Navier-Stokes equations to model the hemodynamics in the neck and brain arteries. Despite the increase in computation time, the 3D formulations are necessary to model the complex hemodynamics around stenosis and to model the blood supply of individual arteries in the neck to the brain.

1.6.4 CFD boundary conditions

An essential part of CFD modeling is the specification of boundary conditions on the 3D computational domain. In this work, the boundaries comprise the inflow face at the ascending aorta, the outflow faces of the descending aorta, subclavian arteries, external carotid arteries, and the intracranial arteries, and the vessel walls connecting the inflow and outflow faces. In our CFD analysis, we employed a Dirichlet boundary condition at the inflow of the ascending aorta by prescribing a pulsatile velocity profile, derived from PC-MRI flow data. Each domain outflow was coupled to a 3-element Windkessel model to capture the overall hemodynamic behavior of the distal vascular bed (Fig. 1.8). The 3-element Windkessel model is a lumped-parameter model comprised of a proximal resistance R_p, distal resistance R_d, and compliance C. At the vessel walls, a “no-slip” Dirichlet boundary condition was prescribed by setting the velocity on the boundary to zero. One of the main challenges of patient-specific CFD modeling is to specify the parameters of the boundary conditions, in particular the 3-element Windkessel model parameters, in a systematic and physiologically meaningful way to accurately represent the patient’s true hemodynamics.

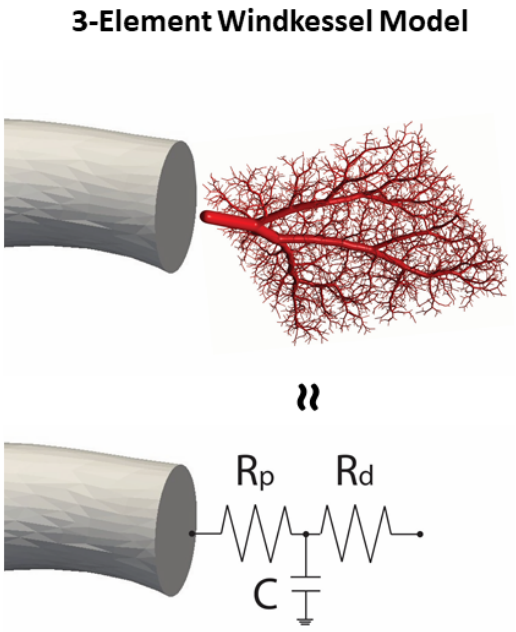

Fig. 1.8 3-element Windkessel model consisting of a proximal resistance R_p, distal resistance R_d, and a capacitor C.

1.7 Structure of thesis

We first implemented a vessel-selective PCASL MRI sequence to acquire territorial perfusion images. To maximize labeling efficiency and to optimize image quality, we investigated the effects of off-resonance, pulsatility, and vessel movement in a group of healthy subjects (**Chapter 2**). We then developed a novel strategy to calibrate patient-specific computational models of cerebral blood flow using perfusion data from non-selective PCASL and flow information from PC-MRI. The calibrated CFD models were validated against territorial perfusion data from vessel-selective PCASL (**Chapter 3**). Following, the clinical feasibility of our calibrated CFD analysis to assess the impact of carotid stenosis on cerebral hemodynamics, including collateral flow compensation, was demonstrated in pre-operative patients with carotid stenosis (**Chapter 4**). Additionally, the changes in cerebral hemodynamics following carotid revascularization were analyzed in one patient. Next, we compared the performance of our proposed patient-specific CFD calibration strategy against an allometric-based calibration approach commonly used in the literature (**Chapter 5**). Finally, a general discussion and future work are presented (**Chapter 6**).

Chapter 2: Territorial Perfusion Mapping in the Cerebral Circulation Using Super-Selective Pseudo-Continuous Arterial Spin Labeling

2.1 Introduction

Perfusion measurements of vascular territories in the brain offer critical clinical information on cerebrovascular function. In the presence of steno-occlusive cerebrovascular disease, vascular territory maps can be used to identify and evaluate collateral flow pathways [46][47]. In cryptogenic stroke, blood supply knowledge of individual arteries to different parts of the brain can help identify the origin of the stroke and guide treatment [48]. The current clinical gold standard for measuring brain vascular territories is digital subtraction angiography, an invasive, non-quantitative procedure relying on the injection of a contrast agent which increases the risk of neurologic complications [49].

In the last decade, the use of MRI Arterial Spin Labeling (ASL) has gained popularity as a noninvasive and quantitative alternative for measuring brain tissue perfusion. Pseudo-continuous labeling (PCASL) is the current preferred inversion scheme [50] in which blood spins flowing through a label plane are continuously inverted to generate a bolus of label which can be measured downstream in the tissue after a short transit time. More recently, the PCASL scheme was extended to include vessel-selective labeling to map perfusion territories. Vessel-selective labeling generally uses additional in-plane gradient blips (perpendicular to the slice-selective gradient) in-between RF pulses and the tracking of the accumulated phase at the target location for the next RF pulse. In vessel-encoded PCASL (VE-PCASL) [31], combinations of vessel pairs are placed in label and control condition by in-plane gradients with a constant amplitude to generate a π-phase-shift between vessel pairs. Contributions from individual vessels are estimated by acquiring multiple combinations based on a Hadamard encoding strategy. To facilitate labeling of individual vessels and to avoid lengthy post-processing procedures, Helle et al. [32] and Dai et al. [33], developed super-selective PCASL (SS-PCASL). By applying gradient blips with time-varying amplitudes, the SS-PCASL scheme generates a circular label spot with adaptable center location and size.

While the ability to label intracranial arteries is one of the major advantages of SS-PCASL, the focus of this work is on labeling in the neck vessels. There is considerable clinical interest in mapping the perfusion territories of the main brain-feeding arteries due to the high anatomical variability of the circle of Willis [51][52]. However, many of the issues and solutions investigated are also applicable to intracranial territorial mapping as well as to VE-PCASL.

While the feasibility of SS-PCASL has previously been shown in a number of clinical applications [46][53][54][55], SNR still remains a challenge [56]. PCASL is well known to be a low SNR technique. In SS-PCASL, SNR is further reduced because of inherently lower labeling efficiency [32], particularly noticeable in low-flow vessels such as the vertebral arteries. A reduction in labeling efficiency can result in the erroneous conclusion that an artery is not contributing to the perfusion of a region in the brain. Labeling efficiency can vary significantly within a scan session, between vessels, and across subjects. Consequently, there is a need to maximize labeling efficiency and to assess efficiency differences between vessels in order to produce accurate, quantitative territorial perfusion maps. These challenges, together with the overall availability of the sequence, must be addressed for SS-PCASL to become mainstream. In the following, the primary causes of reduction in labeling efficiency and SNR, as well as our strategies to mitigate them, are outlined.

Field inhomogeneity (off-resonance): In the presence of off-resonance, the mismatch between the applied RF phase increment and the phase gain experienced by the spins results in a weakened spin lock, therefore reducing the efficiency of the flow-driven adiabatic inversion. Although rarely used in current publications, a number of off-resonance compensation strategies for non-selective PCASL have been proposed [57][58][59]. Here, we evaluate two compensation strategies for SS-PCASL, a multi-phase pre-scan and a field map acquisition, to estimate the optimal off-resonance phase compensation. While the field map measures field inhomogeneity directly, the multi-phase pre-scan estimates the off-resonance indirectly from a set of perfusion images acquired over a range of RF-phase correction increments.

Pulsatility: In PCASL, label and control images are acquired sequentially in a fixed interval (TR) and therefore at different time points in the cardiac cycle. Variations in blood flow during the label period can affect labeling efficiency. Furthermore, differences in the blood volume in the cerebral arteries at the time of the acquisition can lead to significant artifacts when subtracting the label

from the control images. Here, we explore the use of cardiac-triggered SS-PCASL to reduce the effects of pulsatility based on the scheme for standard PCASL by Li et al. [60].

Label rotation scheme: The circular label spot in SS-PCASL is created by applying time-varying in-plane gradient blips, which create a set of rotating inversion bands. The rotation scheme is determined by the time course of the in-plane gradients. Previously proposed label rotation schemes have shown a significant influence on labeling efficiency [32]. Based on Bloch-simulations, we compare the labeling efficiency of multiple label rotation schemes in the absence and presence of off-resonance.

Label spot size and position: The success of SS-PCAL depends on accurate positioning of the label spot onto the vessel of interest. Any mismatch can result in a significant reduction in labeling efficiency. The effects of vessel movement are explored via Bloch-simulations and compared to in vivo vessel movement measurements.

This work is intended as a practical guideline for acquiring high quality territorial perfusion fraction maps with SS-PCASL. Towards that goal, we first investigate the effects of off-resonance, pulsatility, vessel movement, and rotation scheme on SS-PCASL labeling efficiency and overall image quality. We evaluate strategies to mitigate different sources of error based on practicality and effectiveness. Finally, we present a strategy to estimate the territorial perfusion fraction for individual neck arteries based on direct measurements of labeling efficiency.

2.2 Methods

2.2.1 Bloch simulations

Simulations were performed in MATLAB to investigate the effects of off-resonance, label rotation scheme, and vessel location on labeling efficiency. We simulated the inversion of the longitudinal magnetization of spins flowing through the label plane subject to SS-PCASL RF and gradient pulses. The flow of spins was modeled in a 4 cm slab centered around the label plane. Based on the spatial mean velocity in the internal carotid artery (ICA) and vertebral artery (VA) (PC-MRI data from study 2, see section 2.2), a parabolic velocity profile was generated for each of the 20 acquired temporal phases. The parabolic velocity profiles were discretized with a grid containing 30 points in the radial direction. For each point of the profile, Bloch simulations were repeated for all cardiac phases. Based on the balanced version of PCASL, ’label’ and ’control’ pulse trains were

simulated with the same gradient waveform but with a 180° RF phase shift between RF pulses in the control condition. Labeling efficiency of each spin was calculated as

$$\alpha = \frac{M_{Z,\text{Control}} - M_{Z,\text{Label}}}{2\, M_{Z,\text{Control}}} \quad \textbf{(2.1)}$$

where $M_{Z,Control}$ and $M_{Z,Label}$ are the longitudinal spin magnetizations at the end of the simulated slab for the control and label conditions, respectively. The labeling efficiency was then averaged over the cardiac cycle and subsequently velocity-weighted over the vessel cross-section to yield a mean labeling efficiency. The parameters of the label train were set to match in vivo parameters (see section 2.2). The amplitudes of the in-plane gradients are determined by a design-specific rotation scheme. We focused on three schemes: constant clockwise, fully random, and pseudo-random rotation [32]. All schemes were based on 32 evenly distributed angular gradient positions and a constant effective in-plane gradient $G_{xy,k} = \sqrt[2]{G_{x,k}^2 + G_{y,k}^2} = 4\ mT/m$, which corresponds to a label spot size of 18 mm (FWHM). T_1 and T_2 were set to $1650\ ms$ and $250\ ms$, respectively.

Mean labeling efficiency was evaluated for different amounts of off-resonance, ranging from 0 to 400 Hz. The three label rotation schemes were simulated and compared to a non-selective label scheme. The effects of vessel movement were simulated by moving the center of the vessel-cross-section out of the label spot. Mean labeling efficiency was evaluated over a range of (0-10) mm vessel movement.

2.2.2 In vivo imaging

Two in vivo studies were performed on a total of 12 healthy subjects (9 males, 3 females, mean age 27.8). The study protocol was approved by the local Internal Review Board and written consent was obtained from each participant. All scans were performed at 3T (GE Healthcare MR750, Waukesha, WI) with a 32-channel receive-only head coil.

2.2.2.1 Study 1: Optimization of labeling efficiency

This study included 10 volunteers. The protocol started with a 2D time-of-flight (TOF) of the neck to determine the optimal position of the label plane and the location of the arteries. A position

slightly above the carotid bifurcation was selected, where both carotid and vertebral arteries run perpendicular to the label plane and the distance between vessels is maximal. The sequence parameters are: TR/TE = 12.7/2.4 ms, voxel size = 0.43 x 0.43 x 4 mm^3, 20 slices, acquisition time = 47 s. The image volume, not including the region of the label plane, was shimmed only once before the first PCASL sequence using the standard GE pre-scan procedure. The table position was kept fixed throughout the perfusion scans to avoid any change in the magnetic field.

Off-resonance calibration: Off-resonance was investigated by acquiring three sets of SS-PCASL images of the left ICA, each with a different off-resonance calibration. The calibration strategies consisted of a multi-phase pre-scan, a field map, and a scan without calibration. We performed the three calibration strategies in randomized order, each followed by a cardiac-triggered SS-PCASL scan (details below). In the multi-phase calibration, a non-selective PCASL perfusion pre-scan ($G_{xy} = 0\ mT/m$) was acquired with multiple phase corrections added to the RF pulse train. The RF phase correction was increased in steps of 0.4 rad, covering a range of [-3.2, 3.2 rad], between acquisitions of each label/control pair. The sequence consisted of a single-shot spiral acquisition (slices = 16, voxel size = 3.75 x 3.75 x 7 mm^3, TR/TE = 4000/4 ms, label duration = 1800 ms, post-labeling delay = 1400 ms, number of frames = 34 (17 phase increments), background suppression, acquisition time = 2 min 40 s). The slice prescription and the remaining sequence parameters were identical to the SS-PCASL scan (details below). The optimal off-resonance phase correction was estimated on the fly by subtracting pairs of control and label, masking a slice in the center of the image volume, averaging the signal intensity for each phase, and finding the maximum of a least-squares curve-fit with a sine-function. Next, a field map was collected in the same location as the PCASL label plane to measure the off-resonance directly. The acquisition consisted of a spoiled gradient echo, single slice, TR = 18 ms, voxel size = 0.85 x 0.85 x 4 mm^3, flip angle = 20°, and a ΔTE = 2.5 ms (which corresponds to an off-resonance frequency range of ±200 Hz). The phase correction was estimated by manually drawing a ROI around the vessel of interest and calculating the average off-resonance. The vessel itself was excluded from the ROI to avoid flow effects.

Cardiac triggering: Two sets of SS-PCASL images were collected with and without cardiac triggering, using the phase calibration of the multi-phase pre-scan. For this comparison, the dominant vertebral artery was labeled and the pulsatility artifacts, which are most dominant in the

middle cerebral artery, were observed outside the posterior perfusion territory. In the cardiac-triggered SS-PCASL perfusion scan, the balanced label/control pulse train was applied for 1800 ms (in-plane gradient amplitude $G_{xy} = 4\ mT/m$, slice-selective gradient amplitude $G_z = 6\ mT/m$, average slice-selective gradient $G_{z,ave} = 0.6\ mT/m$, 1ms time gap between RF pulses). After a post-labeling delay of 1800 ms, 16 slices were collected with a 2-shot spiral acquisition scheme (voxel size = 3.75 x 3.75 x 7 mm^3). Six subtraction image pairs were collected. The background suppression scheme included a saturation pulse right before the start of the RF label train and 2 adiabatic inversion pulses during the transit delay, followed by a fat suppression pulse. A cardiac-triggered scheme base on Li et al. [60] was used to trigger the start of the saturation pulse, as measured by a peripheral pulse oximeter, attached to the subject's index finger. After a minimum TR of 4400 ms, the sequence waited for a trigger to start the next label period. A proton density image was collected at the beginning of each perfusion scan. The total acquisition time for the perfusion scan was 2 min :45 s ± 10 s. In the non-triggered scan, the TR was fixed at 4400 ms. All other sequence parameters were kept identical to the cardiac-triggered scan. A non-selective perfusion scan with the cardiac-triggered, balanced PCASL scheme was collected as well.

Vessel movement: A single-slice 2D TOF was collected with the same TOF parameters in the label plane before each perfusion scan to detect any subject movement and to update the vessel location needed for accurate placement of the label spot (acquisition time = 2 s).

2.2.2.2 Study 2: Territorial perfusion fraction map

Territorial perfusion fraction maps were obtained in two additional healthy volunteers based on the results of study 1. The protocol started with a 2D TOF and a multi-phase pre-scan followed by a cardiac-triggered SS-PCASL of both carotid and vertebral arteries. The cardiac-triggered SS-PCASL was then adjusted to estimate labeling efficiency of each vessel directly above the label plane. Two image slices with a 18 cm FOV and 3mm slice thickness were positioned approximately 2 cm above the label plane. The label time was 500 ms and the post labeling delay 10 ms. Background suppression was turned off except for the fat suppression pulse. For each vessel, 2 pairs of label and control images were acquired with 4 interleaved shots using the same off-resonance compensation. All four arteries were collected sequentially in a single scan, resulting in a total acquisition time of ~2 min.

At the end of the protocol, phase-contrast MRI (PC-MRI) was acquired with the same slice prescription as the two slices used for labeling efficiency (gradient echo, TR/TE = 5.3/3.1 ms, voxel size = 0.43 x 0.43 x 4 mm^3, VENC = 100 cm/s, phase-encoding perpendicular to slice, 20 cardiac phases). Additionally, a 3D TOF of the circle of Willis was obtained for anatomical reference (gradient spoiled echo, TR/TE = 21/2.5 ms, voxel size = 0.43 x 0.43 x 1.5 mm^3, 2 slabs with a total of 118 slices, ARC acceleration factor = 2, acquisition time = 2 min 48 s).

2.2.3 Image post-processing and analysis

Image post-processing and analysis were performed in MATLAB. All SS-PCASL images were reconstructed to a 128-by-128 resolution via zero-padding in k-space. Label and control images were averaged and subtracted.

2.2.3.1 Study 1: Optimization of labeling efficiency

Off-resonance calibration: Perfusion images were first normalized by the proton density image. A relative labeling efficiency was calculated by dividing the vessel-selective by the non-selective perfusion images and masking the territory of the left ICA. The mask, which included gray and white matter, was created by manually defining the outline of the left ICA perfusion territory based on the mean vessel-selective perfusion image. Finally, a histogram of the relative labeling efficiency was least-squares fitted with a Gaussian function to estimate the mean relative labeling efficiency. The difference between calibration strategies was analyzed using a non-parametric Wilcoxon signed rank test with a significance threshold of 0.05.

Cardiac triggering: A quantitative comparison of the cardiac-triggered and non-triggered images was performed by selecting a single slice in the center of the volume and creating two ROIs: An "inside" ROI of the vertebral perfusion territory and an "outside" ROI of the small vessels distal to the middle cerebral artery (MCA) to capture arterial pulsatility artifacts. We calculated a spatial SNR (sSNR) and a temporal SNR (tSNR) in both ROIs. sSNR was defined as the mean signal over the spatial standard deviation outside the brain. tSNR was calculated as the mean signal over the temporal standard deviation within the ROI based on six pairwise subtraction images. Successful reduction of pulsatility artifacts was characterized by high SNR in the inside ROI and low SNR in the outside ROI. Furthermore, a contrast-to-noise ratio (CNR) was defined as the difference between the two ROIs divided by the temporal standard deviation outside the brain. A statistical comparison was performed with a non-parametric Wilcoxon signed rank test with a significance

threshold of 0.05. Additionally, a qualitative comparison was conducted by four expert observers. Each observer rated the pairs of cardiac-triggered and non-triggered images without prior knowledge of the acquisition method. Image quality was assessed by the delineation of the perfusion territory and by the amount of pulsatility artifacts outside the perfusion territory.

Vessel movement: Vessel movement was quantified by measuring the vessel center locations in each acquired 2D TOF image and calculating the absolute distance to the initial location at the beginning of the protocol.

2.2.3.2 Study 2: Territorial perfusion fraction map

Labeling efficiency of individual arteries: The vessel-averaged labeling efficiency was obtained by first calculating the labeling efficiency map α_{meas} based on the complex reconstructed SS-PCASL images above the label plane (Eq. 1). The "true" labeling efficiency was calculated by compensating for signal loss due to T_1-decay during transit on a voxel-by-voxel basis according to

$$\alpha_{true} = \alpha_{\text{meas}} \cdot \exp\left(\Delta_{sl}\, v^{-1}\, {T_{1,\text{art}}}^{-1}\right), \qquad (2.2)$$

where Δ_{sl} is the distance between label plane and the image slice, chosen such that all 4 vessels are intersected as perpendicularly as possible. The cardiac-averaged velocity field v was acquired with PC-MRI and co-registered to the mean subtraction image above label plane. The T_1-relaxation in arterial blood was set to $T_{1,\text{art}} = 1650\, ms$. Finally, each vessel was masked and a velocity-weighted average labeling efficiency was calculated.

For validation, a relative labeling efficiency was defined as the ratio of vessel-selective to non-selective vessel-averaged labeling efficiency. The relative labeling efficiency based on the measurements in the neck was then compared to the relative labeling efficiency based on the measured perfusion signal in the carotid territories of the brain (see section 2.3, study 1: off-resonance calibration).

Territorial Perfusion fraction map: Vessel-selective perfusion images were first scaled according to their average labeling efficiency. A median filter with a 4x4 window was applied to remove noise. The perfusion fraction map was calculated by dividing the efficiency-scaled vessel-

selective images by the total perfusion on a voxel-by-voxel basis. Total perfusion was defined as the sum of all efficiency-scaled vessel-selective perfusion images in order to yield a fraction sum of one. The resulting combined perfusion image was then visually compared to the measured perfusion image obtained with the non-selective method to ensure that all main feeding arteries were included. For reference, a standard color-coded territorial perfusion map was created by assigning each voxel a color based on the highest contributing artery.

2.3 Results

2.3.1 Off-resonance calibration

Fig. 2.1 shows the simulated mean vessel labeling efficiency for different label rotation schemes over a range of off-resonance frequencies. The labeling efficiency is robust for small amounts of off-resonance, but it significantly decreases for larger amounts of off-resonance. For an off-resonance frequency greater than 250 Hz, which corresponds to a phase accumulation of $\pi/2$, the order of label and control switch (negative mean labeling efficiency). Overall, the vessel-selective label schemes were more prone to a reduction in labeling efficiency due to off-resonance compared to the non-selective label scheme. The constant clockwise rotation scheme showed the highest labeling efficiency for small amounts of off-resonance. However, for larger amounts, the labeling efficiency of the constant clockwise scheme decreased faster compared to other label rotation schemes. The pseudo-random scheme offered the best results when large amounts of off-resonance are present, but showed diminished maximal labeling efficiency at small amounts of off-resonance. The fully-random scheme showed overall the lowest labeling efficiency. The constant clockwise scheme was chosen for all following in vivo experiments, given its superior labeling efficiency in combination with the proposed off-resonance compensation method.

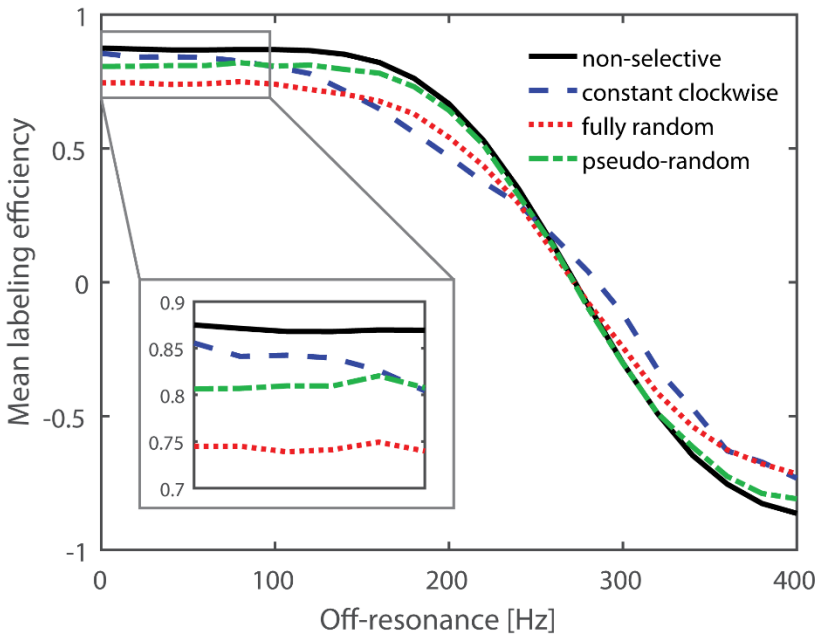

Fig. 2.1 Simulated mean labeling efficiency in the presence of off-resonance for different label rotation schemes. The close-up shows the difference in labeling efficiency between label rotation schemes for small amounts of off-resonance.

In the first part of study 1, an in vivo comparison of two off-resonance calibration strategies was performed. Fig. 2.2 illustrates the calculation of the off-resonance phase compensation based on a multi-phase pre-scan (a) and a field map (b). The results of the off-resonance calibration comparison are summarized in Fig. 2.3. Both multi-phase and field map calibrated SS-PCASL scans yielded statistically significant increases in labeling efficiency (Wilcoxon signed rank test, $P = 0.002$ and $P = 0.037$, respectively) compared to the non-calibrated scan (Fig. 2.3a). The multi-phase calibration consistently outperformed the field map calibration (Wilcoxon signed rank test, $P = 0.002$). The left ICA perfusion territory of two subjects is illustrated in Fig. 2.3b for each calibration strategy. For subject (1), both field map calibrated and non-calibrated scans had significantly reduced labeling efficiency, which resulted in difficulties to distinguish between perfusion signal and background noise. The multi-phase calibrated provided a clear image of the perfusion territory. Subject (2) presented with an anatomical variation of the circle of Willis, where the territory of the right anterior cerebral artery was perfused by the left ICA. This is an important perfusion detail which was difficult to identify in the non-calibrated scan. Both the multi-phase and field map calibrated scan achieved sufficient quality to identify the perfusion territory as well as capture the anatomical variation. The measured off-resonance phase corrections based on the multi-phase pre-scan and the field map are plotted in Fig. 2.4. A linear regression model revealed

a constant offset between the off-resonance phase obtained from the field map and the multi-phase pre-scan.

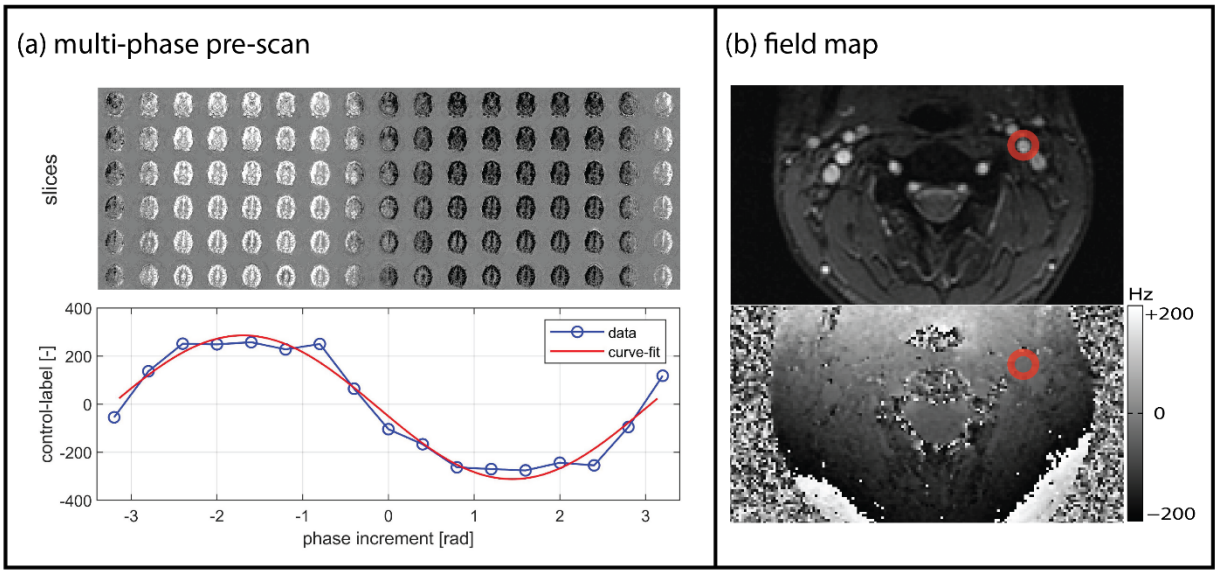

Fig. 2.2 Off-resonance calibration. **(a)** In the multi-phase pre-scan, the perfusion signal is measured for different amounts of added phase. Each column in the top image represents one phase increment, the rows correspond to different slice positions. The optimal phase correction was determined by a least-squares curve-fit with a sine-function. The blue line represents the average signal for each phase increment and the red line the curve-fit. **(b)** Based on the acquisition of a field map in the same location as the PCASL label plane, off-resonance was measured around the vessel of interest. First, a ROI was drawn manually in the magnitude image (top) and then applied to the frequency image (bottom).

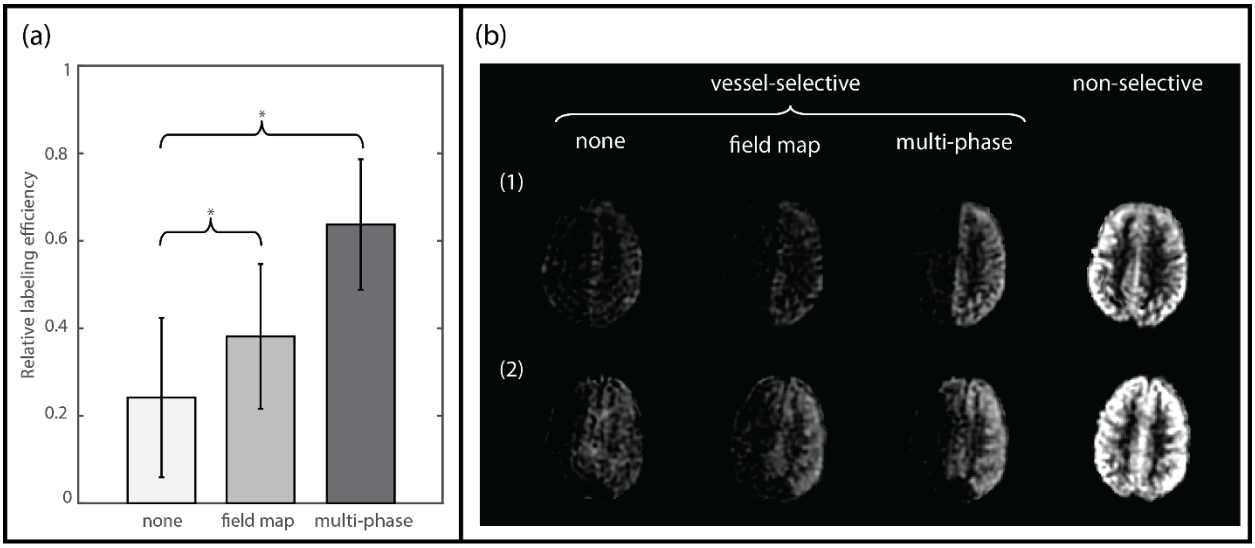

Fig. 2.3 **(a)** Quantitative comparison of the average relative labeling efficiency for three off-resonance calibration approaches (multi-phase pre-scan, field map, no calibration) over all subjects. The asterisk (*) represents a value of $P<0.05$ with the Wilcoxon signed rank test. The multi-phase calibrated scan consistently produced the highest signal, followed by the field map calibrated and

the non-calibrated scan. **(b)** Left ICA perfusion territory of two subjects for different off-resonance calibration strategies compared to a non-selective perfusion scan. Overall, the multi-phase calibrated scan yielded the highest amount of signal. Subject (1) yielded overall low perfusion signal for the field map and the non-calibrated scans, only multi-phase calibration resulted in an adequate representation of the territory. The same pattern was observed in subject (2), which presented with anterior collateral flow, best visible in the multi-phase calibrated scan.

2.3.2 Cardiac triggering

The efficacy of cardiac triggering on reducing pulsatility effects and improving overall image quality was investigated in study 1. A qualitative comparison of the cardiac-triggered and non-triggered mean subtraction images resulted on average in improved image quality with cardiac triggering (Fig. 2.5). A subject with improved outcome is shown in Fig. 2.6. The pairwise subtractions of the non-triggered acquisition displayed pulsatility artifacts around the middle and anterior cerebral arteries (white arrows), whereas the cardiac-triggered acquisition showed a significant reduction in pulsatility artifacts. A quantitative analysis of the cardiac triggering performance is shown in Fig. 2.7. Both sSNR and tSNR did not result in a significant change inside or outside the perfusion territory with cardiac triggering. However, there was a statistically significant improvement in CNR with cardiac triggering.

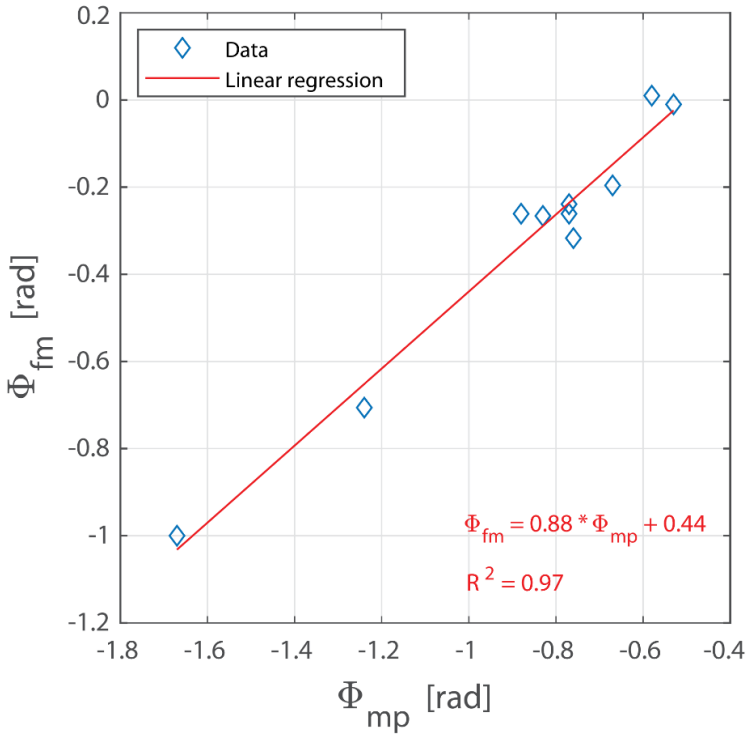

Fig. 2.4 Pairwise comparison of the off-resonance phase measured with the multi-phase pre-scan (mp) and the field map (fm). Data was fitted with a linear regression model.

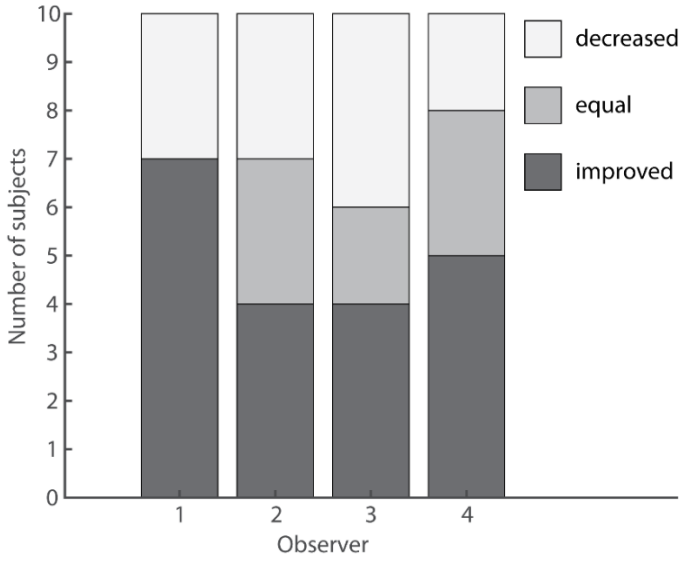

Fig. 2.5 Qualitative comparison of cardiac-triggered and standard non-triggered SS-PCASL. Changes in the image quality with cardiac-triggering were assessed by four expert observers and rated as improved, equal, or decreased.

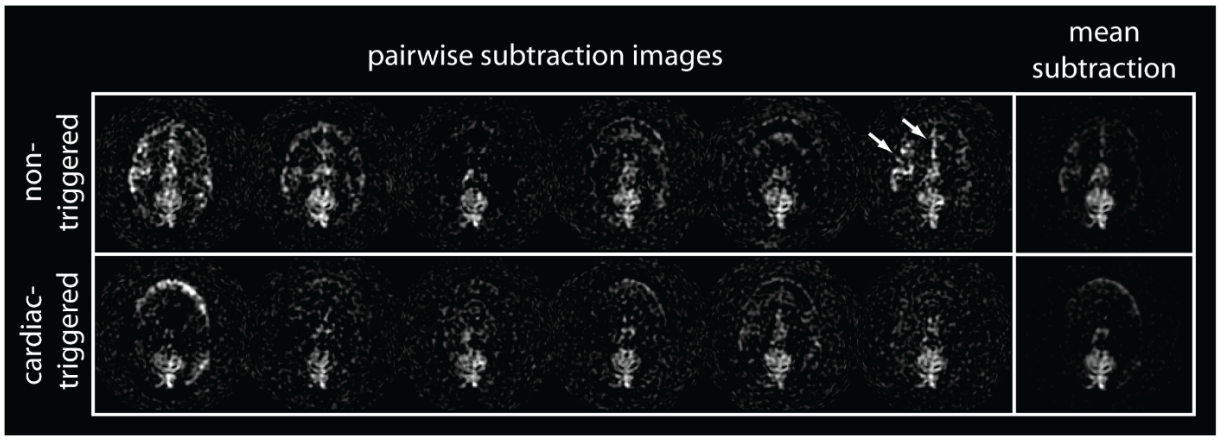

Fig. 2.6 Pairwise and mean subtraction images for a non-triggered and cardiac-triggered perfusion scan of the dominant vertebral artery in the same subject. White arrows indicate pulsatility artifacts in the middle and anterior cerebral arteries caused by the acquisition of control and label in different phases of the cardiac cycle.

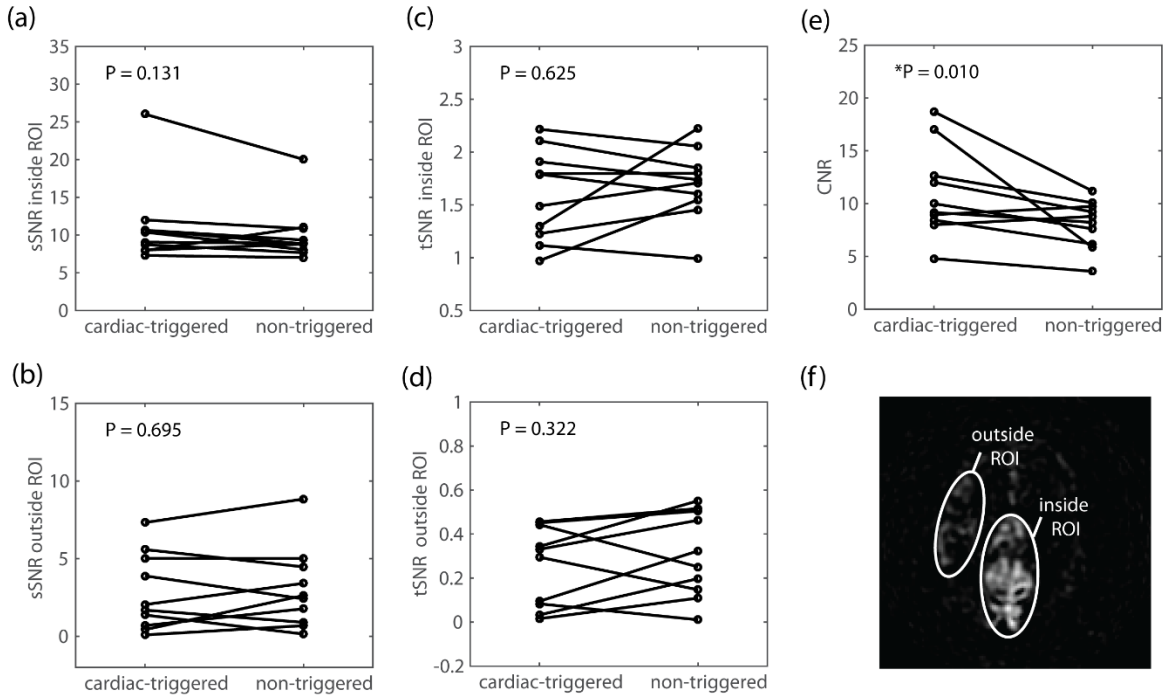

Fig. 2.7 Statistical comparison of cardiac-triggered and non-triggered SS-PCASL of the dominant vertebral artery. **(a)**, **(b)** sSNR inside and outside the posterior perfusion territory showed no statistically significant improvement with cardiac triggering. **(c)**, **(d)** Cardiac triggering did not result in a significant improvement in the temporal variance, represented by tSNR. However, there was statistically significant improvement (*) with cardiac triggering in CNR **(e)**. **(f)** Inside and outside ROI placement based on mean subtraction perfusion image of the vertebral artery.

2.3.3 Vessel movement

Fig. 2.8a shows the simulated mean labeling efficiency over a range of off-center vessel positions. Both carotid and vertebral arteries experience a steep drop in labeling efficiency for a vessel movement of more than 2mm relative to the center of the label spot. The maximum vessel movement measured during the in vivo scanning protocol in study 1 is shown in Fig. 2.8b. The median maximum movement measured over the group of subjects was below 2 mm, but half of the subjects had at least one vessel with more than 2 mm movement during the protocol.

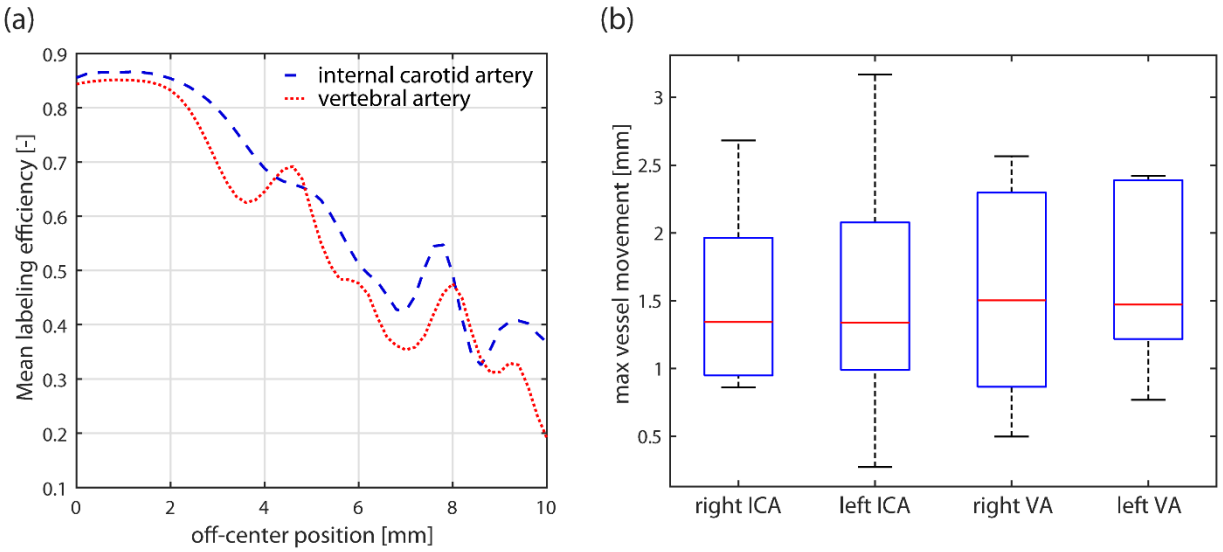

Fig. 2.8 **(a)** Bloch simulation results showing the impact of vessel movement on labeling efficiency for both carotid and vertebral arteries. **(b)** Maximal recorded vessel movement during in vivo scanning protocol over all subjects.

2.3.4 Territorial perfusion fraction map

Building on the results from the first in vivo study, we collected a full set of SS-PCASL images and measured the labeling efficiency in two additional subjects in study 2. The T1-decay compensated labeling efficiencies and the relative labeling efficiencies of the main feeding arteries in the neck are summarized in Table 2.1. The relative labeling efficiencies based on the measured signal above the labeling plane and the perfusion signal in the brain tissue showed good agreement for subject 1. For subject 2, there was an offset between the relative efficiencies. The post-processed territorial perfusion fraction maps alongside standard color-coded territorial maps are shown in Fig. 2.9. Subject 1 presented with ipsilateral perfusion patterns. The perfusion of the posterior circulation was dominated by the left VA, which was of increased caliber as confirmed by the TOF images. Subject 2 presented with an absent basilar artery. Perfusion to the posterior circulation was solely provided by the right ICA artery through the right posterior communicating artery. Again, these findings are in line with the anatomical data.

Table 2.1 Labeling efficiencies of the main feeding arteries in the neck. Measured and T1-decay compensated labeling efficiencies were based on the non-selective ($\alpha_{true,ns}$) and vessel-selective ($\alpha_{true,vs}$) PCASL scan above the label plane. The relative labeling efficiencies were defined as the ratio of vessel-selective to non-selective labeling efficiencies measured in the arteries ($\alpha_{rel,art}$) as well as the ratio of vessel-selective to non-selective perfusion signal at the tissue level ($\alpha_{rel,tiss}$).

	Subject 1				Subject 2			
Vessel	$\alpha_{true,ns}$	$\alpha_{true,vs}$	$\alpha_{rel,art}$	$\alpha_{rel,tiss}$	$\alpha_{true,ns}$	$\alpha_{true,vs}$	$\alpha_{rel,art}$	$\alpha_{rel,tiss}$
Right ICA	0.79	0.48	0.60	0.63	0.80	0.35	0.44	0.28
Left ICA	0.79	0.46	0.59	0.64	0.81	0.46	0.56	0.39
Right VA	0.53	0.40	0.75	-	0.48	0.45	0.92	-
Left VA	0.89	0.82	0.92	-	0.46	0.40	0.86	-

2.4 Discussion and conclusions

In this paper, we discussed several factors that significantly affect the quality of SS-PCASL acquisitions. We showed that off-resonance compensation, cardiac triggering, a constant clockwise rotation scheme, and vessel location tracking improved labeling efficiency and overall image quality. Furthermore, we presented a workflow to generate accurate territorial perfusion fraction maps by maximizing labeling efficiency and accounting for differences in labeling efficiency between vessels.

2.4.1 Off-resonance calibration

Study 1 revealed a significant increase in labeling efficiency for both the multi-phase and field map compensation strategies. Theoretically, both methods should yield the same optimal phase correction for off-resonance. However, the multi-phase calibration consistently yielded higher labeling efficiency and increased perfusion territorial accuracy compared to field map calibration scans. While the field map captures the presence of off-resonance due to B0-field inhomogeneity, the multi-phase pre-scan also accounts for additional imperfections in the magnetic field induced by the PCASL label train itself. This was reflected in the linear regression of the off-resonance phase measured with the multi-phase pre-scan and the field map, which showed a constant phase offset between the two methods. The most likely source for additional off-resonance is the presence of eddy-currents, caused by the fast switching of the slice-selective and vessel-selective gradients [61].

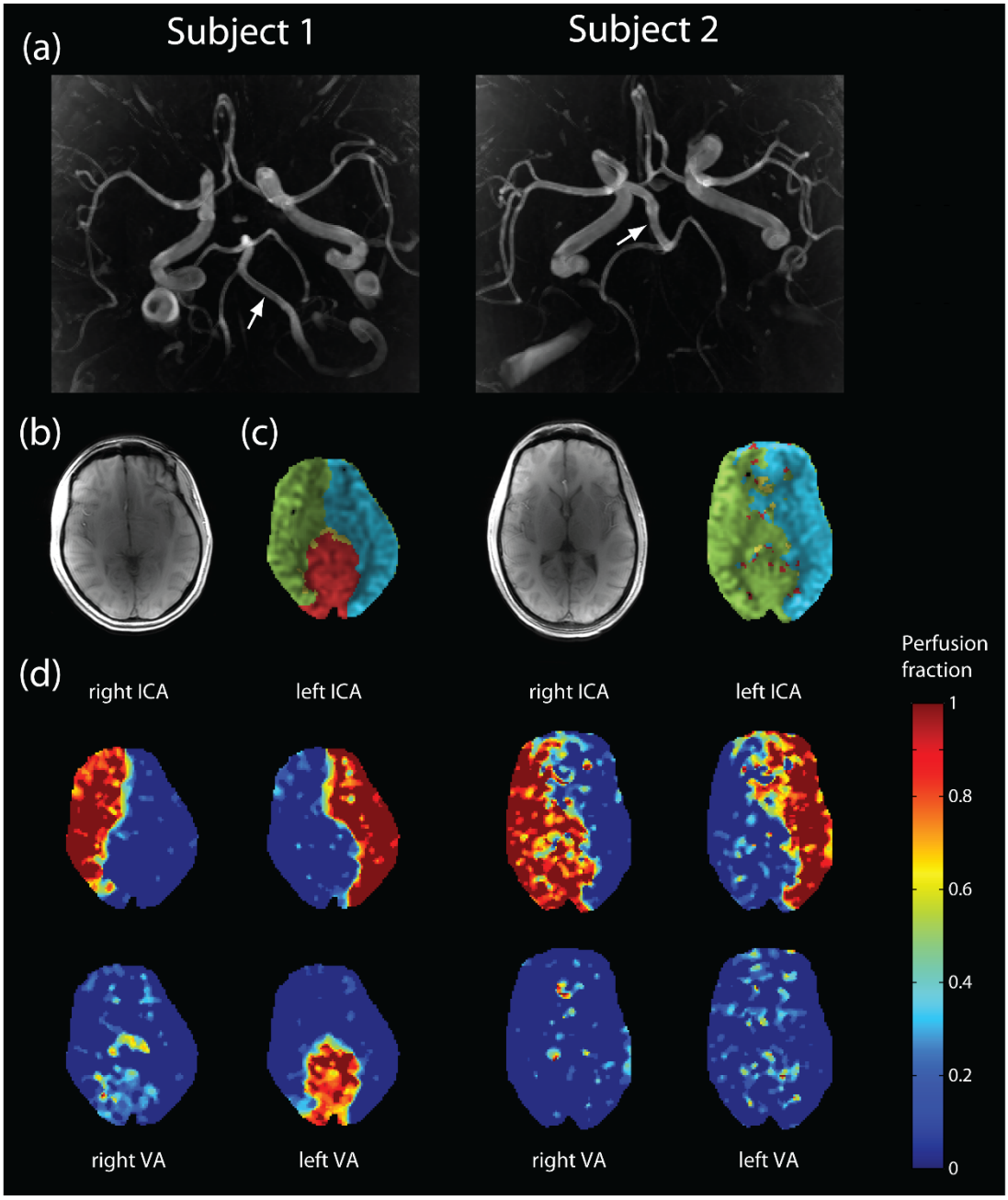

Fig. 2.9 Territorial perfusion in two subjects. **(a)** Axial MIP of TOF angiogram. **(b)** T1-weighted anatomical image. **(c)** Color-coded perfusion map based on the following color-coding: green = right ICA, blue = left ICA, yellow = right VA, red = left VA. **(d)** territorial perfusion fraction map of the neck arteries. Subject 1 presented with a posterior circulation dominantly perfused by left VA. TOF confirms increased caliber of left VA (arrow). Subject 2 presented with absent basilar artery. Posterior circulation is primarily perfused by right ICA (Arrow indicates the presence of the right posterior communicating artery with an increased caliber).

The multi-phase pre-scan used in this work was derived based on previous work. Jung et al. [59] proposed the acquisition of PCASL images over a range of phase increments with subsequent curve-fitting to generate the final perfusion images. However, SNR efficiency was reduced due to

a small number of averages per phase increment and the acquisition time was significantly increased. Shin et al. introduced a pre-scan procedure based on a multi-phase PCASL acquisition to estimate the ideal phase-correction for each vessel (OptPCASL) [62]. Additional to the estimation of a global phase correction, the amplitude and direction of in-plane gradients to compensate for off-resonance variations between vessels were calculated. However, this approach required prior knowledge of the vascular territory map. Here, we used a multi-phase pre-scan based on the estimation of an average phase correction over all vessels. In the presence of an off-resonance gradient between vessels, the accuracy of the calibration will be reduced. However, in our in vivo study, differences in off-resonance between vessels were negligible. As an alternative to the multi-phase pre-scan, a field map was used in this work to measure the off-resonance in the label plane directly. Jahanian et al. previously showed the benefits of estimating the off-resonance compensation in standard PCASL based on a field map [57].

Despite notable increase in labeling efficiency, the multi-phase calibration has so far not found widespread use in standard PCASL due to the additional time necessary for the acquisition (2:30 min) and post-processing (1 min) of the calibration scan. However, acquiring only a range of π should be sufficient to estimate the optimal phase correction in the future, which would cut the acquisition time in half.

While non-selective PCASL label schemes typically produce clinically usable images, even in the presence of moderate off-resonance, SS-PCASL label schemes are more susceptible to off-resonance (see Fig. 2.2). In vivo experiments showed that in the non-calibrated SS-PCASL scan, labeling efficiency was significantly decreased in some cases to the point where, the perfusion signal disappeared in the background noise.

The amount of off-resonance in the labeling plane is highly dependent on the applied shimming procedure. The standard pre-scan procedure, used in our protocol, only shimmed the image volume without the region of the label plane. While label plane shimming isn't available on our system, it might be on other scanners, which could significantly decrease the amount of off-resonance in the label plane and potentially eliminate the need for a calibration scan all together. Furthermore, when the labeling plane is within the shimmed imaged volume (e.g. labeling of intracranial arteries), off-resonance will also be significantly reduced. However, changes in the magnetic field induced by the SS-PCASL label train itself still need to be compensated for. Therefore, the use of a calibration

scan for SS-PCASL is highly recommended in situations where the label plane is outside the shimmed region.

2.4.2 Cardiac triggering

A qualitative inspection of the mean subtraction images showed a reduction in arterial artifacts and an overall improvement in image quality with cardiac triggering. The statistical comparison showed a significant improvement in CNR. However, no significant changes in temporal or spatial SNR were observed. One limiting factor of the analysis was that the temporal variance was based on only six pairwise subtractions. The success of cardiac triggering, more specifically the suppression of pulsatility artifacts, is highly dependent on the stability of the heart rate. A change in heart rate between label and control images can lead to imperfect subtractions and therefore artifacts like those present in non-triggered sequences. Movement of the pulse oximeter clip during the scan can further reduce the efficacy. Overall, Cardiac triggering increased the scan duration on average by 10%, depending on the heart rate. The effects of the cardiac pulsatility on labeling efficiency were previously studied by Verbree et al. [63]. The triggering of start-of-labeling as well as the end-of-labeling showed no significant change in labeling efficiency. Although cardiac triggering did not improve labeling efficiency, Li et al. showed that triggering the start-of-label train reduced temporal variance in non-selective PCASL [60]. While pulsatility artifacts are less visible in non-selective PCASL images, they do affect the accuracy of perfusion quantification. In SS-PCASL, pulsatility artifacts have an even larger impact on the image quality and more importantly the estimation of perfusion territories and fractional ratios.

2.4.3 Label rotation scheme

The constant clockwise rotation of the vessel-selective gradient blips between RF pulses resulted in the highest labeling efficiency for small amounts of off-resonance. For larger off-resonance, the pseudo-random rotation scheme, as recommended by Helle et al. [32], outperformed the constant clockwise rotation scheme. We decided to use the constant clockwise rotation scheme for all in vivo experiments since off-resonance was compensated. However, in scans without off-resonance calibration, the pseudo-random rotation scheme would be preferable.

2.4.4 Vessel movement

The success of SS-PCASL highly depends on the match between label spot and vessel position. A label spot size of 18 mm (FWHM) was chosen based on a number of previous experiments, which showed good selectivity for the majority of vessel anatomies in the neck. Generally, the label spot size should be as large as possible to maximize labeling efficiency, but as small as necessary to avoid labeling of neighboring vessels. For intracranial labeling, the label spot size will have to be reduced by increasing G_{xy} to account for the proximity of cerebral arteries. Based on the label spot size used in our setup, simulations showed a tolerance for a mismatch of approximately 2 mm. These results are in line with simulation and in vivo results reported in [32]. Here, we wanted to investigate vessel movement under realistic conditions. The acquisition of single-slice 2D TOFs in the label plane allowed us to track vessel movement throughout the protocol. The median maximum movement measured in the group of subjects was below 2 mm, but half of the subjects had at least one vessel with more than 2 mm movement. Movement generally increased towards the end of the scan, as subjects became less comfortable on the table. Vessel movement was only measured within the label plane. Motion in the slice-selection direction was not measured directly in this work. However, since the label plane was positioned in the part of the vasculature where both carotid and vertebral arteries are relatively straight, movement in the z-direction was assumed to have only minimal impact on the vessel location.

All the subjects in our study were healthy volunteers, capable of lying still for an extended time. In the clinical setting however, these ideal conditions will likely not be met, and the expected vessel movement will most likely be larger. It is therefore recommended to frequently update the vessel position for the SS-PCASL scan throughout the protocol.

2.4.5 Territorial perfusion fraction map

The overall goal of vessel-selective PCASL is to detect the outline of the perfusion territory and to calculate contributions of individual arteries to the overall perfusion in each voxel. Of particular clinical interest are areas of mixed perfusion. Kansagra et al. previously presented a post-processing method to calculate perfusion fractions of the carotid and basilar perfusion territories based on VE-PCASL [64]. Images were scaled based on a relative labeling efficiency (ratio of vessel-selective to non-selective perfusion signal) [31][64]. The method of calculating relative labeling efficiencies was also used in study 1 to compare different off-resonance compensation

strategies in the left ICA due to its straightforward calculation without the need for additional scans. Unfortunately, this method is only suitable to estimate the labeling efficiency of the carotid and basilar arteries. Due to the mixing of vertebral flow in the posterior cerebral arteries, the relative efficiency of each vertebral artery cannot be calculated based on the perfusion images alone. Here, we proposed a strategy to measure the labeling efficiency of all four vessels directly by acquiring images slightly above the label plane while the inverted spins are still in the arteries. Chen et al. [65] previously proposed a method to measure the labeling efficiency by tracking the outflow of the bolus in the image plane over time using a look-locker acquisition, which was then used to estimate the transit time in each voxel and to compensate for T1-decay. In this work, we acquired a single time point, assuming that the bolus was still fully present in the image plane. The bolus transit time was calculated based on direct measurements of velocity. The labeling efficiency was calculated by first dividing the complex subtraction of control and label image by twice the control image and then compensating for T_1-decay during transit. In order to minimize acquisition time of the labeling efficiency sequence, we made the assumption that measured signal in the arteries in the control image approximates the fully relaxed spin magnetization. This assumption was based on previous simulations showing the magnetization in the control state was approximately constant over a wide range of velocities. Furthermore, off-resonance was compensated during the acquisition. A comparison of the relative inversion efficiencies in the carotid arteries, obtained in the neck and at the tissue level, showed good agreement in subject 1 but resulted in an offset in subject 2. One possible explanation for this discrepancy is the temporal variation between subtraction images, which is only captured by the relative labeling efficiency based on the perfusion images.

Color-coded perfusion maps provide a straightforward illustration of the perfusion territories of individual arteries. However, it is rather difficult to extract quantitative information on mixed perfusion. Here, we calculated perfusion fractions by scaling the vessel-selective subtraction images based on the labeling efficiencies and dividing by the total perfusion. The scaled and smoothed territorial perfusion fraction maps showed the perfusion territory of each vessel clearly. The results in mixed perfusion territories such as the posterior circulation were in line with the anatomical properties revealed by the corresponding 3D TOF images. For accurate calculation of the perfusion fractions, it is important to ensure that all brain feeding arteries are included in the total perfusion. Here, we carefully inspected the TOF images for any anatomical variations or

collateral pathways. Furthermore, we visually compared the total perfusion based on the combined vessel-selective images with the non-selective perfusion images.

2.4.6 Intracranial labeling

While our investigation focuses on labeling the main brain-feeding arteries in the neck, SS-PCASL can also be used to label intracranially. Perfusion territory mapping of cerebral arteries can offer valuable clinical information for example in patients with intracranial stenosis or arteriovenous malformation [53]. Many of the discussed issues and solutions may still be applicable, however, there are some important differences to point out. First, with the label plane being within the shimmed region of the brain, the amount of off-resonance will likely be reduced. Second, for intracranial arteries the tolerance for movement may be different due to the smaller label spot size typically chosen to distinguish between neighboring arteries. Finally, pulsatility artifacts due to differences in blood volume during the acquisition will still be present. Therefore, some of the strategies proposed for labeling in the neck could also be beneficial for intracranial applications.

Chapter 3: A Combined Computational Fluid Dynamics and MRI Arterial Spin Labeling Modeling Strategy to Quantify Patient-Specific Cerebral Hemodynamics

3.1 Introduction

Cerebrovascular occlusive disease (CVOD), characterized by the presence of stenosis in the arteries supplying the brain, is a major risk factor for ischemic stroke. Clinical diagnosis and stratification of CVOD patients relies routinely on measuring the maximum narrowing of the lumen based on duplex ultrasound or computed tomography angiography (CTA). However, the degree of luminal stenosis is only one factor in the assessment of stroke risk. Plaque characteristics, downstream brain perfusion, and patency of collateral pathways also play an important role in the overall risk evaluation of cerebral ischemia [66][67][68]. Collateral flow in the circle of Willis (CoW) has been associated with reduced stroke risk in patients with severe carotid stenosis [69][70][71]. Collateral flow is highly dependent on the cerebral vasculature anatomy, availability of collateral pathways, degree of stenosis in the arteries supplying the brain and, critically, the condition of the cerebral microcirculation and its autoregulatory response [72][12].

The clinical gold standard for evaluating collateral flow is digital subtraction angiography (DSA). Despite providing high-resolution images of blood supply in the cerebral arteries, the procedure is invasive and strictly qualitative. MRI arterial spin labeling (ASL) has become an increasingly popular method for measuring cerebral perfusion, and it provides a non-invasive quantitative alternative to DSA. In non-selective ASL (NS-ASL), brain tissue perfusion is measured by magnetically labeling blood in the neck arteries and acquiring a series of slices of the brain after a short transit delay [50]. More recently, ASL has been extended to vessel-selective labeling to measure the perfusion territory of individual arteries [32][73]. The diagnostic capabilities of vessel-selective ASL (VS-ASL) have previously been demonstrated in patients with extracranial stenosis and arteriovenous malformation [46][53]. Additionally, cerebral angiograms have been performed based on VS-ASL to visualize blood supply in the cerebral arteries [74], rendering

similar qualitative information on cerebral flow patterns as DSA. Nevertheless, the information provided by VS-ASL on collateral flow patterns has thus far been qualitative.

Image-based computational fluid dynamics (CFD) provides a powerful tool for analyzing cerebral hemodynamics. Compared to experimental approaches, CFD renders velocity, pressure, wall shear stress, etc. throughout entire vascular territories with arbitrarily high spatial and temporal resolutions. The feasibility of CFD to assess cerebral hemodynamics has been previously demonstrated for intracranial stenoses [41][42] and aneurysms [43][44][45]. However, patient-specific calibration of cerebral blood flow CFD models remains challenging. Previous studies have heavily relied on literature data for determining flow splits in the CoW [75][76] or used simplistic allometric scaling assumptions to calibrate outflow boundary conditions [77].

In this paper, we propose a novel strategy to quantitatively characterize regional cerebral blood flow and perfusion using CFD in combination with PC-MRI and ASL data. First, a method to calibrate the cerebral blood flow CFD model based on NS-ASL perfusion data is presented. The calibration includes estimation of flow splits in the CoW from non-selective perfusion images and total inflow to the CoW from PC-MRI, followed by tuning of the outflow boundary conditions to match the estimated flow splits. Second, the calibrated CFD model is validated against territorial perfusion maps from VS-ASL based on the blood supply to each cerebral territory using Lagrangian particle tracking (LPT).

3.2 Material and methods

3.2.1 Patient details

Two CVOD patients and a healthy control subject were enrolled in a feasibility study and underwent a research MRI exam. The protocol was approved by the local Institutional Review Board and all subjects provided informed written consent (HUM00114275 and HUM00018426). The reconstructed geometric models of the three subjects are illustrated in Fig. 3.1. The models include the ascending and proximal descending thoracic aorta, its upper branches (brachiocephalic trunk, left carotid and left subclavian), the main neck arteries (internal and external carotids, vertebral arteries), and the main intracranial arteries including the CoW. The healthy control and patient 1 were reconstructed based on magnetic resonance angiography (MRA) and patient 2 based on CTA.

The healthy control subject (male, 28 y/o) presented without evidence of CVOD. The CoW anatomy was incomplete with both right and left posterior communicating arteries hypoplasia. Patient 1 (female, 55 y/o) presented with an asymptomatic 70-99% stenosis (duplex ultrasound, velocity criteria) in the right proximal internal carotid artery (RICA). The left internal carotid artery (LICA) was patent with no evidence of hemodynamically significant stenosis. Patient 1 has a complete CoW anatomy. Patient 2 (male, 64 y/o) presented with asymptomatic bilateral carotid stenosis. The RICA revealed a tandem stenosis of 80-90% (CTA, ECST criteria), stretching from the carotid bifurcation to the distal end of the carotid bulb. The LICA showed a 60% stenosis (CTA, ECST criteria). Patient 2 has an incomplete CoW anatomy with right P1 segment and distal right vertebral artery (RVA) hypoplasia.

3.2.2 Imaging data

All subjects underwent an MRI study to collect data on vascular anatomy, brain tissue perfusion, and flow. The protocol was performed at 3T (MR750; GE Healthcare, Waukesha, WI) with a 32-channel receive-only head coil for the head and neck and the scanner's build-in coil for the upper chest. At the end of the study, the subject's blood pressure was measured in the upper arm in the supine position.

3.2.2.1 Anatomy

Anatomical information from the ascending thoracic aorta to the carotid bifurcation level was acquired with a 2D T1-weighted spoiled gradient echo sequence (voxel size = 0.58 x 0.58 x 2 mm3, TR/TE = 75/3.3 ms). The remaining anatomy from the neck to the CoW was acquired with a 3D Time-of-Flight sequence (voxel size = 0.42 x 0.42 x 1.5 mm^3, TR/TE = 21/2.5 ms). Additionally, structural images of the brain were collected with a 2D T1-weighted spoiled gradient echo sequence (voxel size = 0.46 x 0.46 x 7 mm3, TR/TE = 100/3.0 ms). For patient 2, an additional CTA data of the neck and head vasculature was available (voxel size = 0.39 x 0.39 x 0.62 mm^3). For patient 2, the CTA dataset was chosen over the MRA for reconstruction due to the higher resolution.

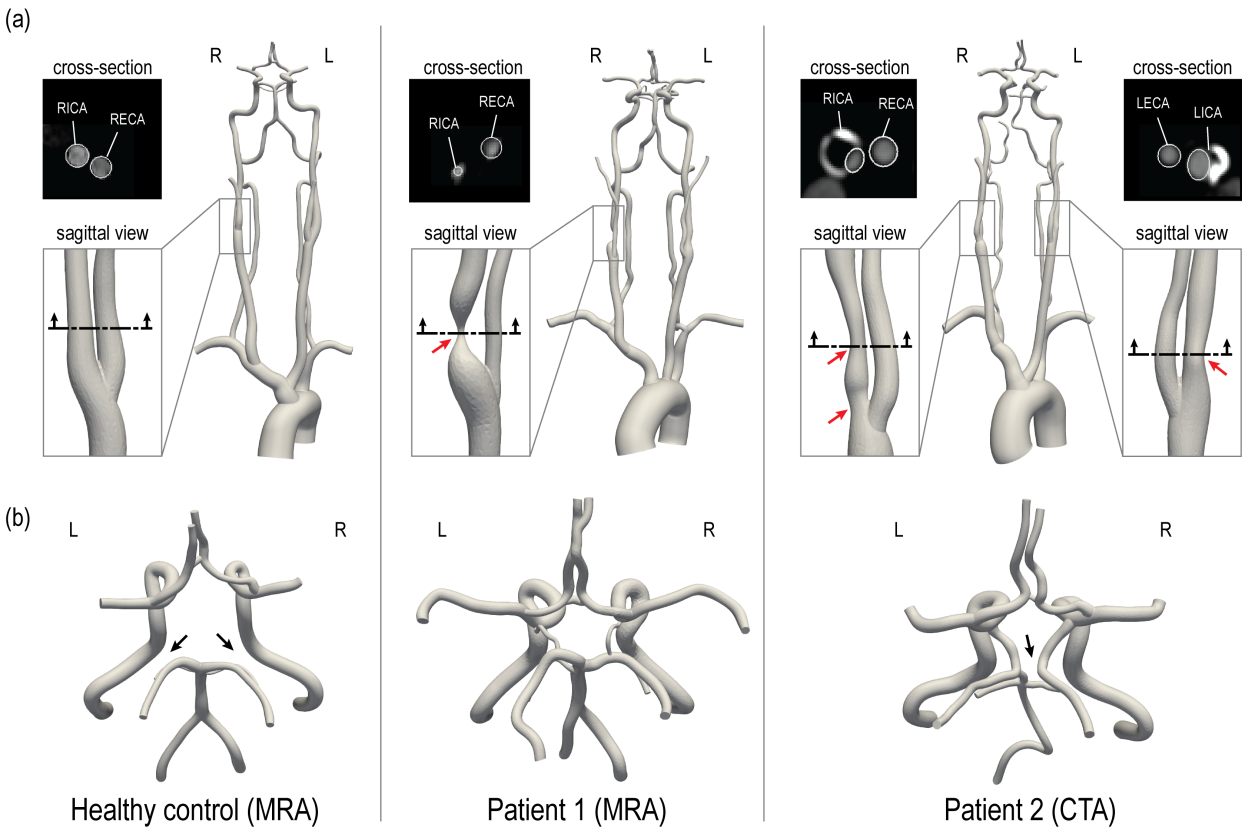

Fig. 3.1 3D-reconstructed geometric models of a healthy control and two CVOD patients. **(a)** For each patient, a close-up of the stenosis is shown. The red arrows indicate the location of the stenosis. An axial cross-section of the stenosis illustrates a comparison between image data and model contours (this comparison is also shown for the healthy volunteer). **(b)** Posterior view of the CoW. The black arrows indicate variations in the CoW anatomy. RICA = right internal carotid artery; RECA = right external carotid artery; LICA = left internal carotid artery; LECA = left external carotid artery. R and L indicate the right and left side from the subject's perspective.

3.2.2.2 Brain tissue perfusion

Using a pseudo-continuous ASL scheme, non-selective and vessel-selective cerebral perfusion images were collected. Prior to image acquisition, an off-resonance calibration pre-scan was performed to correct for B0-inhomogeneity in the label plane. For the NS-ASL acquisition, sequence parameters were set following consensus recommendations [50]: Label duration = 1800 ms, post-labeling delay = 2000 ms, TR/TE = 4600/4, voxel size = 3.75 x 3.75 x 7 mm^3, 3D spiral acquisition, 18 slices, 8 pairs of label/control images. The slice prescription was the same as for the T1-weighted structural images. The label plane was positioned above the carotid bifurcation where the arteries of interest (carotid and vertebral) run perpendicular to the plane and with a maximum distance between them. The start of the labeling period was cardiac-triggered to reduce pulsatility artifacts. A proton density image was collected, followed by a non-selective perfusion scan. Subsequently, four VS-ASL scans of the vertebral and carotid arteries were collected. The

position of vertebral and carotid arteries within the label plane was determined from the Time-of-Flight acquisition. Keeping all parameters of the NS-ASL scan unchanged, vessel-selective labeling was performed based on a super-selective labeling scheme [32], whereby additional in-plane gradients rotate clockwise every radiofrequency pulse to create a circular labeling spot. Finally, the vessel-selective labeling efficiency was measured by collecting an image 2 cm above the labeling plane 10 ms after labeling for 500 ms. Image reconstruction was performed in MATLAB to a resolution of 128 x 128 using zero-padding in k-space. The ASL perfusion signal was calculated by subtracting label and control images and averaging over all acquired pairs. A detailed explanation of the sequence setup and parameters can be found elsewhere [73].

3.2.2.3 Flow

Volumetric blood flow waveforms were measured using 2D cardiac-gated phase-contrast (PC-MRI) at the level of the ascending aorta (voxel size = 0.58 x 0.58x 5 mm3, TR/TE = 5.2/3.1 ms, velocity encoding = 130 cm/s) and above the carotid bifurcation (voxel size = 0.31 x 0.31x 5 mm3, TR/TE = 6.0/3.7 ms, velocity encoding = 100 cm/s). The slice was positioned perpendicular to the arteries of interest and velocity was encoded in the through-plane direction. PC-MRI data was processed in MATLAB to calculate flow rates.

3.2.3 Computational modeling

The key computational modeling tasks, namely three-dimensional anatomical reconstruction, mesh generation, boundary condition specification, and finite element analysis were performed using the validated open-source computational hemodynamics framework CRIMSON [78].

3.2.3.1 Anatomical reconstruction and mesh generation

3D geometric models of the aorta and head and neck vessels, including the CoW, were reconstructed from the anatomical imaging data. Briefly, centerlines and 2D vessel contours were defined for each vessel of interest. Contours were then lofted to create an analytical representation of each vessel and ultimately define a 3D geometric model of the vasculature [75]. This 3D model was then discretized using linear tetrahedral elements. A mesh-adaptation algorithm [79] was used to refine the mesh locally based on local velocity gradients. The final mesh sizes for healthy, patient 1, and patient 2 consisted of 2.16×10^6, 1.84×10^6, and 2.39×10^6 elements, respectively. Mesh-independence was evaluated for patient 1 by creating an additional highly-refined mesh with

$6.86x10^6$ elements, which resulted in a difference of less than 1% for the flow rates at each outlet and a maximum difference of 2 % for peak velocity in the center of the stenosis.

3.2.3.2 Boundary conditions

A pulsatile inflow waveform reconstructed from PC-MRI was mapped to a parabolic velocity profile and prescribed at the inlet of the ascending aorta for each geometric model. Each vessel outlet was coupled to a three-element Windkessel model, which consists of a proximal resistance (R_p), a distal resistance (R_d), and a capacitor (C) [80]. For each subject, the total arterial resistance is

$$R_T = P_{mean}/Q_T \quad (3.1)$$

where the mean pressure $P_{mean} = 1/3\ P_{systolic} + 2/3\ P_{diastolic}$ and Q_T is total cardiac output. The total arterial compliance is

$$C_T = \left(Q_{T,max} - Q_{T,min}\right)/\left(P_{systolic} - P_{diastolic}\right) * \Delta t \quad (3.2)$$

where $Q_{T,max}$ and $Q_{T,min}$ are maximum and minimum values of aortic inflow, and Δt is the time lapse between these values. Initial estimates for the Windkessel model parameters were obtained by distributing R_T and C_T among the different outlets, to obtain R_i and C_i for vessel $i = 1, \ldots, 13$, as described in [81]. The Windkessel parameters were then iteratively adjusted following the scheme described in detail in section 2.4. Lastly, a no-slip boundary condition was assigned to all vessel walls.

3.2.3.3 Finite Element Analysis

Blood was modeled as an incompressible Newtonian fluid with a dynamic viscosity of 0.004 $kg \cdot m^{-1} \cdot s^{-1}$ and a density of 1,060 $kg \cdot m^{-3}$. A stabilized finite-element formulation for the incompressible Navier-Stokes equations was employed to solve for blood flow velocity and pressure in the models [82]. Computations were performed using 80 cores on a high-performance computing cluster. Simulations were run using a time step size of 0.1 ms until cycle-to-cycle periodicity was achieved, typically after 5 cardiac cycles.

3.2.4 Patient-specific calibration of outflow boundary conditions for the CFD models

3.2.4.1 Calculation of mean flow at model outlets

Intracranial arteries: The flow distribution among cerebral and cerebellar arteries was derived from the NS-ASL perfusion images, a cerebral territory atlas, and the total inflow to the brain as illustrated in Fig. 3.2. First, the NS-ASL perfusion images were mapped into a standardized template space (Montreal Neurological Institute ch2better) using the toolbox SPM12 (Wellcome Trust Center for Neuroimaging, London, UK). Next, the standardized perfusion images were segmented using a vascular territory atlas. The vascular territory atlas was derived from a study by Kim et al. [83], in which the perfusion territories of the main cerebral arteries were mapped based on diffusion-weighted MRI in stroke patients. The atlas was extended to include the cerebellum. This extended vascular territory atlas with a resolution of 370 x 301 x 316 is given as a NIfTI dataset in the supplementary materials. In this work, we assumed the following relationship between eight intracranial arteries and seven vascular territories (see Fig. 3.2): 1) RACA territory, perfused by the RACA (yellow); 2) LACA territory, perfused by the LACA (magenta); 3) RMCA territory, perfused by the RMCA (green); 4) LMCA territory, perfused by the LMCA (light blue); 5) RPCA territory, perfused by the RPCA (orange); 6) LPCA territory, perfused by the LPCA (dark blue); 7) Cerebellum territory, perfused evenly by RSCA and LSCA (red). A perfusion split ps_j was then calculated by dividing the sum of perfusion signal in each territory $j = 1, \dots, 7$ by the sum of total perfusion signal over the entire brain. The total mean inflow to the CoW ($\bar{Q}_{CoW}$) was calculated from the PC-MRI data on left and right ICAs and VAs. Mean flow rates through each intracranial vessel ($\bar{Q}_{target,i}$) were calculated as the product of the total mean inflow to the CoW and the perfusion split ps_j corresponding to the territory perfused by vessel $i = 1, \dots, 8$.

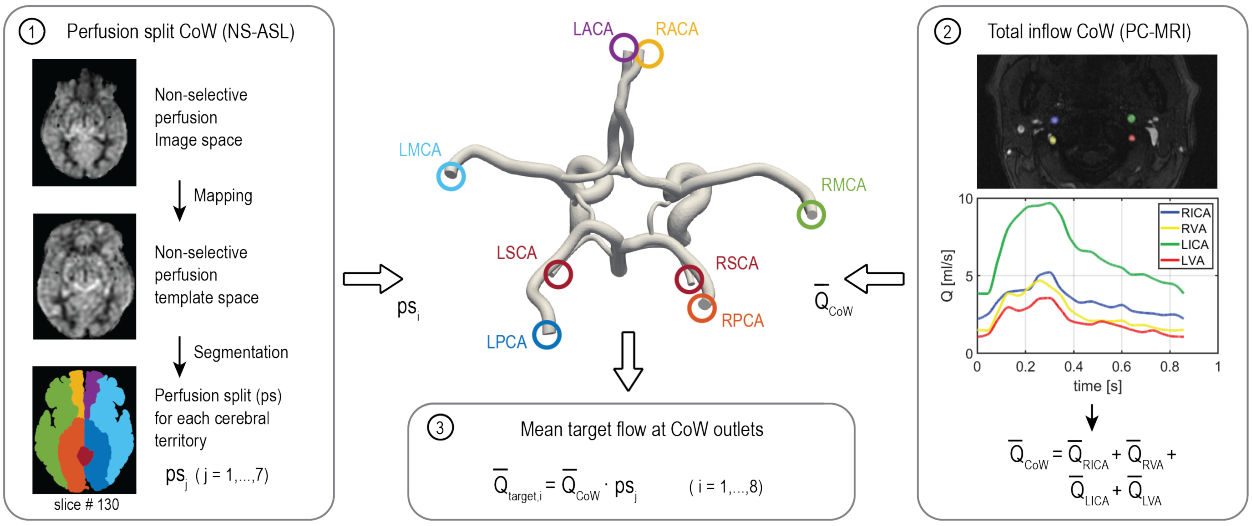

Fig. 3.2 Workflow of calculating the flow split among the arteries of the CoW based on NS-ASL perfusion imaging, a vascular territory atlas, and total inflow to the CoW from PC-MRI. RACA/LACA = right/left anterior cerebral artery, RMCA/LMCA = right/left middle cerebral artery, RPCA/LPCA = right/left posterior cerebral artery, RSCA/LSCA = right/left superior cerebellar artery.

Extracranial arteries: Mean flow rates in the external carotid arteries were calculated from PC-MRI. In the subclavian arteries, we assumed a mean flow rate of 5.6% of cardiac-output [75]. Finally, the difference between inflow and intracranial, external carotid arteries, and subclavian arteries flow was assigned to the descending thoracic aorta.

3.2.4.2 Calibration of Windkessel model parameters

Patient-specific calibration of the Windkessel model parameters for each outflow branch was performed in three stages. *Stage 1*: the distal resistance R_d was iteratively adjusted during simulation runtime using Python controller scripts [84] to match the target mean flow rates. At each simulation time step, R_d was adjusted proportional to the error between the current mean flow and the target flow. Simulations were terminated once the flow at each outlet was fully converged (error < 1%). Stage 2: The ratio of R_p/R_d was adjusted for each cerebral and cerebellar branch such that the computed and measured PC-MRI flow waveforms in the ICAs and VAs had similar pulsatility. The total resistance $R_i = R_p + R_d$ at each outlet was kept constant to preserve mean flow. Stage 3: Measurements of brachial pressure ($P_{systolic}$ and $P_{diastolic}$) were matched by adjusting R_T and C_T. The percentage change in R_T and C_T through the iterations was proportionally assigned to R_i and C_i at each outlet $i = 1, \dots, 13$.

3.2.5 Validation of the calibrated CFD models

The calibrated CFD models were validated against VS-ASL by comparing the fractional blood supply (FBS) in each vascular territory. We defined the fractional blood supply for a vascular territory j from a neck artery k as $FBS_{j,k} = Q_{j,k}/\sum_k Q_{j,k}$, where j = 1,..,7 is the vascular territory index and k = 1,..,4 is the neck artery index (1:RIVA , 2:RVA, 3:LVA, 4:LICA), and $Q_{j,k}$ is the flow contribution from the neck artery k to the vascular territory j. The process for calculating $FBS_{j,k}$ from VS-ASL and CFD data is described next.

3.2.5.1 Fractional blood supply based on VS-ASL

The process for calculating $FBS_{j,k}$ from VS-ASL images is outlined in Fig. 3.3. The perfusion signal in the VS-ASL images is determined by the blood supply from a single neck artery to the vascular territories. The signal in the VS-ASL images was first scaled based on the measured labeling efficiency. Then, scaled VS-ASL images were transformed into the standardized template space (panel 1). The sum of all scaled VS-ASL images produces the total perfusion image. The $FBS_{j,k}$ maps were then calculated by dividing each scaled VS-ASL image by the total perfusion image on a voxel-by-voxel basis (panel 2). Then, the $FBS_{j,k}$ maps were segmented into different territories using the vascular territory atlas. Lastly, due to noise in the raw ASL data, negative values of $FBS_{j,k}$ distribution are possible on a given voxel. Therefore, we characterize the $FBS_{j,k}$ distribution by its median (M) and median absolute deviation (MAD) (see panel 3).

3.2.5.2 Fractional blood supply based on CFD Lagrangian particle tracking

To validate the CFD results using the VS-ASL data, one must develop a method to assess the fractional blood supply of the intracranial arteries/territories and compare it with the median (M) of the $FBS_{j,k}$ obtained with VS-ASL for each artery/territory. This can be achieved via a further post-processing analysis on the CFD data, known as “Lagrangian particle tracking” (LPT), whereby virtual boluses of blood are created by seeding mass-less particles in different regions of the vasculature and advected by the velocity field over multiple cardiac cycles. This is an established technique with multiple applications in cardiovascular flows [85] [86] [87] [88] [89].

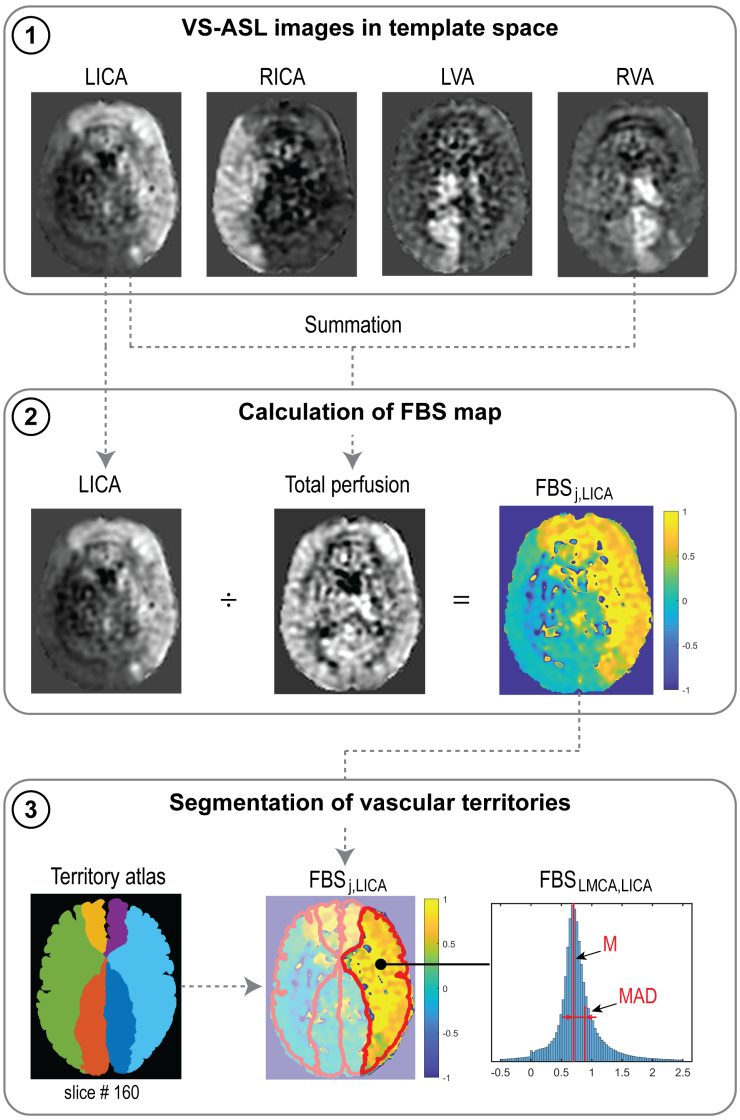

Fig. 3.3 Processes to calculate $\boldsymbol{FBS_{j,k}}$ from VS-ASL images, illustrated for the LICA. (1) Scaled VS-ASL perfusion images in standardized template space. **(2)** Calculation of spatial $\boldsymbol{FBS_{j,k}}$ maps. **(3)** Segmentation of territories using a vascular territory atlas and calculation of median (M) and median absolute deviation (MAD) from the $\boldsymbol{FBS_{j,k}}$ distribution in each territory.

In this work, we performed four individual LPT simulations, one for each carotid and vertebral artery. In each of the LPT simulations, a bolus was created by seeding particles continuously at the base of the corresponding neck artery (Fig. 3.4). To achieve continuous seeding, a small volume of particles was re-injected every 40 particle tracking steps. The volume of particles was defined by a disk with the radius of the seeding vessel and a height of approximately 2mm. The volume was discretized with a fine mesh, where each mesh vortex represents the seeding location of a particle. Particles were seeded and tracked over 4 cardiac cycles with a particle tracking time step size of 0.2 ms. After reaching the intracranial arteries, particles were counted at each outlet.

Once cycle-to-cycle periodicity in the number of counted particles was achieved, the total number of particles collected per intracranial vessel over a full cardiac cycle was extracted. The final particle count of each LPT simulation was scaled proportional to the flow rate of the seeding artery. This scaling step is necessary to keep the blood volume represented by a single particle constant across LPT simulations.

Lastly, for each intracranial vessel, assigned to a vascular territory j, itsfractional blood supply $FBS_{j,k}$ from each neck artery k was calculated by dividing the particle count of the LPT analysis for neck artery k by the sum of the particle counts of each of the four LPT analyses of the neck arteries.

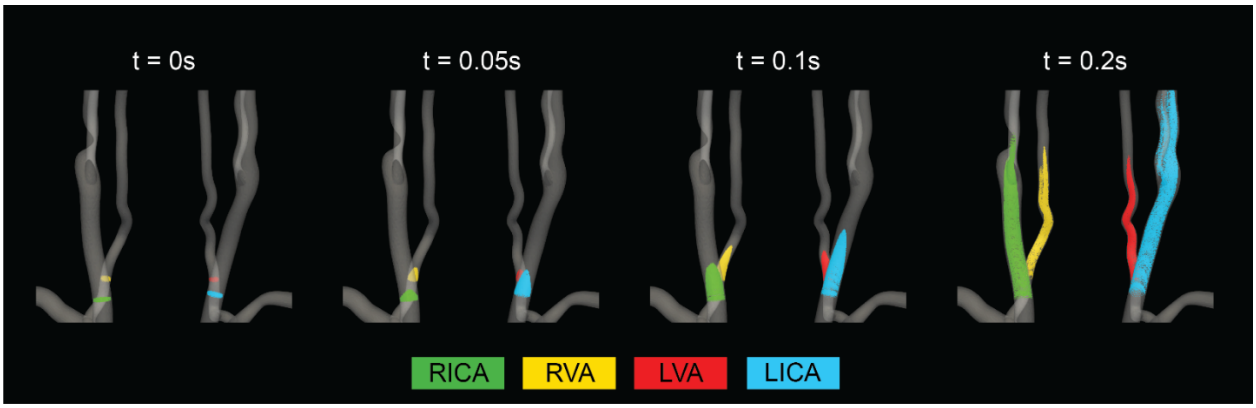

Fig. 3.4 Continuous seeding and advection of Lagrangian particles in the vertebral and carotid arteries at four time points.

3.3 Results

3.3.1 Validation fractional blood supply: CFD LPT versus VS-ASL

3.3.1.1 Qualitative analysis:

A qualitative comparison between FBS obtained from VS-ASL and CFD LPT is illustrated in Fig. 5. The VS-ASL images (Fig. 3.5a) show the perfusion territories of the four neck arteries, from the inferior region of the cranium (bottom row slices) to the superior region (top row slices). Each image voxel was color-coded based on the FBS of the neck arteries. For visualization purposes, we limited the FBS in each voxel to positive fraction values between 0 and 1 (cf. Fig. 3.3 panel 3). LPT analyses results (Fig. 3.5b) show maps of the advection of particles, color-coded based on the seeding artery in the neck, as well as temporal histograms of particles collected at the outflow of selected intracranial arteries.

1. Middle cerebral arteries: The VS-ASL data revealed that the perfusion territories of the RMCA (arrow 1) and LMCA (arrow 2) were primarily supplied by the ipsilateral carotid artery for all subjects regardless of the degree of stenosis. This perfusion pattern was also replicated in the LPT analyses, where particles exiting the RMCA primarily originated in the RICA (green particles) and particles leaving the LMCA predominantly originated in the LICA (blue particles).
2. Anterior cerebral arteries: All three subjects displayed flow compensation from the LICA to the RACA territory (arrow 3) in the VS-ASL images. The LPT analysis also reproduced this flow compensation in the RACA via the anterior communicating artery (AComA) for all subjects. The histograms of LPT RACA particles illustrate clear differences in the amount of compensation among subjects. The healthy control subject revealed significant blood supply from the LICA (blue particles) to the RACA, despite the absence of stenosis. The severe RICA stenosis in patient 1 resulted in the RACA being predominantly supplied by the LICA. In contrast, the severe stenosis in the RICA and the mild stenosis in the LICA in patient 2 only led to a small amount of collateral flow in the RACA.
3. Posterior cerebral arteries: The VS-ASL images revealed large differences in blood supply in the RPCA (arrow 4) and LPCA (arrow 5) territories between subjects. These differences in blood supply were also replicated in the LPT analyses. In the healthy control subject, the posterior circulation received mixed supply from both vertebral arteries as seen in the LPCA histogram. In patient 1, the RPCA territory was predominantly perfused by the LVA whereas the LPCA territory was predominantly perfused by the RVA (see histogram). The VS-ASL data revealed a switch in blood supply to the posterior circulation between right and left hemisphere, a switch also mirrored in the LPT analysis which shows vortex-like flow patterns in the basilar artery resulting in crossing of particles originating in the VAs. In patient 2, the posterior circulation was supplied by the ipsilateral carotid arteries. In this patient, the VAs did not contribute to cerebral blood flow. Instead, the LVA supplied most of the cerebellum flow with some small contribution from the LICA, as also apparent in the VS-ASL data (arrow 6).

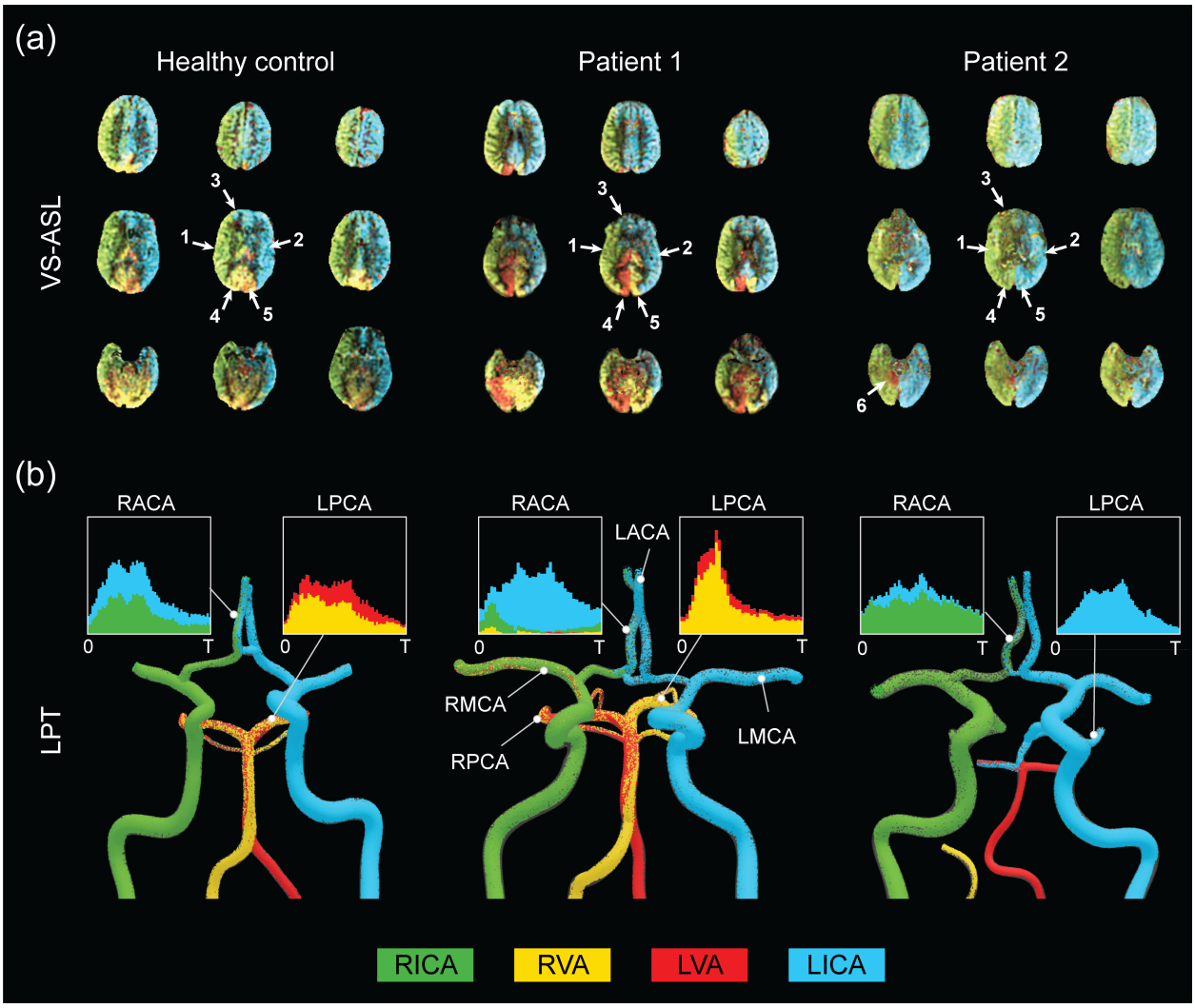

Fig. 3.5 Qualitative comparison between FBS obtained from VS-ASL and CFD LPT (a) VS-ASL images show the perfusion territories of the main neck arteries from the inferior of the cranium (bottom row slices) to the superior (top row slices). The images were created by color-coding the FBS maps of the main neck arteries on a voxel-by-voxel basis. For visualization purposes, we limited the fractional contributions of each neck artery to a positive range between 0 and 1. The arrows indicate the vascular territories of the 1) RMCA, 2) LMCA, 3) RACA, 4) RPCA, 5) LPCA, and 6) cerebellum. (b) LPT analyses show the advection of particles in the large arteries of the CoW. Particles are color-coded based on the artery of origin in the neck. Histograms demonstrate mixed supply in the RACA and LPCA over the cardiac cycle T.

3.3.1.2 Quantitative analysis

A quantitative comparison of $FBS_{j,k}$ obtained with VS-ASL and CFD LPT is summarized in Fig. 3.6. For each vascular territory j, the percentage supply contributions from the neck arteries k, obtained from VS-ASL (red bars) and LPT (blue bars), are shown. VS-ASL data includes the median absolute deviation. Due to noise in the VS-ASL signal, FBS results show small negative values in territories for which the perfusion contribution from a given neck artery k is small. Conversely, the LPT data is “noise-free” and given by a single value of FBS, instead of by a

distribution. Overall, VS-ASL and LPT estimates of $FBS_{j,k}$ agreed well for all subjects. The LPT analysis correctly identified the artery contributing the largest % of perfusion in vascular territories predominately perfused by a single neck artery in all subjects (e.g. LACA, LMCA, RMCA). Furthermore, the magnitude of flow compensation from the LICA to the RACA territory was correctly reflected in the LPT analyses for all subjects. The main sources of perfusion in the RPCA and LPCA territories were correctly identified by the LPT in both patients and only partially matched in the healthy control subject.

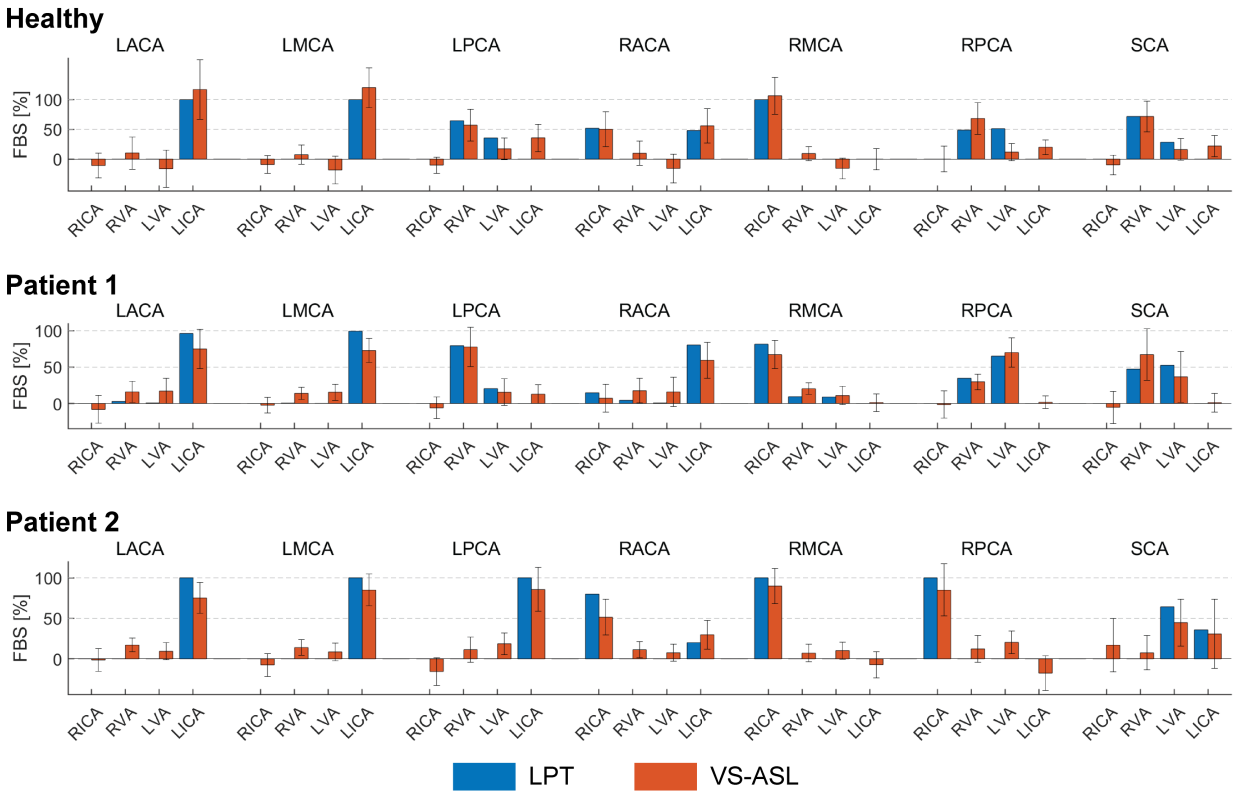

Fig. 3.6 Comparison of the $\boldsymbol{FBS_{j,k}}$, obtained from VS-ASL and LPT, in each vascular territory *j* and for each neck artery *k*. For VS-ASL, values of $\boldsymbol{FBS_{j,k}}$ represent the median of the $\boldsymbol{FBS_{j,k}}$ distribution in each vascular territory. The error bar represents the median absolute deviation. For LPT, values of $\boldsymbol{FBS_{j,k}}$ were calculated based on the particle count at each outlet of the CoW. RACA/LACA = right/left anterior cerebral artery, RMCA/LMCA = right/left middle cerebral artery, RPCA/LPCA = right/left posterior cerebral artery, SCA = superior cerebellar arteries, RVA/LVA = right/left vertebral artery, RICA/LICA = right/left internal carotid artery.

A correlation coefficient of $FBS_{j,k}$ between VS-ASL and LPT was calculated for each subject over all vascular territories *j* and neck arteries *k* (Fig. 3.7). The correlation coefficients were $R = 0.92$, $R = 0.94$, and $R = 0.95$ for the healthy subject, patient 1, and patient 2, respectively.

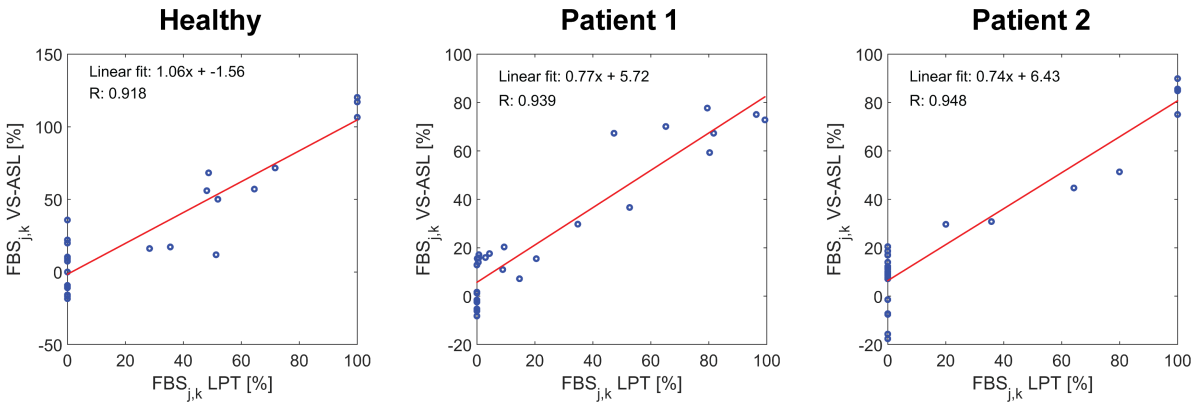

Fig. 3.7 Correlation of $\boldsymbol{FBS_{j,k}}$ between VS-ASL and LPT. For each subject, the correlation coefficient and linear fit of $\boldsymbol{FBS_{j,k}}$ over all territories *j* and neck arteries *k* was calculated.

3.3.2 Validation flow: CFD versus PC-MRI

Mean flow rates from the calibrated CFD model were compared to PC-MRI flow data in the vertebral and carotid arteries above the carotid bifurcation. The difference in mean flow rates in each neck artery was smaller than 10% for all subjects.

3.4 Discussion

3.4.1 Patient-specific calibration of outflow boundary conditions

We presented a strategy for calibrating patient-specific outflow boundary conditions in the CoW. Our strategy relies on deriving mean flow splits in the main arteries of the CoW using ASL perfusion data, and on knowledge of the total flow to the head given by PC-MRI data in the neck arteries. The perfusion data in the different cerebral territories is the result of the spatial distribution of blood supply to the brain tissue, which is determined by the overall distal microvascular resistance and potentially cerebral auto-regulatory effects that seek to compensate deficits in flow in a region of the brain. Therefore, the calibrated outflow boundary condition parameters include the effect of all these mechanisms. Cerebral auto-regulatory compensation was apparent in patient 1, where the ASL-derived flow rates in the right and left MCA of the CoW were comparable despite a severe RICA stenosis. To match the ASL-derived mean flow rates in the CFD analysis, the distal resistance of each Windkessel model for the vessels in the CoW was iteratively adjusted during stage 1 of the calibration (cf. section 3.2.4.2). The calibrated RMCA resistance was significantly lower than its LMCA counterpart. This finding points to a substantial vasodilation of the distal vasculature of the RMCA to maintain adequate blood supply to the brain tissue.

Previous CFD modeling studies of cerebral blood flow have relied primarily on assumptions on the flow distribution in the CoW, either based on literature data of healthy vasculatures [75][76] or allometric scaling laws [77]. However, in situations of cerebrovascular disease, the distribution of flow between the different vessels of the CoW may be substantially different from that given by idealized allometric scaling principles based on healthy data. Ultimately, incorrect values of flow in the vessels of the CoW will affect the quality of the CFD results. Zhang et al. [90] previously presented a calibrated 1D-0D computational model of cerebral blood using single photon emission computed tomography (SPECT) to estimate the flow distribution in the CoW [91]. In this work, we built on this approach by acquiring non-invasive and non-radioactive NS-ASL perfusion images and using 3D models of blood flow, given by the incompressible Navier-Stokes equations, which are essential to capture complex hemodynamics around the stenosis and in the small and tortuous vessels of the CoW.

3.4.2 Validation of calibrated CFD model

In this work, we demonstrated that our CFD calibration strategy of using NS-ASL perfusion images, in combination with a vascular territory atlas and PC-MRI, can accurately characterize flow in the main arteries of the CoW in a small group of subjects. The LPT analysis performed using the calibrated CFD model was validated using VS-ASL data by comparing their respective values of FBS in each vascular territory. Results showed an overall good agreement between LPT and VS-ASL with high correlation coefficients.

Bockman et al. [77] developed a CFD model of the vertebrobasilar system with outflow boundary conditions defined via allometric scaling on healthy subjects without flow-altering CVOD. They studied the agreement in the laterality of the VA blood supply for the cerebral and cerebellar circulations between CFD and vessel-encoded ASL. ASL perfusion data was therefore not used to calibrate the outflow BC of the CFD model. Here, we modeled the entire CoW and validated blood supply to each vascular territory in both healthy and CVOD subjects. Furthermore, we demonstrated that the calibrated CFD models captured the collateral flow observed in the VS-ASL data.

3.4.3 Limitations

Vascular territory atlas: Estimating the flow splits between the main arteries of the CoW and, consequently, calibrating the corresponding outflow Windkessel models, relies on the segmentation of non-selective ASL perfusion images using a vascular territory atlas. The atlas was derived from a large population study and represents a map of the average vascular territories in the brain. Although the size of border zones between territories appears to be much narrower than previously assumed [83], a degree of variability in the vascular territories between patients is expected. Furthermore, leptomeningeal collaterals can form between the distal branches of the CoW to augment flow compensation in cases of severe stenosis [92], thereby altering the vascular territories of the main cerebral arteries. To assess the accuracy of the atlas in the subjects of our study, we could qualitatively compare their boundaries against the outlines of the perfusion VS-ASL data, see Fig. 3.3, maps of territorial atlas and $FBS_{j,LICA}$ for slice 160.

VS-ASL: Perfusion quantification from ASL images is challenged by its inherently low signal-to-noise ratio, pulsatility artifacts, and sensitivity to bolus arrival time variation. Although NS-ASL is rapidly gaining acceptance in the clinic, quantification of perfusion is not readily available in all scanner platforms and the technique is generally used qualitatively in the clinical setting [50]. In VS-ASL, these challenges can lead to artifacts in the territorial perfusion maps [73]. For example, signal fluctuations between label and control images can result in spurious perfusion signal in vascular territories not perfused by the labeled neck artery, and consequently lead to errors in the calculation of the FBS. To account for the spatial variability of FBS within a vascular territory, we included the median absolute deviation in the data as shown in Fig. 3.6.

3.5 Conclusion

In this work, we presented a strategy to quantify cerebral hemodynamics using CFD in combination with ASL and PC-MRI data. We demonstrated that our calibrated CFD model accurately reproduced the fractional blood supply to the vascular territories, as obtained from VS-ASL. In particular, the flow compensation between hemispheres was captured well by the calibrated CFD models.

Chapter 4: Patient-Specific Computational Modeling of Cerebral Hemodynamics in Patients with Carotid Stenosis

4.1 Introduction

Clinical assessment of patients with carotid stenosis generally relies on categorizing the severity of the stenosis based on the degree of diameter reduction. Yet, hemodynamic factors, including the patency of collateral flow compensation and the cerebral vascular flow reserve, are also known to play an important role in the pathophysiology of Transient ischemic attack (TIA) and ischemic stroke [51]. Strokes in patients with high level stenosis (80%-99%), especially in combination with inadequate collateralization, are more likely to have a hemodynamic etiology due to critical reduction in ipsilateral blood supply to the brain tissue exceeding the limits of the cerebral vascular flow reserve [93]. Furthermore, cerebral hemodynamics might play a key role in the prevention of embolic stroke, as the presence of patent collaterals has been associated with a reduced risk of hemispheric stroke and TIA in symptomatic patients [69][71][70]. While the pathophysiology is not fully understood, it has been hypothesized that collateral flow and overall adequate cerebral perfusion are beneficial in the clearance or washout of emboli [94]. Given the complexity of the cerebral vasculature and the mechanisms of flow compensation, a better understanding of cerebral hemodynamics is needed.

Unfortunately, clinically available imaging modalities provide only a snapshot of cerebral hemodynamics and are limited to velocity measurements (transcranial doppler, 4D flow). To evaluate patency of collateral flow compensation, collateral vessels are typically graded based on anatomical data (computed tomography angiography (CTA), magnetic resonance angiography (MRA), digital subtraction angiography (DSA)). However, quantitative information about the blood supply to the vascular territories of the brain and the collateral flow contributions are currently not available.

The aim of this study is to demonstrate a novel method of quantifying cerebral hemodynamics using computational fluid dynamics (CFD) combined with medical imaging data. We previously

presented a strategy of calibrating patient-specific CFD models using brain perfusion data obtained from arterial spin labeling (ASL) MRI, which was validated in a small cohort of subjects [95]. Here we perform patient-specific CFD analysis to characterize the preoperative cerebral hemodynamics in two patients with carotid stenosis and to investigate the hemodynamic impact of anatomy, stenosis progression, and collateralization. Additionally, the changes in cerebral hemodynamics following carotid revascularization are assessed in a single patient.

4.2 Methods

4.2.1 Patient history

Two patients with carotid stenosis were recruited from the vascular surgery unit at the University of Michigan Hospital. The study was approved by the local Institutional Review Board and all subjects provided informed written consent (HUM00114275).

Patient 1 (female, 55 y/o) presented with a symptomatic 70-99% stenosis of the proximal right internal carotid artery (RICA) based on duplex ultrasound (DUS). The left internal carotid artery (LICA) was patent with no evidence of stenosis following carotid endarterectomy (CEA) one year prior to this study. Patient 1 presented with a complete Circle of Willis (CoW) anatomy. CEA with patch angioplasty was performed on the RICA

Patient 2 (male, 64 y/o) presented with an asymptomatic 80-90% tandem stenosis of the proximal RICA and an asymptomatic 60% stenosis of the proximal LICA, based on CTA. This patient had an incomplete CoW anatomy with a missing right P1 segment and an atretic distal right vertebral artery (RVA). CEA with patch angioplasty was performed on the RICA.

4.2.2 Imaging data

The two patients underwent an MRI study to acquire data on vascular anatomy, flow, and brain tissue perfusion. Patients 1 and 2 received preoperative MRI scanning 46 days and 12 days prior to undergoing right CEA, respectively. Patient 2 received an additional MRI scan 56 days post operation.

Anatomical information of the vasculature of the thoracic aorta and complete cerebral vasculature was acquired with a combination of 2D T1-weighted spoiled gradient echo and 3D Time-of-Flight. Additionally, CTA data of the neck and head region was acquired preoperatively as part of the clinical treatment of patient 2. Flow rates were measured in the ascending aorta and in the main

cervical arteries above the carotid bifurcation via phase-contrast (PC) MRI. Brain tissue perfusion data was collected using ASL MRI. The ASL sequence included a standard non-selective labeling scheme to acquire total perfusion maps [50] and a vessel-selective labeling scheme to acquire the regional perfusion territories of the main neck arteries (carotid and vertebral arteries) [32][73]. At the end of the MRI protocol, non-invasive cuff pressure measurements of the right upper extremity were acquired while in the supine position. Further details about the imaging protocol are described in chapter 3.2.2.

4.2.3 Patient-specific computational modeling

Image-based CFD allows for the analysis of hemodynamics in patient-specific geometries by solving the governing equations of flow motion. In this work, CFD analysis of cervical and cerebral hemodynamics was performed in preoperative models of patients 1 and 2 and in a postoperative model of patient 2. Computational modeling was performed using the validated open-source computational hemodynamics framework CRIMSON [78]. The modeling steps and parameters have been described in detail in chapter 3.2.3. Briefly, 3D geometric models of the cervical and cerebral vasculature were reconstructed using the preoperative anatomical MRI data of patient 1 and the CTA data of patient 2. The postoperative geometric model of patient 2 was created by adapting the preoperative geometric model in the region of the right carotid bifurcation based on the postoperative anatomical MRI data to reflect the anatomical changes following CEA. Patient-specific boundary conditions were specified at each model inflow and outflow. A volumetric flow waveform, reconstructed from PC-MRI, was imposed at the inflow of the ascending aorta. 3-element Windkessel models, representing the resistance and compliance of the distal vasculature, were assigned at each outflow. To calibrate the Windkessel model parameters, the mean flow rates in the intracranial arteries were derived from ASL perfusion and PC-MRI data using a previously proposed calibration strategy [95]. Briefly, ASL perfusion images were segmented into the vascular territories, corresponding to the anterior cerebral artery (ACA), middle cerebral artery (MCA), posterior cerebral artery (PCA), and superior cerebellar artery (SCA), using a vascular territory atlas and a perfusion split over the vascular territories was calculated. The final mean flow rates were calculated by distributing the total mean inflow to the CoW, obtained from PC-MRI, among the vessel of the CoW proportionally to the derived perfusion splits. The mean flow rates in the subclavian arteries were assumed to be 5.6% of cardiac-output [75] and the mean flow rates in the extracranial carotid arteries were calculated directly from PC-MRI. The mean

flow rate in the descending aorta was defined as the difference between the inflow at the ascending aorta and the cervical and cerebral outflows combined. Finally, the Windkessel model parameters were iteratively tuned to match the CFD flow rates to the calculated target mean flow rates and the pulsatility of the PC-MRI waveforms above the carotid bifurcation. The Windkessel model parameters were further tuned to match the cuff pressure measurements. The final Windkessel model parameters for each patient model are summarized in Table 4.1. Blood was modeled as an incompressible Newtonian fluid with a dynamic viscosity of 0.004 $kg \cdot m^{-1} \cdot s^{-1}$ and a density of 1,060 $kg \cdot m^{-3}$. Computations were performed using the CRIMSON Navier-Stokes Flow solver on 80 cores at the University of Michigan high-performance computing cluster ConFlux. Simulations were run using a time step size of 0.1 ms until cycle-to-cycle periodicity was achieved, typically after 5 cardiac cycles. Velocity and pressure fields were extracted for the last cardiac cycle.

To visualize and quantify the blood supply from the cervical arteries to the CoW, a further post-processing analysis on the CFD data, known as "Lagrangian particle tracking" (LPT) was performed [85][86]. Virtual boluses were created by seeding massless particles continuously at the root of each cervical artery and advecting the particles with the velocity field over multiple cardiac cycles. Particles were counted at each outlet over the last cardiac cycle.

Table 4.1 Parameters of the calibrated 3-element Windkessel models for patients 1 and 2. Each Windkessel model consists of a proximal resistance $\boldsymbol{R_p}$, distal resistance $\boldsymbol{R_d}$, and compliance $\boldsymbol{C}$. RECA/LECA = right/left external carotid artery, RACA/LACA = right/left anterior cerebral artery, RMCA/LMCA = right/left middle cerebral artery, RPCA/LPCA = right/left posterior cerebral artery, RSCA/LSCA = right/left superior cerebellar artery, RVA = right vertebral artery.

Outlet	Patient 1			Patient 2		
	$\mathbf{R_p}$ $(10^9 \mathrm{Pa\,s\,m^{-3}})$	$\mathbf{R_d}$ $(10^9 \mathrm{Pa\,s\,m^{-3}})$	$\mathbf{C}$ $(10^{-10} \mathrm{m^3 Pa^{-1}})$	$\mathbf{R_p}$ $(10^9 \mathrm{Pa\,s\,m^{-3}})$	$\mathbf{R_d}$ $(10^9 \mathrm{Pa\,s\,m^{-3}})$	$\mathbf{C}$ $(10^{-10} \mathrm{m^3 Pa^{-1}})$
Descending Aorta	0.01	0.23	63.72	0.01	0.26	54.52
R. subclavian	0.13	2.68	5.50	0.17	3.24	4.43
L. subclavian	0.13	2.63	5.50	0.17	3.24	4.43
RECA	0.49	5.69	2.44	0.42	4.90	2.89
LECA	0.85	10.01	1.42	0.64	7.46	1.89
RACA	2.38	2.38	2.09	4.72	8.01	1.18
LACA	2.11	2.11	2.42	5.76	6.23	1.26
RMCA	0.15	1.55	5.31	2.10	3.54	2.76
LMCA	1.27	1.27	5.60	2.61	2.83	2.86
RPCA	4.22	4.57	1.62	7.51	12.63	0.77
LPCA	4.37	4.73	1.55	8.61	9.33	0.86
RSCA	1.32	14.59	0.91	6.11	15.79	0.69
LSCA	1.32	14.03	0.91	6.14	15.85	0.69
Terminal RVA	-	-	-	7.09	17.09	0.61

4.3 Results

4.3.1 Geometric patient models

The reconstructed geometric models of the main arteries from the thoracic aorta to the CoW are illustrated in Fig. 4.1 for patients 1 and 2. A cross-sectional comparison of geometric model at peak RICA stenosis revealed a remaining luminal diameter of 1.4 mm and 3.0 mm for patients 1 and 2 respectively. The lumen of the proximal RICA was fully restored following CEA of patient 2.

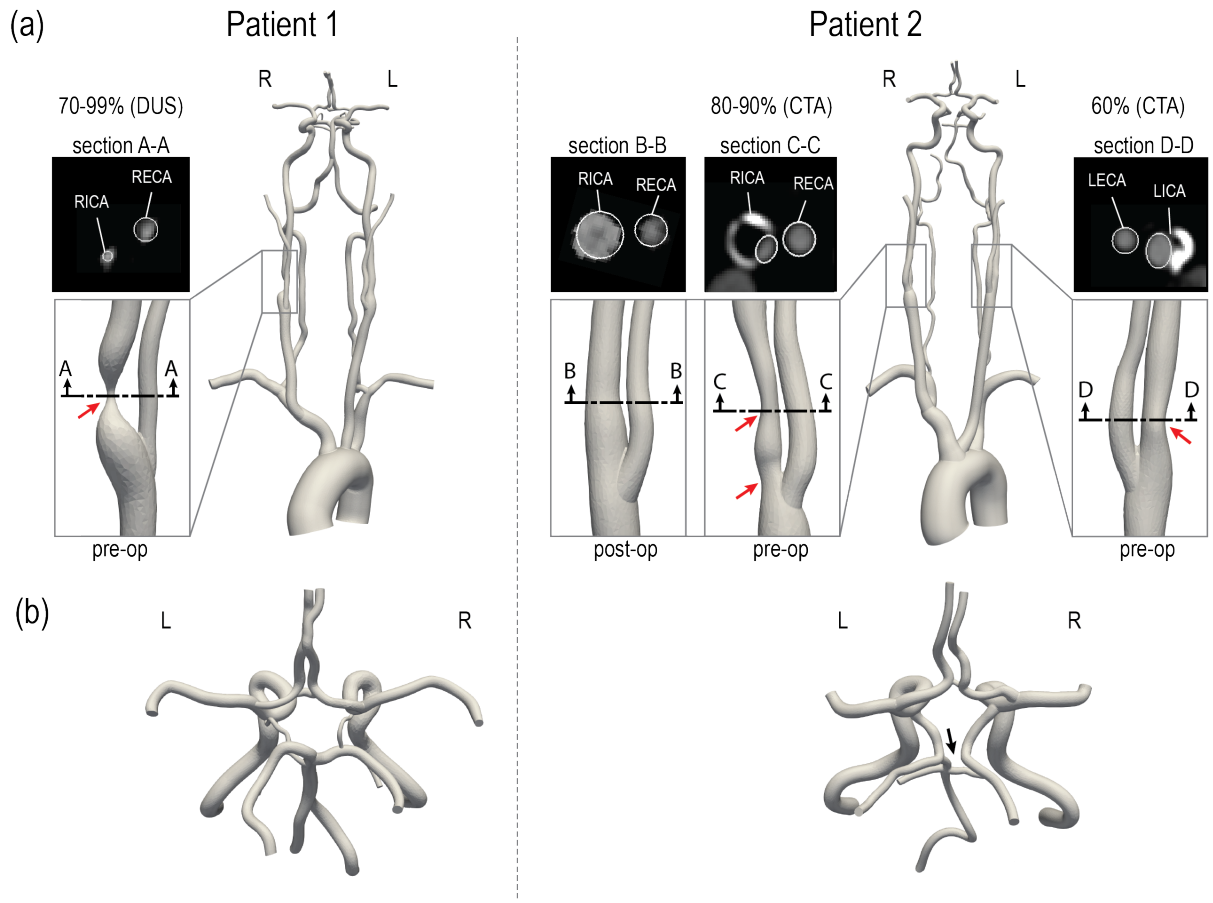

Fig. 4.1 3D-reconstructed geometric models. **(a)** Close-up of the stenosed carotid bifurcations. The red arrows indicate the location of peak stenosis. An axial cross-section illustrates the comparison between image data and model contours. **(b)** Posterior view of the CoW. The black arrows indicate variations in the CoW anatomy. RICA = right internal carotid artery; RECA = right external carotid artery; LICA = left internal carotid artery; LECA = left external carotid artery. R and L indicate the right and left side from the subject's perspective.

4.3.2 Preoperative hemodynamic analysis

After establishing the accuracy of our CFD-ASL modeling strategy against VS-ASL and PC-MRI data (see chapter 3.3), we investigated its clinical feasibility to assess preoperative hemodynamics in patients with carotid stenosis. Specifically, we quantified pressure and flow waveforms, the hemodynamic impact of the carotid stenoses, and the resistances of the distal cerebral vascular territories.

Fig. 4.2 shows pressure and flow waveforms in six arteries of the neck and head for patient 1. The mean pressure gradient over the stenosis was defined as $\Delta\bar{P} = \bar{P}_{prox} - \bar{P}_{dist}$, where $\bar{P}_{prox}$ and $\bar{P}_{dist}$ are the mean cross-sectional-averaged pressures 2 cm proximal and distal to the maximum diameter reduction, respectively. The mean pressure gradient over the RICA was $\Delta\bar{P}_{RICA} = 26.25$ mmHg, compared to a $\Delta\bar{P}_{RICA} = 0.58$ mmHg mean pressure gradient over the unstenosed

LICA. Another metric of the hemodynamic significance of the stenosis is given by the fractional flow (FF) index [68][41][96], defined as $FF = \bar{P}_{dist}/\bar{P}_{prox}$. This index produced $FF_{RICA} = 0.71$ and $FF_{LICA} = 0.99$. The stenosis resulted in a substantial difference in flow between the RICA and LICA, with mean flow rates of $\bar{Q}_{RICA} = 3.25\ mL/s$ and $\bar{Q}_{LICA} = 6.79\ mL/s$. In the CoW, the RMCA and LMCA exhibit substantially different mean values of pressure ($\bar{P}_{RMCA} = 47.62$ mmHg, $\bar{P}_{LMCA} = 74.91$ mmHg, mean difference: 27.29 mmHg). Despite the pressure difference between hemispheres, the mean flow rates in the RMCA and LMCA were comparable with $\bar{Q}_{RMCA} = 3.74\ mL/s$ and $\bar{Q}_{LMCA} = 3.92\ mL/s$. This preservation of flow at the RMCA was achieved through a reduction in the total resistance of its distal vasculature, resulting in $R_{RMCA} = 1.7 \cdot 10^9\ Pa\ s\ m^{-3}$ compared to $R_{LMCA} = 2.54 \cdot 10^9\ Pa\ s\ m^{-3}$ at the contralateral LMCA.

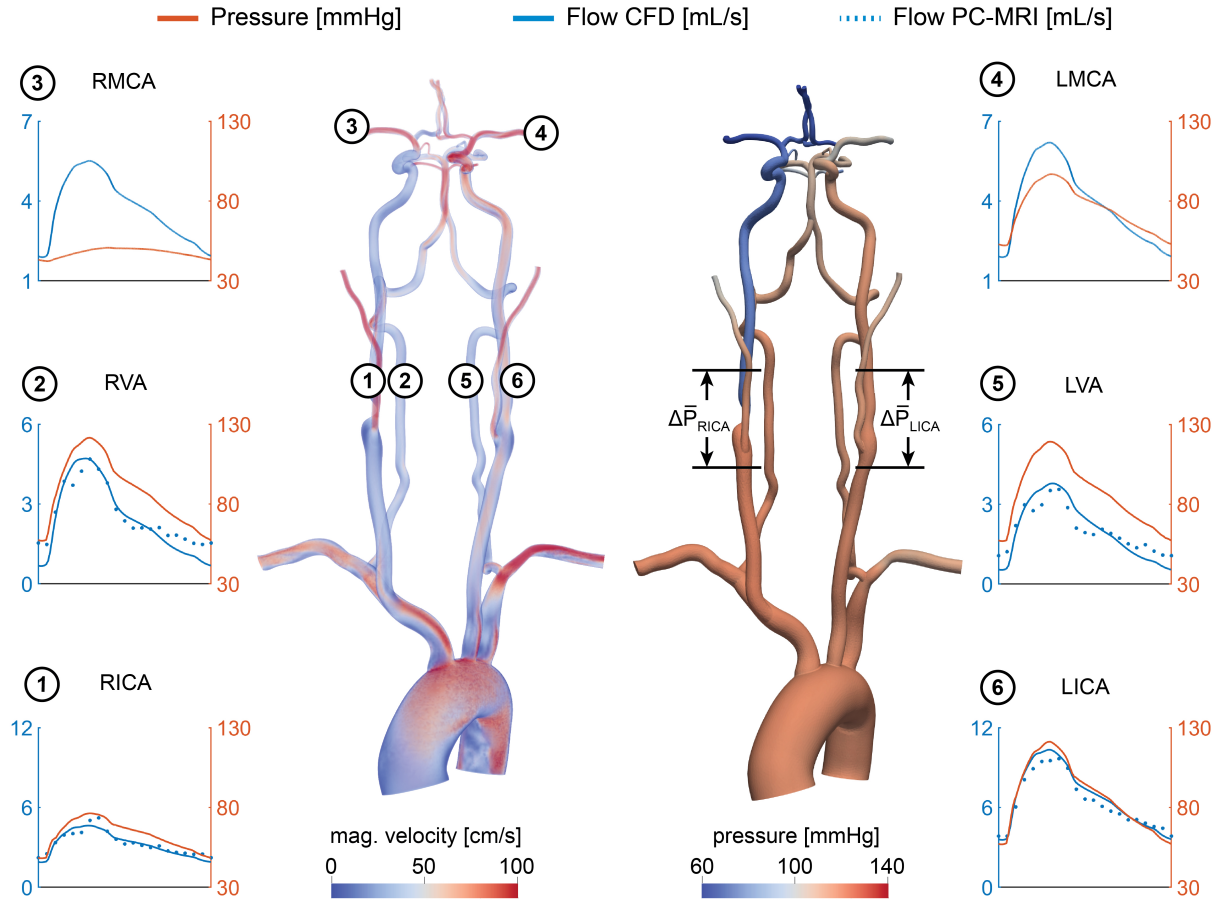

Fig. 4.2 Velocity and pressure fields at peak systole for patient 1. Flow and pressure waveforms are evaluated in the internal carotid (ICA), vertebral (VA), and middle cerebral arteries (MCA). The flow waveforms in the neck arteries are compared to PC-MRI measurements above the carotid bifurcation (dotted lines). The mean pressure gradient $\Delta\bar{P} = \bar{P}_{prox} - \bar{P}_{dist}$ was calculated over the RICA stenosis and the same vessel segment in the LICA.

Fig. 4.3 shows the pressure and flow waveforms for patient 2. The mean pressure gradient over the stenoses and *FF* indices in the RICA and LICA were $\Delta\bar{P}_{RICA} = 1.75$ mmHg, $\Delta\bar{P}_{LICA} = 0.71$ mmHg, $FF_{RICA} = 0.98$, and $FF_{LICA} = 0.99$, respectively. The mean flow rates in the RICA and LICA were $\bar{Q}_{RICA} = 4.00\ mL/s$ and $\bar{Q}_{LICA} = 5.25\ mL/s$. Despite the severe RICA stenosis and moderate LICA stenosis, the mean pressure at the RMCA and LMCA were similar ($\bar{P}_{RMCA} = 106.42$ mmHg, $\bar{P}_{LMCA} = 106.37$ mmHg, mean difference: 0.05 mmHg). The mean flow rates, as well as the corresponding total resistances, at the outlets of the RMCA and LMCA were comparable with $\bar{Q}_{RMCA} = 2.50\ mL/s$ and $\bar{Q}_{LMCA} = 2.60\ mL/s$, and $R_{RMCA} = 5.64 \cdot 10^9\ Pa\ s\ m^{-3}$ and $R_{LMCA} = 5.44 \cdot 10^9\ Pa\ s\ m^{-3}$, respectively.

For comparison, the pressure and flow results for the healthy control subject from chapter 1 are shown in Fig. 4.4. A pressure gradient and fractional flow over the patent right and left carotid bifurcations were calculated analog to the patient examples for reference, yielding $\Delta\bar{P}_{RICA} = 0.77$ mmHg and $\Delta\bar{P}_{LICA} = 0.55$ mmHg and correspondingly $FF_{RICA} = 0.99$ and $FF_{LICA} = 0.99$. The flow rates in the RMCA and LMCA were similar with $\bar{Q}_{RMCA} = 3.71\ mL/s$ and $\bar{Q}_{LMCA} = 3.62\ mL/s$ and the pressure difference between these outlets was $\Delta\bar{P}_{MCA} = 3.61$ mmHg.

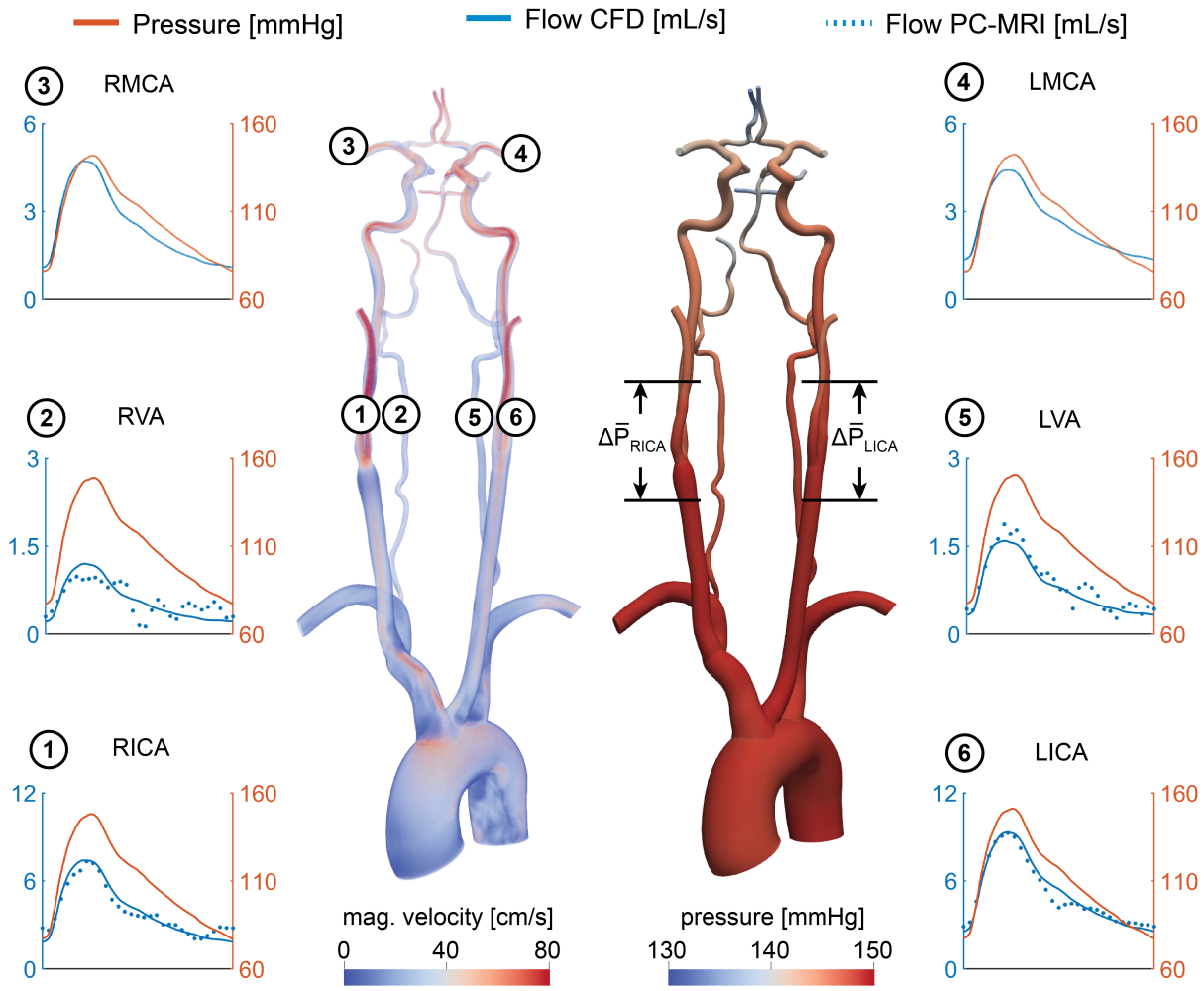

Fig. 4.3 Velocity and pressure fields at peak systole for patient 2. Flow and pressure waveforms are evaluated in the internal carotid (ICA), vertebral (VA), and middle cerebral arteries (MCA). The flow waveforms in the neck arteries are compared to PC-MRI measurements above the carotid bifurcation (dotted lines). The mean pressure gradient $\Delta\bar{P} = \bar{P}_{prox} - \bar{P}_{dist}$ was calculated over the RICA and LICA stenosis.

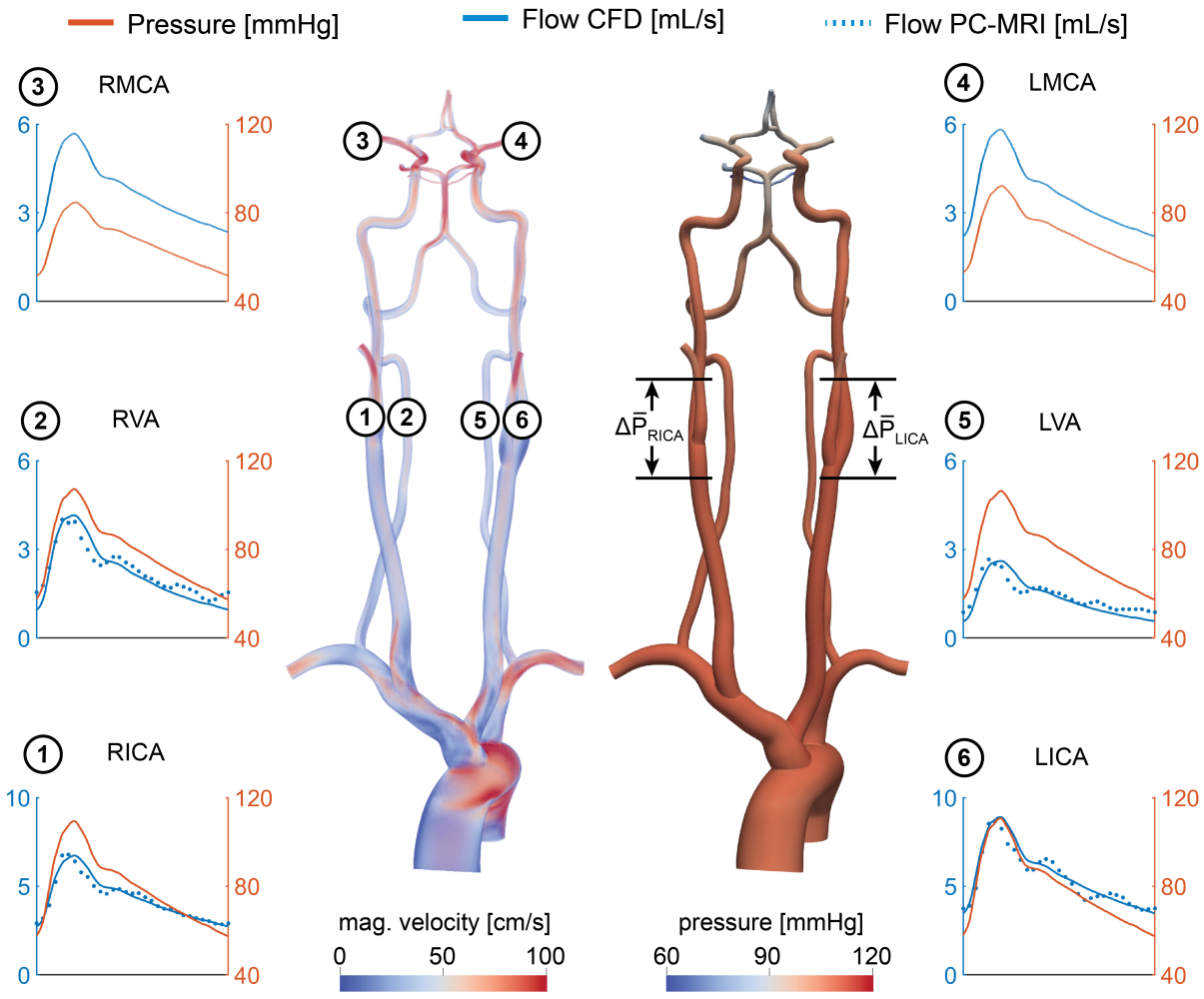

Fig. 4.4 Velocity and pressure fields at peak systole are shown for the healthy control subject. Flow and pressure waveforms are evaluated in the internal carotid (ICA), vertebral (VA), and middle cerebral arteries (MCA) and compared to PC-MRI measurements in the neck arteries. The mean pressure gradient $\Delta\bar{P} = \bar{P}_{prox} - \bar{P}_{dist}$ was calculated over the RICA and LICA bifurcation.

A Comparison of the flow waveforms in the main cervical arteries (above the carotid bifurcation) obtained from CFD with in-vivo PC-MRI data showed an overall good agreement in both patients and the healthy control subject and resulted in differences in mean flow rates of less than 10%.

The blood supply from the main cervical arteries to the CoW, obtained with LPT, is illustrated in Fig. 4.5. Patient 1 exhibited a large amount of flow compensation between hemispheres with the RACA (#2) being predominately supplied by the LICA (80.31%) via the anterior communicating artery. In contrast, patient 2 revealed only a small amount of collateral flow from the LICA to the RACA (20.05%). The MCAs (#3, #4) were predominately supplied by the ipsilateral ICA in both patients. Significant differences in the supply of the posterior territory were observed between patients. Patient 1 revealed a swirling motion of vertebral flow in the basilar artery, resulting in dominant supply of the LPCA (#5) from the RVA and dominant supply of the RPCA (#6) from the LVA. The posterior territory of patient 2 was supplied ipsilaterally by the ICAs and the cerebellum was supplied by the LVA. The CFD-derived blood supply of the main intracranial arteries matched well the territorial perfusion obtained from vessel-selective ASL.

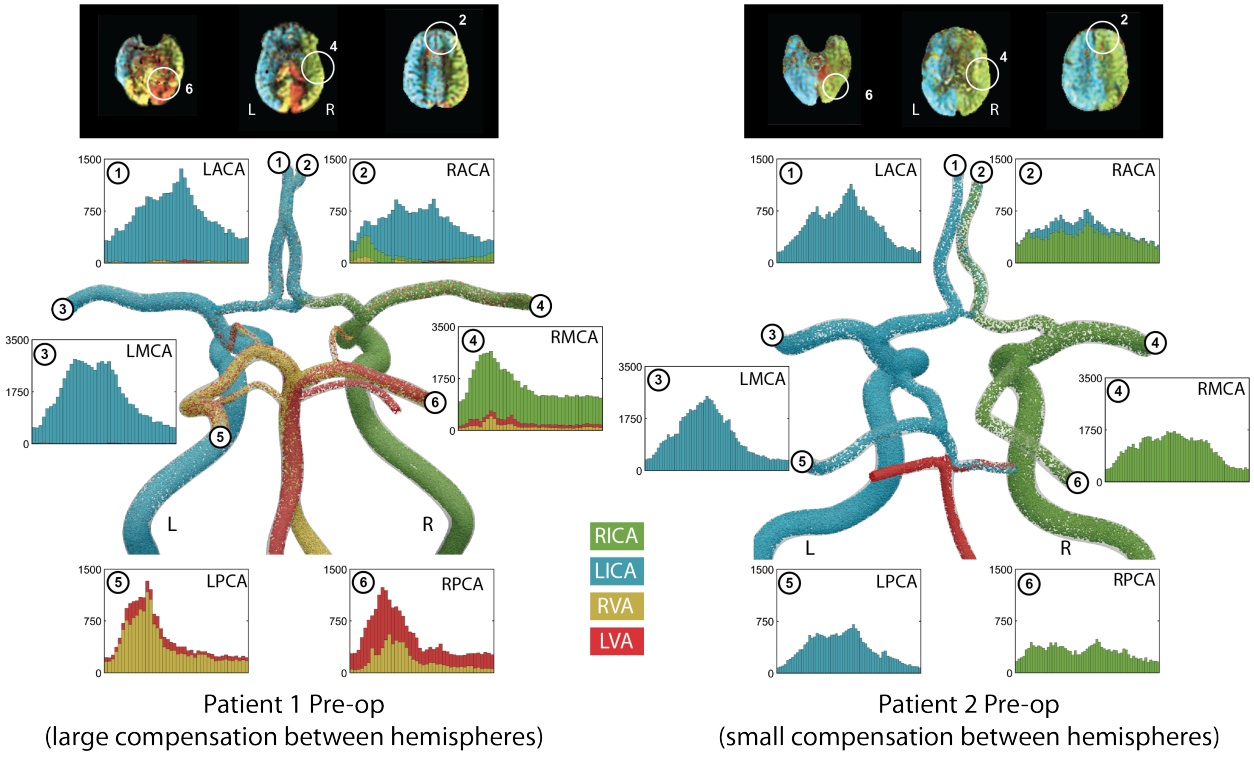

Fig. 4.5 Analysis of blood supply in the CoW with Lagrangian particle tracking. Particles are color-coded based on the originating cervical artery. Histograms show the particle count over a full cardiac cycle at each outlet. The results of Lagrangian particle tracking are compared to territorial perfusion maps from vessel-selective ASL.

4.3.3 Postoperative hemodynamic analysis

Changes in blood supply following revascularization in patient 2 are illustrated in Fig. 4.6. The preoperative collateral flow from the LICA to the RACA disappeared postoperatively. The direction of Flow in the anterior communicating artery was reversed, resulting a minor flow contribution from the RICA to the LACA (7.24%).

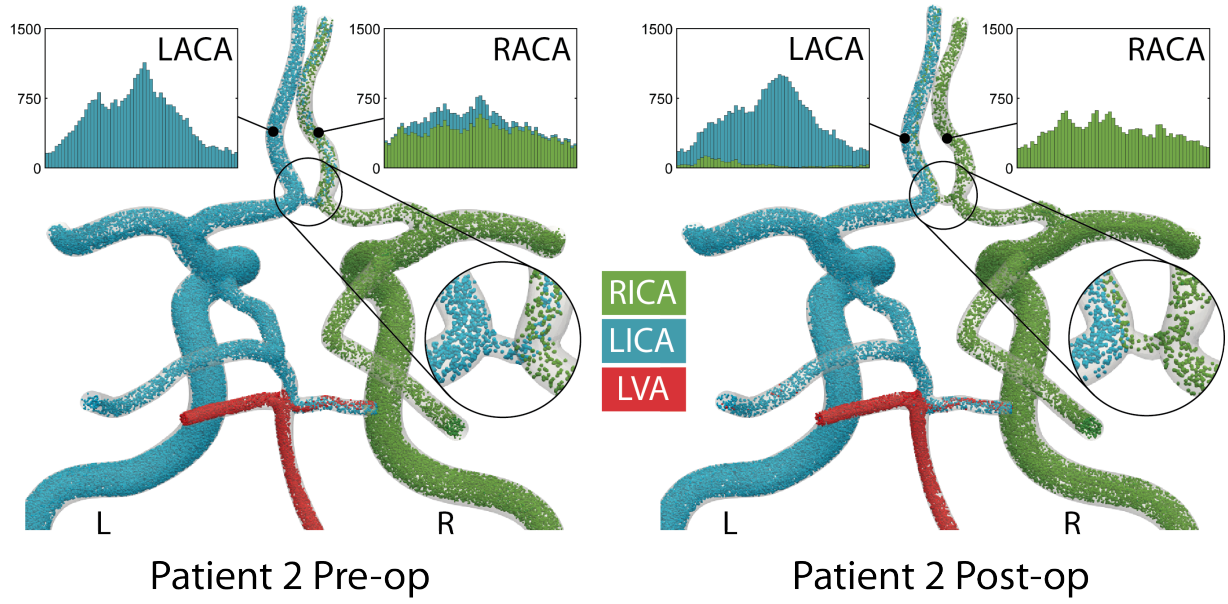

Fig. 4.6 Comparison of the preoperative and postoperative blood supply in the CoW with Lagrangian particle tracking. Particles are color-coded based on the originating cervical artery. Histograms show the particle count over a full cardiac cycle at the right and left ACA. A close-up of the flow in the anterior communication artery is shown.

To further assess the hemodynamic changes following revascularization, the mean pressure gradient and fractional flow FF were calculated over the stenosis (Fig. 4.7). Patient 2 exhibited a preoperative mean pressure gradient of $\Delta\bar{P}_{RICA,pre} = 1.8\ mmHg$ over the severely stenosed RICA and $\Delta\bar{P}_{LICA,pre} = 0.7\ mmHg$ over the mildly stenosed LICA. Following revascularization, the mean pressure gradient in the RICA was reduced to $\Delta\bar{P}_{RICA,Post} = 0.1\ mmHg$. The mean pressure gradient over the LICA did not change postoperatively. However, contrasting these values to the preoperative mean pressure gradient in the RICA of patient 1 of $\Delta\bar{P}_{RICA} = 26.3\ mmHg$, the pressure gradient of the RICA in patient 2 was neglectable. The minor impact of the procedure on the pressure gradient was further demonstrated by the fractional flow changing from $FF_{RICA,pre} = 0.98$ preoperatively to $FF_{RICA,post} = 0.99$ postoperatively.

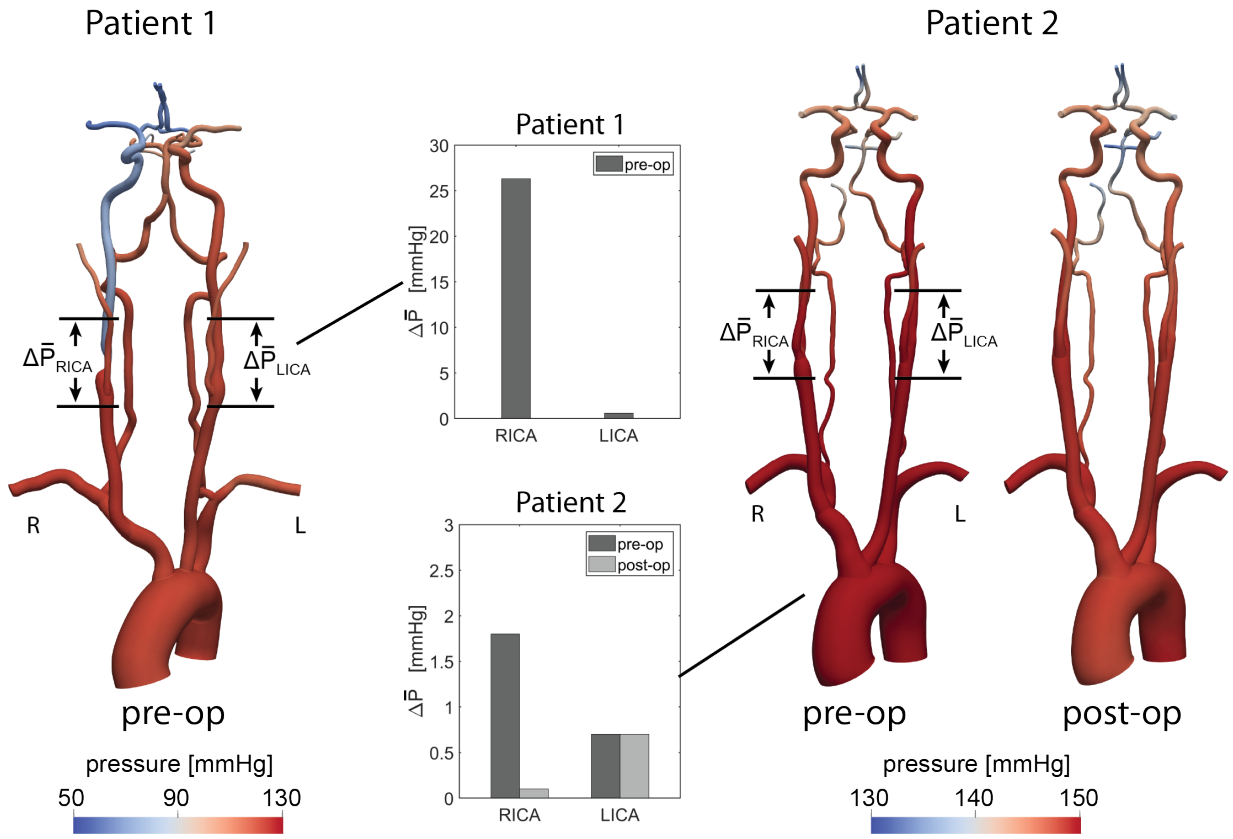

Fig. 4.7 Evaluation of the mean pressure gradient over the stenosis in patients 1 and 2. The pressure distribution in the vasculature is shown at peak systole for both patients. The mean pressure gradient was calculated as the difference between the mean pressures 2cm proximal and distal to the peak stenosis.

The changes in mean flow rates in the cervical and cerebral arteries following revascularization of patient 2 are summarized in Fig. 4.8. Flow in the RICA and LMCA increased postoperatively, but changes in the flow distribution among the main arteries were overall small.

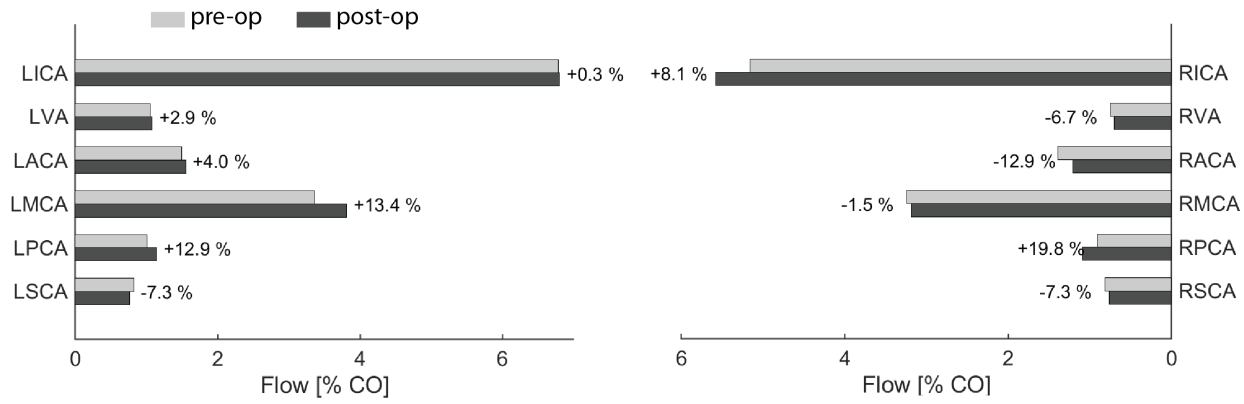

Fig. 4.8 Comparison of preoperative and postoperative mean flow rates in the main arteries. Mean flow rates were normalized with the cardiac output (CO).

4.4 Discussion

4.4.1 Clinical assessment of patients with carotid stenosis

The current paradigm of diagnosing and stratifying patients with carotid stenosis is centered around assessing the degree of stenosis. While a reduced long-term stroke risk following carotid revascularization has been demonstrated in symptomatic patients with stenotic lesions of >50% [3][4][5], the long-term benefits of revascularization in asymptomatic patients are an ongoing topic of debate. Based on current guidelines, asymptomatic patients with stenotic lesions of > 60 % should be considered for revascularization [97]. However, these guidelines were derived from clinical trials dating back two decades [98][99]. Significant advancements have been made since in the areas of medical therapy and carotid revascularization, prompting new clinical trials to re-evaluate the benefits of revascularization in asymptomatic patients (CREST-2, ACST-2). However, the question of how to best identify patients who benefit from revascularization remains.

Over the past decade, there has been a shift towards a hemodynamic-driven assessment of stenotic lesions in coronary artery disease. Intervention guided by fractional flow reserve (FFR) has been shown superior to anatomic-based intervention by reducing myocardial ischemia, rate of death, and revascularization [100][101]. While a similar strategy has been proposed for carotid stenosis [68], studies so far have only established feasibility [96][42]. Furthermore, there are significant differences between the cerebral and coronary vasculatures, including the presence collateral flow compensation and the pathology of ischemia and infarction. To further explore the role of hemodynamics in cerebrovascular occlusive disease and the risk of stroke, a better understanding of the complex flow phenomena in the cerebral vasculature is needed.

4.4.2 Computational modeling

Image-based computational modeling for characterizing complex hemodynamics has found increasing use in the cardiovascular field due to its ability to provide velocity and pressure data with a high spatial and temporal resolution. The capabilities of image-based CFD analysis to assess cerebral hemodynamics have previously been demonstrated for intracranial stenosis [41][42] and aneurysm [43][44][45]. However, previous CFD studies of cerebral hemodynamic have generally relied on modeling assumption about the flow distribution in the CoW, either based on literature flow data or allometric scaling laws, which severely limit patient-specific applications. To overcome these shortcomings and produce patient-specific models of cerebral blood flow, we previously presented a CFD calibration strategy based on perfusion data from ASL data [95]. In this work, we demonstrated the advantages of our calibrated CFD analysis to characterize cerebral hemodynamics in two patients with carotid stenosis.

4.4.2.1 Pre-operative CFD analysis

Using the calibrated and validated CFD model, we performed an in-depth quantification of preoperative hemodynamics in the two patients with carotid stenosis. Both patients presented with a severe RICA stenosis (70-99% diameter reduction) according to the velocity criteria (Patient 1), which correlates the peak systolic velocity measured with Duplex Ultrasound to a percentage diameter reduction, and the ECST criteria (Patient 2), which is defined as the diameter reduction relative to the original vessel diameter based on CTA. Despite similar degrees of clinical stenosis severity, the cerebral hemodynamics varied significantly between these two patients. In patient 1, the RICA stenosis led to severe ipsilateral pressure gradient and flow reduction compared to the contralateral unstenosed LICA. Despite the pressure difference between right and left hemisphere, there was no significant difference in flow between the right and left MCA due to collateral flow compensation and vasodilation of the distal vasculature. In contrast, the RICA stenosis in patient 2 did not result in a notable ipsilateral pressure gradient or flow reduction. Consequently, the flow compensation between hemispheres was small. The difference in flow compensation between the two patients is explained by the much smaller stenosis diameter of patient 1 (1.4 mm in our geometric model, 74.7% diameter reduction relative to the distal diameter) compared to patient 2 (3.0 mm, 52.3% diameter reduction relative to distal diameter), see Fig. 4.1. Flow compensation is highly dependent on accurate characterizations of the degree of stenosis, the cerebral anatomy, and the cerebrovascular reserve and can vary significantly between patients.

Medical imaging used for cerebral hemodynamics assessment (e.g. Transcranial Doppler, 4D Flow MRI, etc.) only provide information on velocity. However, the above results (similar cerebral flow between the two subjects while having substantial differences in pressure) highlight the shortcomings of describing the hemodynamic significance of stenotic lesions purely from the perspective of velocity. In contrast, blood pressure is highly sensitive to changes in vascular resistance induced by the stenosis, as illustrated in patient 1. Therefore, substantial changes in cerebral blood pressure may be a more sensitive marker for diminished vascular flow reserve. While pressure catheter measurements are commonly acquired in other vascular territories (e.g. coronary arteries), cerebral blood pressure is generally not acquired during clinical assessment of patients with carotid stenosis due to increased stroke risk. While there have been efforts to derive pressure gradients from 4D Flow MRI data, application in the small and tortuous CoW arteries remains challenging due to limited spatial resolution [17]. In contrast, patient-specific CFD overcomes these shortcomings by providing highly resolved velocity and pressure.

To quantify the stenosis hemodynamic significance, we calculated the fractional flow index, defined as the ratio of the pressures distal and proximal to the stenosis under baseline flow conditions (e.g., non-hyperemic). The fractional flow in the RICA stenosis was $FF_{RICA} = 0.71$ for patient 1 and $FF_{RICA} = 0.98$ for patient 2. Using a threshold of $FF = 0.8$ [96], only the RICA stenosis in patient 1 would be deemed to be hemodynamically significant. While the clinical metric of diameter reduction resulted in a similar value of 70-99% in the RICA for both patients, the fractional flow index captured better the large differences in cerebral hemodynamics between the patients.

4.4.2.2 Post-operative CFD analysis

The postoperative analysis of patient 2 revealed overall minor hemodynamic changes following carotid endarterectomy. While a small reduction in pressure gradient and increase in flow in the RICA was observed, the hemodynamic impact of stenosis was preoperatively small and did therefore not substantially change following revascularization.

Since the procedure did not improve hemodynamics, was did the patient still receive a benefit? One could argue that the primary purpose of revascularization is to restore blood flow and pressure in the cerebral vasculature. However, it is important to point out that only a small fraction of all ischemic strokes is caused directly by the reduction in flow due to the stenosis. The majority of

ischemic strokes are caused by embolic events, either from plaque rapture or thrombus formation around the stenosis. By removing the plaque during carotid endarterectomy, the risk of embolic stroke can be reduced. However, not every plaque is at risk for rupture. Unfortunately, evaluating plaque vulnerability is challenging and a focus of current research.

Interestingly, hemodynamics also seem to play a significant role in the rapture vulnerability of atherosclerotic plaque [102]. While wall shear stress is known to be a key player in the formation and progression of carotid plaque, tensile stress seems to be relevant in the risk of plaque rapture [103]. CFD analyses of tensile stress in carotid bifurcations have shown that the pressure gradient over the stenosis is correlated with the tensile stress induced at the site of the thinnest fibrous cap [102]. Unfortunately, the relationship between hemodynamics and risk of embolic stroke is still mostly unknown and requires further investigation.

4.4.3 Future clinical applications

The blood supply to the main territories of the CoW, obtained from CFD and LPT, provided important information about collateral flow in the anterior circulation and mixed VA supply in the posterior circulation. Beyond flow compensation, the blood supply to the cerebral vascular territories can provide clinically relevant information about the etiology of embolic stroke. Even after thorough diagnostic evaluation, the cause of embolic stroke remains uncertain in one third of cases [104]. It is common that multiple atherosclerotic lesions within the same patient are identified. Evaluation of the blood supply in the region of the stroke could help to determine the source of emboli and ultimately guide clinical treatment.

4.4.4 Limitations

This study was limited by the small sample size. While the results were validated against in-vivo data, performing the same CFD analysis in different patients with carotid stenosis might result in different outcomes. This initial work is therefore intended as a feasibility study to demonstrate the capabilities of a patient-specific CFD analysis to characterize cerebral hemodynamics and extract clinically meaningful data.

The CFD models of cerebral blood flow presented in this work did not take into account any secondary collateral pathways including ophthalmic and leptomeningeal vessels. The anatomical data of the two patients was carefully studied and did not show any visible secondary collaterals.

However, it is worth noting that secondary collaterals could be integrated into the geometric models if they are detectable on the imaging data.

4.5 Conclusions

In this work, we presented a patient-specific CFD modeling strategy to characterize cerebral hemodynamics in patients with carotid stenosis. We demonstrated that our CFD analysis can provide detailed and quantitative information about hemodynamic impact of carotid stenosis and collateral flow compensation in the circle of Willis. Analysis of two patients with similar clinical classifications of RICA stenosis severity showed significant differences in cerebral hemodynamics and flow compensation which was not apparent from anatomical data alone. Comparison of preoperative and postoperative hemodynamics in one patient example resulted in only minor changes following revascularization despite severe carotid stenosis. We further illustrated the advantages of CFD-based pressure data for assessing the hemodynamic significance of carotid stenosis. Future studies are needed to investigate the benefits of using of a hemodynamic-based metric (fractional flow) versus an anatomy-based metric (diameter reduction) for the risk assessment of CVOD patients.

Chapter 5: Comparison of Outflow Boundary Condition Calibration Strategies: ASL-Based vs. Allometric-Based

5.1 Introduction

The cerebral vasculature consists of a complex network of arteries supplying all regions of the brain with blood. To ensure optimal blood supply, the cerebral vasculature is equipped with a set of collateral pathways forming the circle of Willis (CoW), which allows for flow compensation between hemispheres. Cerebral autoregulation of the distal vascular bed further helps to maintain adequate blood flow to the brain. The compensatory capabilities are however highly subject-specific due to the anatomical variability of the cerebral vasculature. A complete CoW anatomy is only present in approximately 50% of the population [1]. These flow compensating capabilities become most relevant in the presence of cerebrovascular occlusive disease, where plaque buildup inside the lumen, or stenosis, of the main brain supplying arteries can result in significant flow reductions.

Quantitative information on cerebral blood flow obtained from conventional imaging modalities are generally limited to either peak velocity measurements at selected locations (Transcranial Doppler Ultrasound) or a low-resolution velocity field (4D Flow MRI). Image-based computational fluid dynamics (CFD) has become an increasingly popular method of non-invasively quantifying complex cerebral hemodynamics due to its high spatial and temporal resolution. Previous CFD modeling studies of cerebral flow in the CoW have investigated the impact of anatomical variations on collateral flow compensation in the absence of stenosis [105][106] and in the presence of stenosis [107][108].

One of the main challenges of modeling cerebral hemodynamics using CFD is to define physiologically meaningful boundary conditions at the outlets of the CoW that represent the subject's true hemodynamics. Due to the general absence of in-vivo flow and pressure data in the intracranial arteries, previous studies have relied heavily on modeling assumptions about the flow distribution in the CoW. One commonly used modeling approach is allometric-scaling, where total

arterial resistance assigned to the intracranial arteries is distributed across the CoW outlets proportional to the outlet's cross-sectional area [77][75]. Alternatively, population-averaged intracranial flow rates obtained from PC-MRI studies in healthy subjects have been used to assign outflow boundary conditions [76]. While these modeling assumptions might lead to reasonable results in healthy subjects, in situations of cerebrovascular disease, the distribution of flow between the different vessels of the CoW may be substantially different from that given by idealized allometric scaling principles or literature data. To avoid modeling assumptions, previous studies have also used 4D flow MRI data to directly assign flow rates at the CoW outlets [109][110]. However, due to the limited spatial resolution of clinically available 4D flow (typically 1 mm^3), accurate measurements of flow in the cerebral arteries (approx. 2-3mm in diameter) is challenging.

To overcome these limitations, we recently presented a strategy to calibrate outflow boundary conditions in the CoW using brain perfusion data obtained from arterial spin labeling (ASL) MRI, in combination with PC-MRI data [95]. This patient-specific approach measures the blood supply to the main cerebral vascular territories and accounts for changes in the distal vascular bed.

In generally, there has not been consensus in the literature on how to best specify boundary conditions in the CoW to produce patient-specific CFD results. It appears that in most cases the choice of boundary condition specification is primarily guided by the availability or unavailability of clinical data. Furthermore, the impact of modeling assumptions on cerebral hemodynamics is not well studied, particularly in subjects with flow-altering disease or anatomical variations.

The goal of this work is to investigate the impact of outflow boundary conditions on cerebral hemodynamics in subjects with carotid stenosis. We are comparing the performance of two outflow boundary conditions calibration strategies, an ASL-based and allometric-based, to model patient-specific cerebral hemodynamics. The blood supply to the main arteries of the CoW is evaluated using Lagrangian particle tracking and the fractional flow distribution is validated against vessel-selective ASL data.

5.2 Methods

5.2.1 Computational modeling of cerebral hemodynamics

Cerebral hemodynamics were assessed in three subjects with varying degrees of carotid stenosis: Subject 1) healthy volunteer without evidence of stenosis, but with an incomplete CoW (both posterior communicating arteries were missing); Subject 2) patient with bilateral carotid stenosis, 80-90% (3.0 mm remaining luminal diameter) in the right and 60% (5.4 mm remaining luminal diameter) in the left proximal internal carotid artery (ICA). The patient's CoW was Incomplete (right posterior communicating artery missing) and the right vertebral artery (VA) was atretic; Subject 3) patient with a 70-99% stenosis in the right ICA (1.4 mm remaining luminal diameter) and a complete CoW. The protocol was approved by the local Institutional Review Board and all subjects provided informed written consent (HUM00114275 and HUM00018426).

Information on anatomy, flow, and perfusion was acquired with MRI at 3T (MR750; GE Healthcare, Waukesha, WI). Anatomical data of the vasculature from the aorta to the CoW was collected with a combination of 2D T1-weighted spoiled gradient echo and 3D Time-of-Flight. Flow rates were measured at the ascending aorta and the main neck arteries above the carotid bifurcation using 2D cardiac-gated phase-contrast (PC) MRI. Information on brain tissue perfusion was acquired with ASL. First, a standard non-selective labeling scheme was performed to measure the total perfusion in the brain tissue [50]. Second, a vessel-selective labeling scheme was performed to measure the perfusion territories of the main neck arteries (carotid and vertebral arteries) [32][73]. Following the MRI protocol, non-invasive cuff pressure measurements of the right upper extremity were acquired while the subject remained in the supine position. A more detailed description of the imaging protocol can be found in chapter 3.2.2.

3D geometric models of the vasculature from the aorta to the CoW were reconstructed from the anatomical imaging data using the validated open-source computational hemodynamics framework CRIMSON [78]. The model reconstruction consisted of the following steps: 1) Defining the centerlines of each vessel, 2) 2D segmentation of vessel contours perpendicular to the centerlines, 3) Lofting of the vessel contours to create an analytical representation of each vessel, 4) Blending of vessels to create a 3D model of the vasculature. The final 3D geometric models are shown in Fig. 5.1. The geometric models were then discretized using linear tetrahedral elements. The mesh was optimized based on the local velocity-gradients using a mesh-adaptation

algorithm [79]. The final meshes for subjects 1-3 consisted of 2.16x10^6, 2.39x10^6, and 1.84x10^6 elements, respectively, with a minimum and maximum element length of 0.1 mm and 1.0 mm. Mesh-independence was demonstrated for subject 3 by creating an additional highly refined mesh with 6.86x10^6 elements. The increase in mesh elements resulted in a difference in mean flow rates of less than 1% and a maximum difference in peak stenosis velocity of 2%.

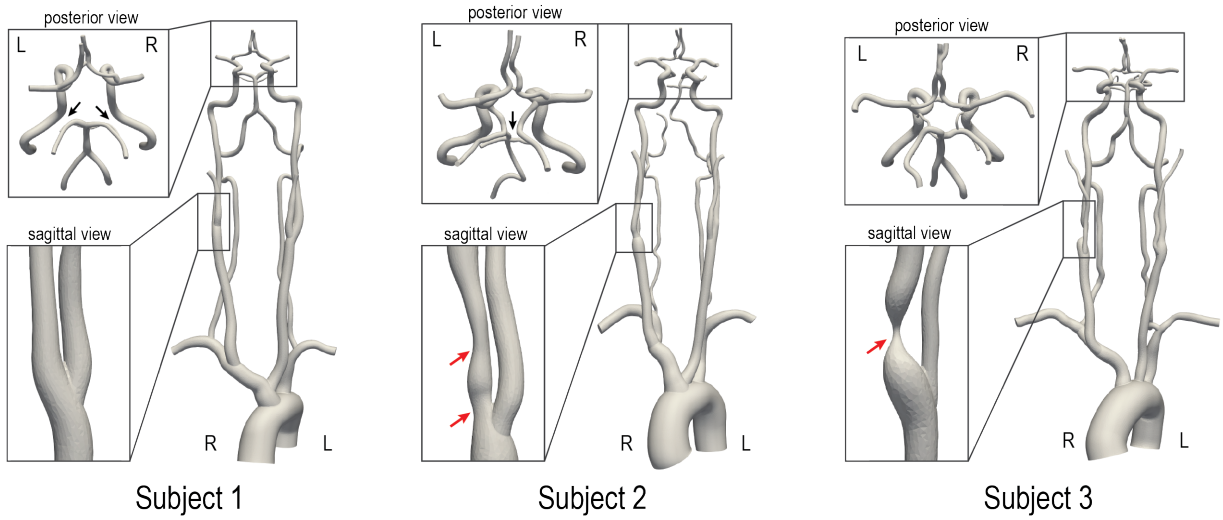

Fig. 5.1 3D geometric models of all 3 subjects. Close-ups show a sagittal view of the right carotid bifurcation and a posterior view of the CoW. Red arrows indicate the location of stenosis. Black arrows indicate missing segments in the CoW anatomy.

At the inlet of the ascending aorta, a parabolic velocity profile was prescribed based on the pulsatile PC-MRI data. At each model outlet, a 3-elements Windkessel parameter model was prescribed to represent the distal vascular bed. The 3-element Windkessel model consists of a proximal resistance (R_p), a distal resistance (R_d), and a capacitor (C) [80]. A non-slip boundary condition was assigned to all vessel walls.

Blood was modeled as an incompressible Newtonian fluid with a dynamic viscosity of 0.004 kg·m^{-1}·s^{-1} and a density of 1,060 kg·m^{-3}. A stabilized finite-element formulation for the incompressible Navier-Stokes equations was employed to solve for blood flow velocity and pressure in the discretized model domain [82]. Computations were performed using 80 cores on a high-performance computing cluster. Simulations were run using a time step size of 0.1 ms until cycle-to-cycle periodicity was achieved, typically after 5 cardiac cycles.

5.2.2 Outflow boundary condition calibration

Initial estimates for the Windkessel model parameters were obtained by first calculating a total arterial resistance as $R_T = P_{mean}/Q_T$, where Q_T is the total mean inflow at the ascending aorta and $P_{mean} = 1/3\, P_{systolic} + 2/3\, P_{diastolic}$ is the mean pressure. Similar, a total arterial compliance was calculated as $C_T = \left(Q_{T,max} - Q_{T,min}\right)/\left(P_{systolic} - P_{diastolic}\right) * \Delta t$, where $Q_{T,max}$ and $Q_{T,min}$ are the maximum and minimum of the inflow waveform at the ascending aorta and Δt is the time difference between these values. Following, R_T and C_T were distributed among the different outlets, to obtain $R_i = R_{p,i} + R_{d,i}$ and C_i for vessel $i = 1, \dots, 13$, as described in [81]. The proximal resistance $R_{p,i}$ was initially set to 5% of the total outlet resistance R_i for the descending aorta and the subclavian arteries and to 8% for all remaining outlets. Two calibration strategies, an ASL-based and allometric-based, were employed to specify the 3-element Windkessel parameters at the outlets. The details are described in the following sections.

5.2.2.1 ASL-based calibration

In this strategy, the flow distribution across the main intracranial arteries in the CoW was estimated based on non-selective ASL perfusion images in combination with PC-MRI data and a vascular territory atlas. A detailed description can be found in chapter 3.2.4. Briefly, the perfusion images were segmented into the vascular territories corresponding the main intracranial arteries of the CoW using a vascular territory atlas. A perfusion split across territories was then calculated based on the integrated perfusion signal in each territory. Finally, a mean target flow was calculated for each outlet by scaling the total inflow to the CoW, obtained from PC-MRI, with the perfusion split.

The mean flow rate in the subclavian arteries was assumed to be 5.6% of the total inflow at the ascending aorta [75]. In the external carotid arteries, the mean flow rate was directly derived from PC-MRI data. To maintain mass-conservation, the mean flow rate at the descending aorta was prescribed as the difference between the total inflow at the ascending aorta and the outflow of all extracranial and intracranial artery outlets.

To match the calculated mean target flow rates in the CFD model, the distal resistance $R_{d,i}$ at each vessel outlet *i* was dynamically tuned during simulation runtime using controller scripts [84]. At each time step, the difference between the mean target flow rate and the current mean CFD flow rate (averaged over the last cardiac cycle) was calculate for each outlet i and $R_{d,i}$ was

proportionally adjusted (Fig. 5.2). Once all mean CFD flow rates were converged towards the mean target flow rate (< 1%), the simulation was terminated.

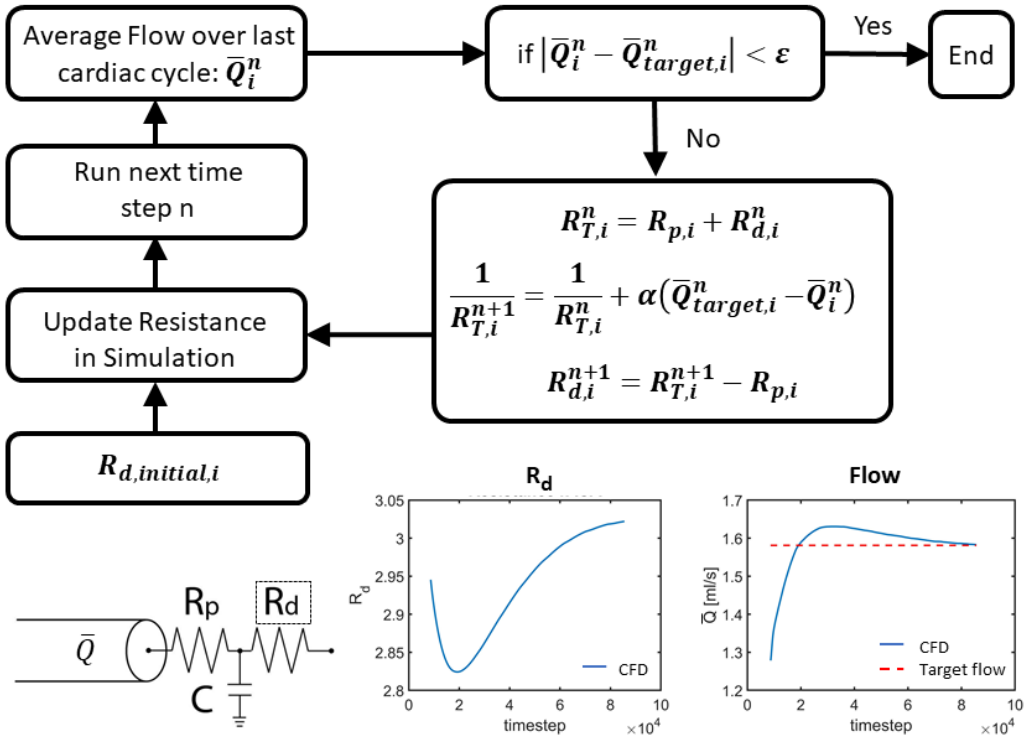

Fig. 5.2 Flow chart describing the controller script to adjust distal resistance $R_{d,i}$ at each outlet during simulation runtime. $R_{d,i}$ was iteratively changed each time step *n* proportionally to the difference in calculated mean target flow rate and the current mean CFD flow rate. An example of the convergence of the mean flow rate (blue line) towards the mean target flow rate (red dashed line) over the simulation time steps and the corresponding change in distal resistance is shown for the RACA.

Next, the ratio of R_p/R_d of the Windkessel models in the CoW were further adjusted to match the pulsatility of the CFD flow waveforms in the main cervical arteries to the flow waveforms obtained from PC-MRI above the carotid bifurcation. The total resistance R_i at each outlet was kept constant to maintain the previously match mean target flow rates. Finally, the cuff pressure measurements $P_{systolic}$ and $P_{diastolic}$ at the right subclavian artery were matched in the CFD model by adjusting the total arterial resistance R_T and the total arterial compliance C_T. The changes in R_T and C_T were distributed among the outlets proportional to R_i and C_i.

5.2.2.2 Allometric-based calibration

In this calibration strategy, we assumed that no prior information about the flow split in the CoW was available. This represents a typical clinical scenario, where intracranial flow data is unavailable. However, the flow data in the extracranial arteries from PC-MRI and the cuff pressure data was still included in this approach.

The total arterial resistance R_T was first distributed among the main territories including the descending aorta, subclavian arteries, external arteries, and CoW based on the previously calculated mean flow rates from PC-MRI. The total resistance allocated to the CoW was then distributed among the main intracranial arteries proportional to the cross-sectional diameters of each outlet and kept constant. As with the ASL-based calibration, the mean target flow rates of the extracranial outlets were matched in the CFD model using the controller scripts. Following, the pulsatility of the PC-MRI waveforms and the cuff measurements were matched in the CFD model as described in section 5.2.2.1.

5.2.3 Fractional blood supply

The blood supply to the main intracranial arteries was visualized and quantified using Lagrangian particle tracking (LPT). LPT was performed for each neck artery individually by seeding mass-less particles continuously at the base of the artery and transporting the particles based on the velocity field obtained from the calibrated CFD model over multiple cardiac cycles. Once cycle-to-cycle periodicity was achieved in the CoW, particles were counted at each outlet over a full cardiac cycle. To quantify the blood supply at each intracranial artery, a fractional blood supply (FBS) was calculated. FBS was defined as the ratio of counted particles from each neck artery to the total number of particles from all neck arteries combined. The FBS based on LPT was then validated against the FBS measured with vessel-selective ASL. In vessel-selective ASL, blood in each neck artery was magnetically labeled (analog to the seeding of particles in LPT) and the labeled blood was measured in the brain tissue. The post-processing steps to extract the FBS from the vessel-selective ASL images are described in chapter 3.2.5.1.

5.3 Results

5.3.1 Flow comparison in neck arteries

Comparison of the mean flow rates in the main neck arteries above the carotid bifurcation revealed a good match between the PC-MRI data and the ASL-calibrated CFD with maximum errors across the neck arteries of 6.85%, 8.99%, and 5.75% in subjects 1-3, respectively (Fig. 5.3. The allometric-based CFD analysis resulted in larger discrepancies compared to the pc-MRI data with maximum errors of 13.94%, 13.66%, and 55.39% in subjects 1-3, respectively. The largest differences were observed in subject 3 using the allometric-based strategy.

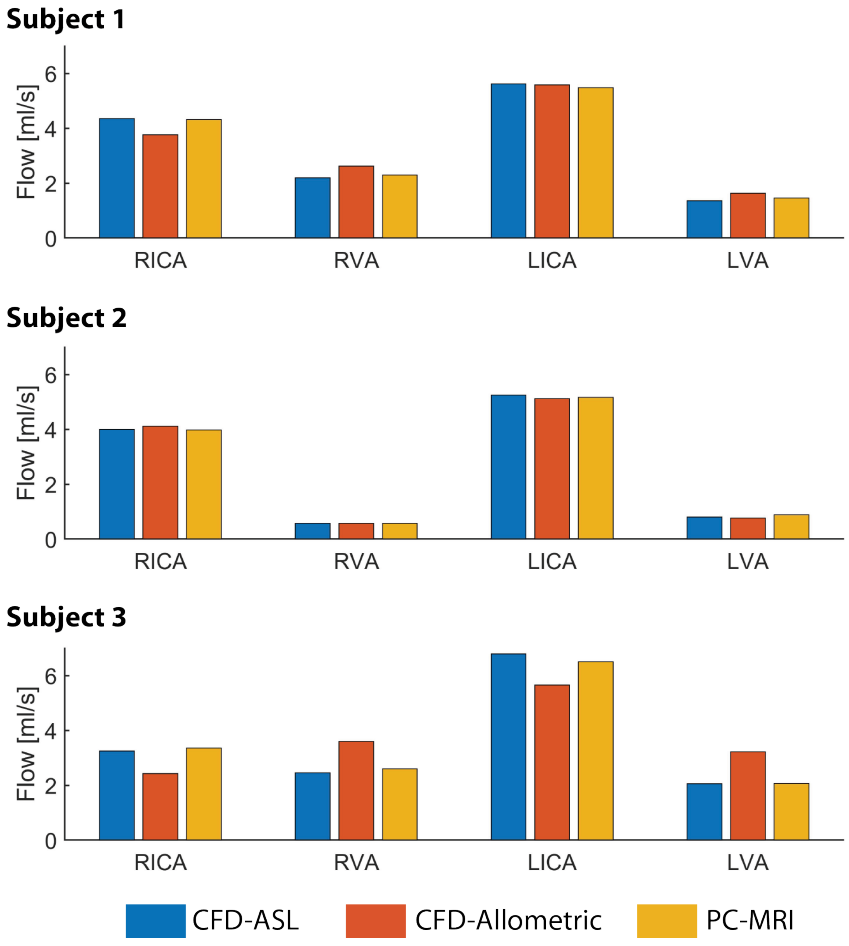

Fig. 5.3 Comparison of mean flow rates in the neck arteries above the carotid bifurcation for subjects 1-3. The mean flow rates of the ASL-based and allometric-based calibrated CFD validated against the mean flow rates obtained from PC-MRI. RICA = right internal carotid artery, LICA = left internal carotid artery, RVA = right vertebral artery, LVA = left vertebral artery.

5.3.2 Flow comparison in CoW arteries

A comparison of the mean flow rates in the cerebral arteries obtained from the ASL-based and allometric-based calibrated CFD analyses are shown in Fig. 5.4. The two calibration strategies

resulted in significantly different mean flow distributions in the CoW. The ASL-based calibrated CFD analyses resulted in an overall symmetric flow distribution between hemispheres with a difference between right and left MCA of 2.30%, 3.66%, and 4.58% for subjects 1-3. In contrast, the allometric-based calibrated CFD analyses resulted in flow differences between right and left MCA of 26.86%, 24.51%, and 47.44% for subjects 1-3. A similar trend was observed in the ACA and PCA territories. Furthermore, the allometric-based calibration resulted in a consistently higher flow to the posterior circulation (right and left PCA combined) compared to the ASL-based calibration, with an average difference of 44.95%, 49.88%, and 117.20% for subjects 1-3. Conversely, the allometric-based calibration resulted in consistently lower flow to the MCA territories (right and left MCA combined) compared to the ASL-based calibration, with an average difference of 18.55%, 25.41%, and 36.36%.

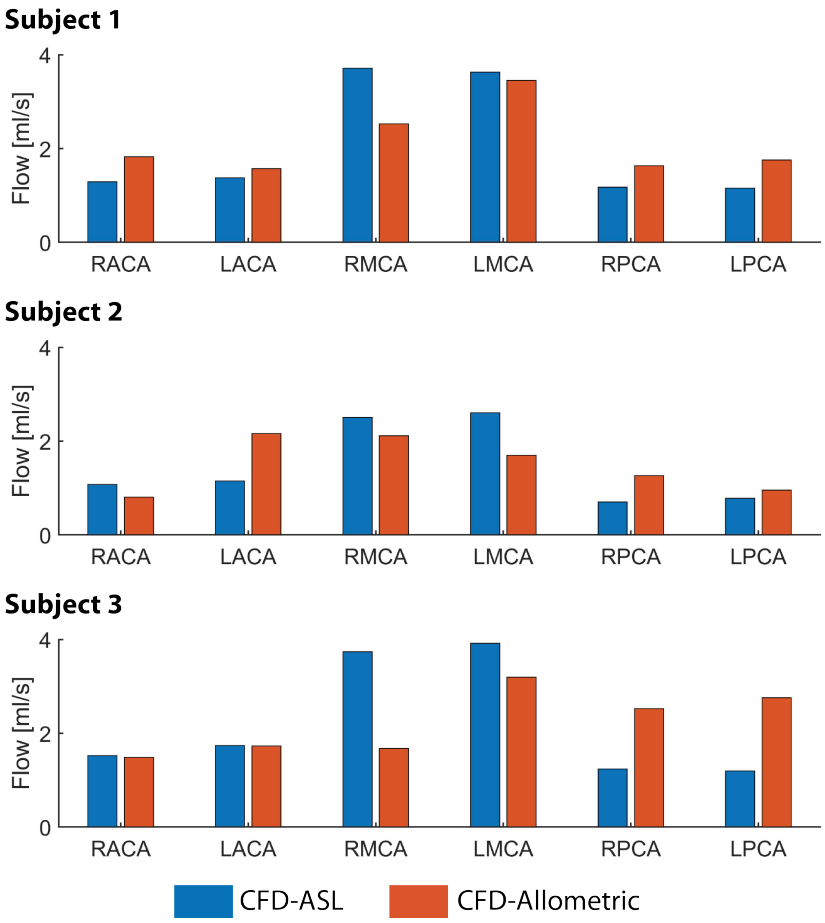

Fig. 5.4 Comparison of mean flow rates in the cerebral arteries of the CoW for subjects 1-3 between the ASL-based and allometric-based calibrated CFD. RACA = right anterior cerebral artery, LACA = left anterior cerebral artery, RMCA = right middle cerebral artery, LMCA = left middle cerebral artery, RPCA = right posterior cerebral artery, LPCA = left posterior cerebral artery.

5.3.3 Fractional blood supply comparison in CoW

The FBS obtained with the ASL-based CFD resulted in an overall good match with the FBS obtained from vessel-selective ASL (Fig. 5.5). The FBS obtained from the allometric-based CFD analysis resulted in similar FBS values as the ASL-based CFD in territories primarily perfused by a single neck artery but lead to large differences in territories perfused by multiple neck arteries. These differences were most noticeable in the RACA, which received mixed contributions from the ipsilateral RICA and the contralateral LICA in all 3 subjects. Based on the FBS obtained from vessel-selective ASL, the RICA contributed 50.07%, 51.36%, and 7.21% to the RACA in subjects 1-3. In the ASL-based CFD analysis, the ipsilateral flow contributions to the RACA resulted in 51.91%, 79.95%, and 14.7% in subjects 1-3. In contrast, the allometric-based CFD analysis resulted in flow contributions of 66.77%, 92.35%, and 71.24% to the RACA in subjects 1-3. The allometric-based calibration was unable to capture the collateral flow compensation accurately, especially in the subject 3, who had the highest amount of collateral flow due to the severe stenosis.

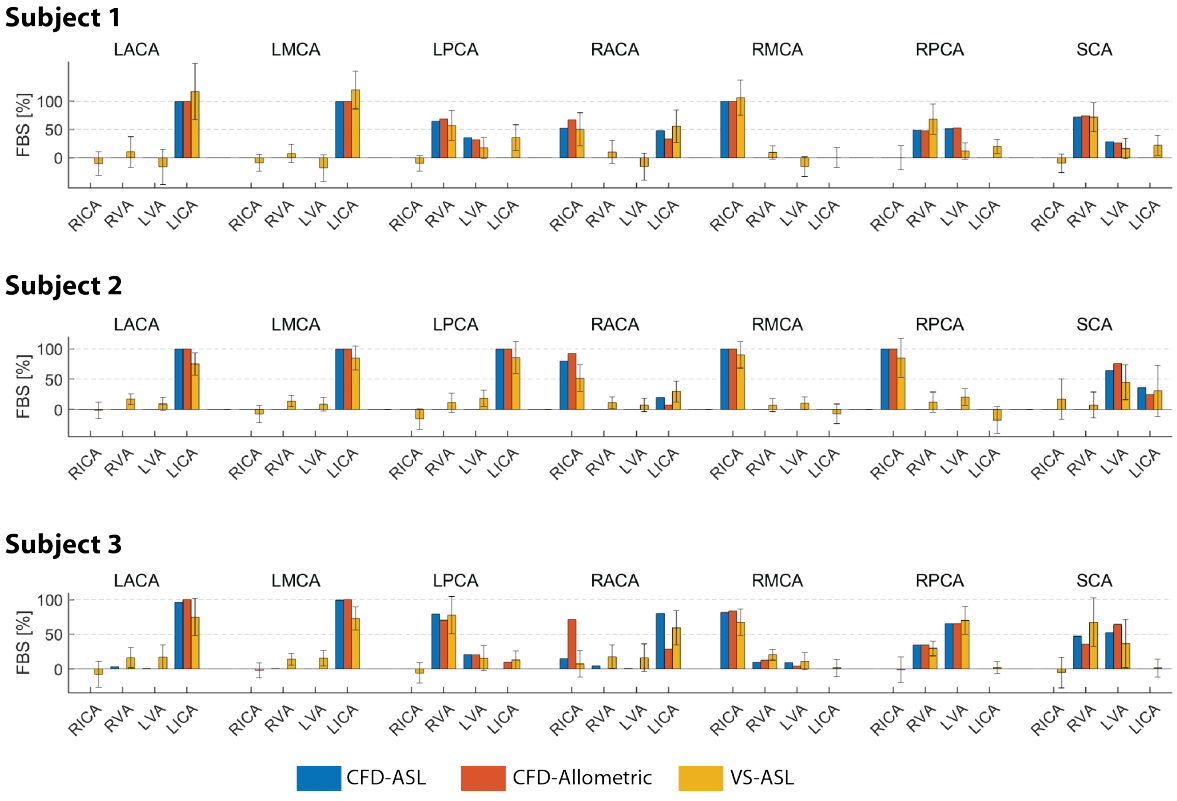

Fig. 5.5 Fractional blood supply (FBS) in the main intracranial territories. FBS was obtained from the ASL-based CFD and allometric-based CFD in combination with LPT and compare to the FBS obtained from VS-ASL. For VS-ASL, values of FBS represent the median of the FBS distribution in each vascular territory. The error bar represents the median absolute deviation. For

CFD, values of FBS were calculated based on the particle count at each outlet of the CoW. RACA/LACA = right/left anterior cerebral artery, RMCA/LMCA = right/left middle cerebral artery, RPCA/LPCA = right/left posterior cerebral artery, SCA = superior cerebellar arteries, RVA/LVA = right/left vertebral artery, RICA/LICA = right/left internal carotid artery.

To further evaluate the match between the FBS obtained from the two CFD analyses and VS-ASL, the correlation over all intracranial territories and labeled neck arteries was calculated for each subject. Fig. 5.6 shows a scatter plot of the FBS and the linear fit for each subject. Overall good correlation between both CFD calibration strategies and VS-ASL was achieved. However, the ASL-based calibration consistently outperformed the allometric-based calibration. The difference in correlation coefficient was most significant in subject 3.

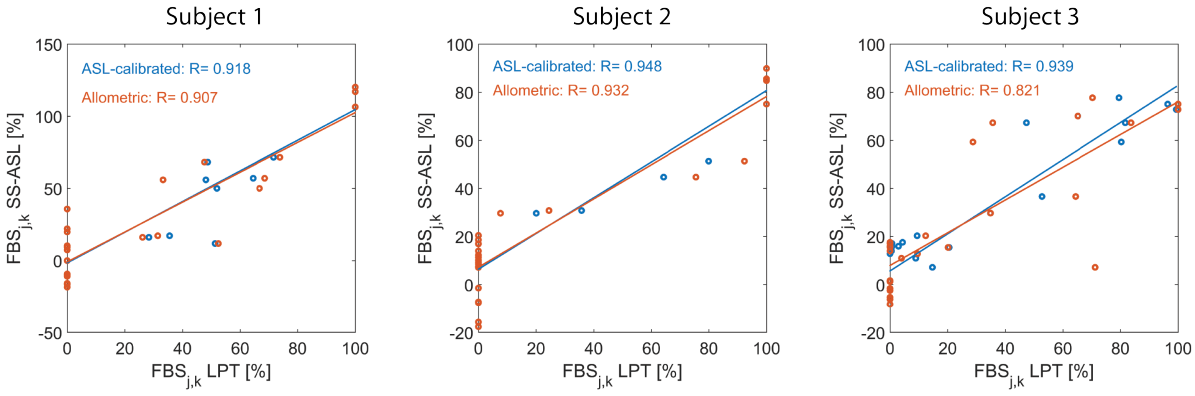

Fig. 5.6 Correlation between the FBS obtained from CFD and VS-ASL for both ASL-based and allometric-based calibrations. For each subject, the correlation coefficient and linear fit of FBS over all territories and neck arteries was calculated.

Fig. 5.7 shows a comparison of the blood supply in the CoW of subject 3 using LPT for the ASL-based CFD and the allometric-based CFD analyses. In the ASL-based CFD analysis, the RACA was predominately supplied by the LICA (blue particle), which was also apparent in the vessel-selective ASL data (see Fig. 5.5 bar plots of FBS). In contrast, the allometric-based CFD analysis resulted in the RACA being predominately supplied by the ipsilateral RICA (green particles) with only a small collateral flow contribution from the LICA. Furthermore, in the ASL-based CFD analysis, flow in the left posterior communication artery (arrow) was transporting vertebral particles (red, yellow) from the posterior circulation to the anterior circulation. In the allometric-based CFD analysis, the flow direction was reversed and LICA particles (blue) were supplied to the posterior circulation.

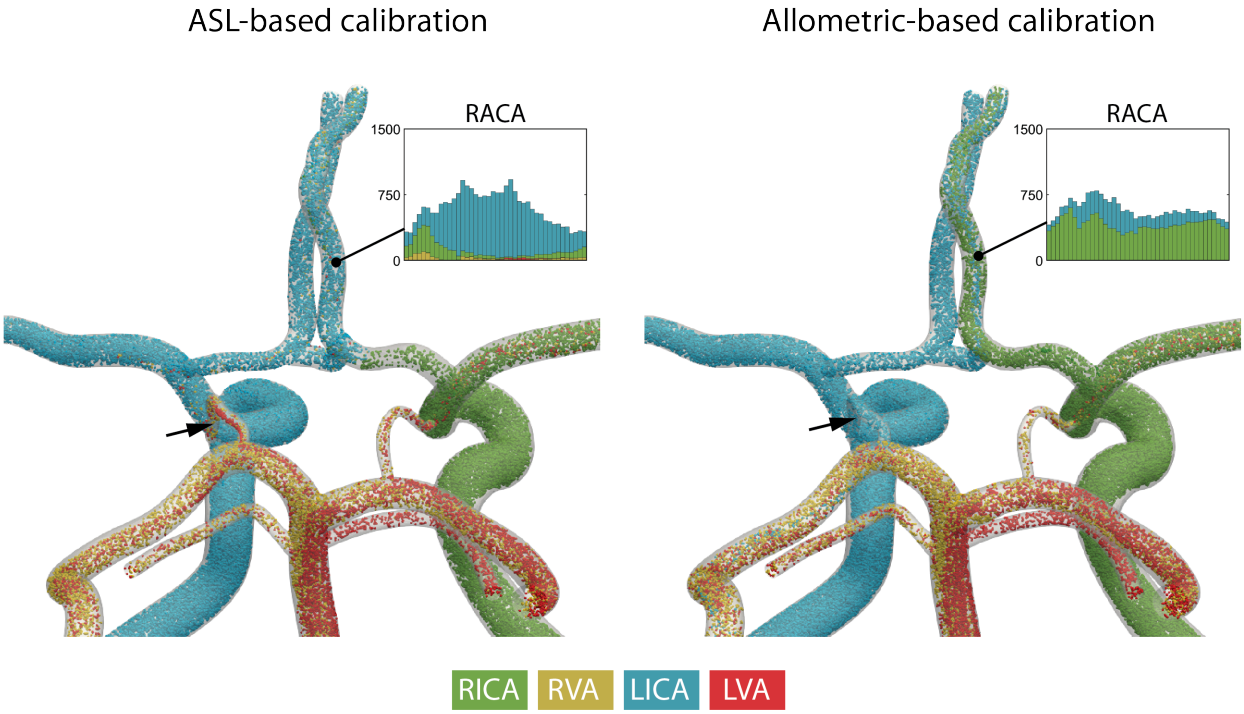

Fig. 5.7 Comparison of the blood supply in the CoW of subject 3 for the ASL-based and allometric-based CFD analysis in combination with LPT. The particles were color-coded based on the originating cervical artery. Histograms show the particle count over a full cardiac cycle at the RACA. Arrows indicate the left posterior communicating artery.

5.4 Discussion

Image-based CFD is becoming an increasingly popular method of non-invasively quantifying cerebral hemodynamics. Clinical applications of CFD have included hemodynamic assessment of cerebral aneurysm [43][44][45] intracranial stenosis [41][42]. To provide clinically meaningful results with CFD analysis, patient-specific computational models are needed. Unfortunately, the word “patient-specific” is not well-defined in CFD modeling and different interpretations have been used in the literature. In general, there has not been a consensus on what constitutes as a patient-specific CDF model of cerebral hemodynamics.

Previous studies have used a wide range of outflow boundary conditions, ranging from directly assigning flow or pressure [107][106][109] to lumped parameter models of the distal vasculature, including Windkessel models [105][75]. The calibration of outflow boundary conditions has also varied significantly between studies and has included strategies based on literature data [111] [108], allometric-scaling [77][75], and in-vivo data [90][112]. Yet, the impact of these modeling assumptions on cerebral hemodynamics is not well studied. The goal of this work was to

investigate the impact of boundary conditions parameter calibration on cerebral hemodynamics in patients with carotid stenosis.

We evaluated the performance of two strategies, an ASL-based and allometric-based, for the calibration of intracranial outflow boundary conditions in 3 subjects with varying degrees of stenosis. The comparison of mean flow rates in the neck arteries showed good agreement between the ASL-based calibrated CFD analysis and the PC-MRI data. The allometric-based calibrated CFD analysis resulted in larger differences in mean flow rates compared to the PC-MRI data. The amount of error seemed to increase with the amount of collateral flow between the hemispheres rather than the degree of stenosis. In the example of subject 2, flow was relatively symmetric between hemispheres with only minor amounts of collateral flow despite the severe RICA stenosis, which was well captures by both calibration strategies.

The differences in mean flow rates between the two calibration strategies increased significantly at the level of the CoW. The ASL-based calibration estimated an overall higher flow to the MCAs and lower flow to the PCAs compared to the allometric-based calibration. More importantly, the ASL-based calibration resulted in an approximately even flow distribution between right and left hemisphere, which reflects the even distribution of perfusion between hemispheres measured with non-selective ASL. In contrast, the allometric-based calibration resulted in large differences between right and left hemisphere. The main reason for these differences in flow between hemispheres is that the allometric-based calibration does not capture the adaptation (cerebral autoregulation) of the distal vasculature, necessary to maintain flow to the vascular territory. Since the resistances were assigned based on allometric-scaling and kept constant, flow to the territories ipsilateral to the carotid stenosis was reduced. The ASL-based calibration on the other hand captures the changes in the distal vasculature and adapts the resistances accordingly.

Quantification of the fractional blood supply of the main intracranial arteries using Lagrangian particle tracking revealed an overall good match between the ASL-based calibrated CFD and vessel-selective ASL data. Differences in FBS between the ASL-based and allometric-based calibration were most noticeable in vascular territories with mixed supply from multiple brain-supplying arteries. The allometric-based calibration was unable to capture the collateral flow from the LICA to the RICA accurately. With increasing amounts of flow compensation between

hemispheres or asymmetry of blood supply to the brain, the importance of a physiological based calibration strategy becomes increasingly important to capture the true cerebral hemodynamics.

The strategy of outflow boundary condition calibration for CFD models of the cerebral vasculature has historically been driven mainly by the availability of clinical data. While strategies based on allometric scaling or literature-based flow distributions provide easy implementation without the need to acquire flow data, applications in subjects with complex cerebral hemodynamics are limited. The ASL-based calibration strategy on the other hand could capture well the flow in the CoW, in particular the flow compensation between hemispheres. Tissue perfusion imaging captures the adaptation of the distal vascular bed, which is represented by the derived flow split from the imaging data. Furthermore, the ASL-based calibration can detect hypoperfusion in subjects with severe stenosis in combination with exhausted cerebral vascular reserve. However, the ASL-based strategy requires the acquisition of non-selective ASL perfusion images in addition to flow measurements (PC-MRI) and anatomical data (Time-of-Flight MRI). While ASL data is generally not acquired as part of clinical protocols for cerebrovascular disease, the clinical use of ASL in general has been steadily increasing due to its quantitative and non-invasive properties.

5.5 Conclusions

In this work, we compared two outflow boundary condition calibration strategies, an ASL-based and an allometric-based, for CDF modeling of cerebral blood flow. The ASL-based calibrated CFD analysis captured the flow compensation between hemispheres as measured with vessel-selective ASL and overall lead to an approximately symmetrical flow distribution in the CoW in all three subjects. In contrast, the allometric-based calibrated CFD analysis was unable to capture the collateral flow compensation, which resulted in large differences in flow between hemispheres. Due to the assignment of distal resistance at the intracranial outflow boundary conditions based on the cross-sectional outflow area in the allometric-based calibration, the adaptation of the distal vasculature (cerebral autoregulation) is not accounted for. The ASL-based calibration accounts for the adaptation of the distal vasculature by deriving a flow split across the main intracranial arteries based on brain tissue perfusion measurements, which allows to capture the complex cerebral hemodynamics in patients with carotid stenosis.

Chapter 6: Discussion and Future Work

6.1 General discussion

In this thesis, we developed a novel strategy to characterize cerebral hemodynamics in patients with carotid stenosis. This project was motivated by the complexity of the cerebral vasculature and its ability to compensate flow in the presence of cerebrovascular disease. Cerebral hemodynamics vary significantly among patients due to differences in vascular anatomy, cerebral vascular flow reserve, and disease progression. Cerebral hemodynamics are known to play a major role in the pathophysiology of cerebrovascular disease and the risk of ischemic stroke. Yet, clinically available imaging tools only provide a limited snapshot of cerebral hemodynamics and flow compensation. In this project, we used CFD in combination with ASL perfusion imaging to model cerebral hemodynamics non-invasively and with high spatial and temporal resolution.

We first implemented a vessel-selective PCASL sequence on a 3T MRI system to measure the perfusion territories of the brain-supplying arteries in the neck. The acquisition of vessel-selective PCASL images is challenging due to a reduction in labeling efficiency compared to non-selective PCASL labeling schemes. To maximize labeling efficiency and improve overall image quality, we investigated the effects of off-resonance, pulsatility, and vessel movement in a group of 10 healthy subjects. We found that the use of a multi-phase off-resonance calibration pre-scan significantly improved the labeling efficiency compared to the uncalibrated vessel-selective perfusion scan and is worth the extra scan time. To reduce the effects of pulsatility during the image acquisition, we also investigated the application of a cardiac-triggering scheme. While there was a statistically significant increase in CNR, overall impact of cardiac-triggering on image quality was small. Lastly, we examined the effects of vessel movement on labeling efficiency and found a threshold of 2mm based on simulation. In-vivo, we found that 50% of the subjects had more than 2mm movement in at least one of the neck arteries during MRI protocol, demonstrating the importance of frequently measuring the vessel location within the labeling plane during the protocol.

Next, we modeled the hemodynamics in the large cervical and cerebral arteries using CFD analysis. To overcome the limitations of using allometric-scaling approaches or literature-based flow distributions to specify outflow boundary conditions, commonly used in CFD studies, we developed a patient-specific calibration strategy using ASL perfusion data. We estimated the flow distribution in the main intracranial territories using non-selective PCASL images in combination with a vascular territory atlas and flow data in the neck arteries. We then calibrated the outflow boundary conditions to match the estimated flow distribution in the CFD model. Validation of the FBS obtained from CFD LPT in 3 subject models (one healthy subject and two patients with carotid stenosis) against FBS measurements derived from vessel-selective PCASL resulted in an overall good match. The CFD model was able to reproduce the collateral flow observed in the anterior territory and the mixing of vertebral flow in the posterior circulation.

To further analyze our patient-specific calibration strategy, we performed additional CFD analyses in the same subject models but using an allometric-scaling approach to calibrate intracranial outflow boundary conditions. The comparison showed that the allometric-based calibrated CFD model was unable to accurately capture the collateral flow between hemispheres correctly. In contrast to the allometric-based calibration, the ASL-based calibration accounts for the adaptation of the distal vasculature to maintain cerebral blood flow, which is needed to accurately capture the flow compensation in the CoW.

The feasibility of our proposed CFD-ASL modeling strategy to assess cerebral hemodynamics in patients with carotid stenosis and to gain clinically relevant information was demonstrated in two preoperative patient examples. Despite similar severity of the RICA stenosis, large differences in cerebral hemodynamics and flow compensation were observed. Additional to a calibrated velocity field, The CFD models produced an absolute pressure distribution, which is not clinically available. The pressure gradient over the stenosis revealed important information about the hemodynamic impact of the stenosis, which was not captured by a anatomical-based assessment alone. We further investigated the changes in hemodynamics following revascularization in one patient example. Due to the minor hemodynamic impact of the stenosis preoperatively, the hemodynamics did not change significantly postoperatively. This patient illustrated an example where the anatomical assessment indicated a severe stenosis but the CFD analysis revealed only a

minor hemodynamic impact. While further studies are necessary, this examples illustrates the importance of a hemodynamic assessment.

6.2 Future work

In the future, we want to expand our clinical study and include more patients with carotid stenosis. One of the main limitations of our work was the small sample size of the study. While we were able to demonstrate the feasibility and validity of our combined computational and imaging modeling strategy, we were unable to draw general conclusions about the patient population. With a larger sample size, we could investigate the relationship between anatomical variations, stenosis severity, and collateral flow patterns. A detailed analysis of cerebral hemodynamics in a large group of patients could help to identify new clinical metrics to better stratify patients for revascularization.

Another future application of our CFD-ASL modeling strategy is the assessment of the relation between embolism source and embolus distribution to the CoW in patients with embolic stroke. Stroke is a heterogeneous clinical entity with various different pathophysiologic mechanisms including large vessel atherosclerosis, cardioembolism and small vessel disease. Optimal secondary stroke prevention would select preventive therapy based on a clear understanding of disease mechanism. Yet, even after thorough diagnostic evaluation, the cause of embolic stroke remains uncertain (cryptogenic) in one third of cases [104]. It is relatively common that multiple separate pathophysiologic mechanisms may be identified in the same patient. For example, an apparently small vessel (i.e. lacunar) infarct may be identified on imaging, but accompanied by a moderate stenosis in the perfusing carotid and/or a high risk cardioembolic source. A key question to answer is thus: Given the location of the infarction, what is the most likely path the embolus traveled? The transport of emboli from the cervical arteries to the CoW has previously been studied using CFD analysis [76][113]. However, the scope of these previous studies was limited to assessing the impact of emboli size, shape, and density on the distribution across the CoW arteries. While the CFD analysis was performed in geometric models derived from anatomical data, boundary conditions were not calibrated patient-specifically. Based on the findings in our study, the specification of boundary conditions has a profound impact on the flow distribution in the CoW and therefore the transport of emboli. Out proposed ASL-based calibration strategy could be used to further assess the transport of emboli in a patient-specific setting. To achieve this goal, further

technical developments would be needed on the particle tracking code (e.g. inclusion of mass properties).

Lastly, our computational model of cerebral blood flow could be extended to include models of cerebral autoregulation. Our current CFD model consists of static boundary conditions which allow us to only match the patient's hemodynamic state at the time of the data acquisition. The effects of autoregulatory control on the distal vasculature and the resulting cerebral blood flow are indirectly captured in our strategy by acquiring tissue perfusion images. However, it would be very useful to predict the autoregulatory response of the distal vasculature and the changes in cerebral hemodynamics following revascularization solely on preoperative imaging data. To achieve this goal, a set of new boundary condition models need to be implemented that allow the dynamic adaptation of the distal resistance based on the autoregulatory response curve and the remaining vascular flow reserve. We previously implemented a lumped parameter model (0D) of cerebral blood flow regulation to study the effects of carotid endarterectomy on collateral flow [114]. A 0D parameter model based on Poiseuille's Law was implemented to account for the large cerebral arteries, arterioles, venous side, and cerebrospinal fluid circulation. The 0D-model was coupled to a phenomenological-based autoregulation model to dynamically adapt the vessel properties of the small arteries based on changes in cerebral blood flow. The next step would be to couple our patient-specific 3D model of cerebral blood flow to the lumped parameter model of cerebral autoregulation. The netlist functionality in CRIMSON provides a framework to include the dynamic control of lumped parameter models. This functionality was used in this work to calibrate boundary condition parameters dynamically during simulation runtime and could be adapted to model the autoregulatory response.

Bibliography

[1] Alpers BJ, Berry RG, Paddison RM. Anatomical studies of the circle of Willis in normal brain. *Arch Neurol Psychiatry* 1959; 81: 409.

[2] Roger VL, Go AS, Lloyd-Jones DM, et al. Heart Disease and Stroke Statistics—2011 Update. *Circulation* 2011; 123: 18–209.

[3] Selby, Joe V., Friedman, Gary D., Quesenberry Charles P., Weiss NS. Beneficial Effect of Carotid Endarterectomy in Symptomatic Patients with High-Grade Carotid Stenosis. *N Engl J Med* 1991; 325: 445–453.

[4] Warlow C. MRC European Carotid Surgery Trial: interim results for symptomatic patients with severe (70-99%) or with mild (0-29%) carotid stenosis. European Carotid Surgery Trialists' Collaborative Group. *Lancet (London, England)* 1991; 337: 1235–43.

[5] Mayberg MR, Wilson SE, Yatsu F, et al. Carotid endarterectomy and prevention of cerebral ischemia in symptomatic carotid stenosis. Veterans Affairs Cooperative Studies Program 309 Trialist Group. *JAMA* 1991; 266: 3289–94.

[6] Irvine CD, Baird RN, Lamont PM, et al. Endarterectomy for asymptomatic carotid artery stenosis. *BMJ* 1995; 311: 1113–1114.

[7] Halliday A, Mansfield A, Marro J, et al. Prevention of disabling and fatal strokes by successful carotid endarterectomy in patients without recent neurological symptoms: randomised controlled trial. *Lancet* 2004; 363: 1491–1502.

[8] Brott TG, Hobson RW, Howard G, et al. Stenting versus Endarterectomy for Treatment of Carotid-Artery Stenosis. *N Engl J Med* 2010; 363: 11–23.

[9] Felberg RA, Christou I, Demchuk AM, et al. Screening for intracranial stenosis with transcranial doppler: The accuracy of mean flow velocity thresholds. *J Neuroimaging* 2002; 12: 9–14.

[10] Best LMJ, Webb AC, Gurusamy KS, et al. Transcranial Doppler Ultrasound Detection of Microemboli as a Predictor of Cerebral Events in Patients with Symptomatic and Asymptomatic Carotid Disease: A Systematic Review and Meta-Analysis. *Eur J Vasc Endovasc Surg* 2016; 52: 565–580.

[11] Sarkar S, Ghosh S, Ghosh SK, et al. Role of transcranial Doppler ultrasonography in stroke. *Postgrad Med J* 2007; 83: 683–689.

[12] Russell SM, Woo HH, Siller K, et al. Evaluating middle cerebral artery collateral blood flow reserve using acetazolamide transcranial Doppler ultrasound in patients with carotid occlusive disease. *Surg Neurol* 2008; 70: 466–470.

[13] Schnell S, Ansari SA, Vakil P, et al. Three-dimensional hemodynamics in intracranial aneurysms: influence of size and morphology. *J Magn Reson Imaging* 2014; 39: 120–131.

[14] Hope TA, Hope MD, Purcell DD, et al. Evaluation of intracranial stenoses and aneurysms with accelerated 4D flow. *Magn Reson Imaging* 2010; 28: 41–46.

[15] Chang W, Loecher MW, Wu Y, et al. Hemodynamic Changes in Patients with Arteriovenous Malformations Assessed Using High-Resolution 3D Radial Phase-Contrast MR Angiography. *Am J Neuroradiol* 2012; 33: 1565–1572.

[16] Wu C, Schnell S, Vakil P, et al. In Vivo Assessment of the Impact of Regional Intracranial Atherosclerotic Lesions on Brain Arterial 3D Hemodynamics. *Am J Neuroradiol* 2017; 38: 515–522.

[17] Vali A, Aristova M, Vakil P, et al. Semi-automated analysis of 4D flow MRI to assess the hemodynamic impact of intracranial atherosclerotic disease. *Magn Reson Med* 2019; 82: 749–762.

[18] Lu L, Zhang LJ, Poon CS, et al. Digital Subtraction CT Angiography for Detection of Intracranial Aneurysms: Comparison with Three-dimensional Digital Subtraction Angiography. *Radiology* 2012; 262: 605–612.

[19] Vinuela F. Comments , Opinions , and Reviews Digital Subtraction Angiography : Current Clinical Applications. 1985; 528–537.

[20] Awad I, Little JR, Modic MT, et al. Intravenous digital subtraction angiography: An index of collateral cerebral blood flow in internal carotid artery occlusion. *Stroke* 1982; 13: 469–472.

[21] Bokkers RPH, Hernandez DA, Merino JG, et al. Whole-Brain Arterial Spin Labeling Perfusion MRI in Patients With Acute Stroke. *Stroke* 2012; 43: 1290–1294.

[22] Wang DJJ, Alger JR, Qiao JX, et al. The value of arterial spin-labeled perfusion imaging in acute ischemic stroke: Comparison with dynamic susceptibility contrast-enhanced MRI. *Stroke* 2012; 43: 1018–1024.

[23] Zaharchuk G, El Mogy IS, Fischbein NJ, et al. Comparison of Arterial Spin Labeling and Bolus Perfusion-Weighted Imaging for Detecting Mismatch in Acute Stroke. *Stroke* 2012; 43: 1843–1848.

[24] Benedictus MR, Leeuwis AE, Binnewijzend MAA, et al. Lower cerebral blood flow is associated with faster cognitive decline in Alzheimer's disease. *Eur Radiol* 2017; 27: 1169–1175.

[25] Iturria-Medina Y, Sotero RC, Toussaint PJ, et al. Early role of vascular dysregulation on late-onset Alzheimer's disease based on multifactorial data-driven analysis. *Nat Commun* 2016; 7: 11934.

[26] Fernández-Seara MA, Mengual E, Vidorreta M, et al. Cortical hypoperfusion in Parkinson's disease assessed using arterial spin labeled perfusion MRI. *Neuroimage* 2012; 59: 2743–2750.

[27] Wong EC, Buxton RB, Frank LR. A theoretical and experimental comparison of continuous and pulsed arterial spin labeling techniques for quantitative perfusion imaging. *Magn Reson Med* 1998; 40: 348–355.

[28] Dai W, Garcia D, De Bazelaire C, et al. Continuous flow-driven inversion for arterial spin labeling using pulsed radio frequency and gradient fields. *Magn Reson Med* 2008; 60: 1488–1497.

[29] Hartkamp NS, Bokkers RPH, Van Der Worp HB, et al. Distribution of cerebral blood flow in the caudate nucleus, lentiform nucleus and thalamus in patients with carotid artery stenosis. *Eur Radiol* 2011; 21: 875–881.

[30] Hendrikse J, Petersen ET, van Laar PJ, et al. Cerebral Border Zones between Distal End Branches of Intracranial Arteries: MR Imaging. *Radiology* 2008; 246: 572–580.

[31] Wong EC. Vessel-encoded arterial spin-labeling using pseudocontinuous tagging. *Magn Reson Med* 2007; 58: 1086–1091.

[32] Helle M, Norris DG, Rüfer S, et al. Superselective pseudocontinuous arterial spin labeling. *Magn Reson Med* 2010; 64: 777–786.

[33] Dai W, Robson PM, Shankaranarayanan A, et al. Modified pulsed continuous arterial spin labeling for labeling of a single artery. *Magn Reson Med* 2010; 64: 975–982.

[34] Abdi M, Karimi A, Navidbakhsh M, et al. Modeling the Circle of Willis Using Electrical Analogy Method under both Normal and Pathological Circumstances. *J Biomed Phys Eng* 2013; 3: 45–56.

[35] Zhang C, Wang L, Li X, et al. Modeling the circle of Willis to assess the effect of anatomical variations on the development of unilateral internal carotid artery stenosis. *Biomed Mater Eng* 2014; 24: 491–499.

[36] Olufsen M, Tran H, Ottesen J. Modeling Cerebral Blood Flow Control During Posture Change from Sitting to Standing. *Cardiovasc Eng* 2004; 4: 47–58.

[37] Alastruey J, Parker KH, Sherwin SJ. Arterial pulse wave haemodynamics. *11th Int Conf Press Surges* 2012; 401–443.

[38] de Lancea CL, David T, Alastruey J, et al. Recruitment Pattern in a Complete Cerebral Arterial Circle. *J Biomech Eng* 2015; 137: 1–11.

[39] Alastruey J, Moore SM, Parker KH, et al. Reduced modelling of blood flow in the cerebral circulation: Coupling 1-D, 0-D and cerebral auto-regulation models. *Int J Numer Methods Fluids* 2008; 56: 1061–1067.

[40] Melis A, Moura F, Larrabide I, et al. Improved biomechanical metrics of cerebral vasospasm identified via sensitivity analysis of a 1D cerebral circulation model. *J Biomech* 2019; 90: 24–32.

[41] Liu J, Yan Z, Pu Y, et al. Functional assessment of cerebral artery stenosis: A pilot study based on computational fluid dynamics. *J Cereb Blood Flow Metab* 2017; 37: 2567–2576.

[42] Leng X, Scalzo F, Ip HL, et al. Computational fluid dynamics modeling of symptomatic

intracranial atherosclerosis may predict risk of stroke recurrence. *PLoS One* 2014; 9: 1–8.

[43] Castro MA, Putman CM, Cebral JR. Computational fluid dynamics modeling of intracranial aneurysms: Effects of parent artery segmentation on intra-aneurysmal hemodynamics. *Am J Neuroradiol* 2006; 27: 1703–1709.

[44] Raschi M, Mut F, Byrne G, et al. CFD and PIV Analysis of Hemodynamics in a Growing Intracranial Aneurysm. *Int j numer method biomed eng* 2012; 28: 214–228.

[45] Rayz VL, Boussel L, Acevedo-Bolton G, et al. Numerical Simulations of Flow in Cerebral Aneurysms: Comparison of CFD Results and In Vivo MRI Measurements. *J Biomech Eng* 2008; 130: 1–9.

[46] Richter X V, Helle XM, Osch XMJP Van, et al. MR Imaging of Individual Perfusion Reorganization Using Superselective Pseudocontinuous Arterial Spin-Labeling in Patients with Complex Extracranial Steno-Occlusive Disease. *AJNR Am J Neuroradiol* 2017; 38: 703–711.

[47] Van Laar PJ, Hendrikse J, Mali WPTM, et al. Altered flow territories after carotid stenting and carotid endarterectomy. *J Vasc Surg* 2007; 45: 1155–1161.

[48] Yaghi S, Bernstein RA, Passman R, et al. Cryptogenic Stroke: Research and Practice. *Circ Res* 2017; 120: 527–540.

[49] Kaufmann TJ, Huston J, Mandrekar JN, et al. Complications of Diagnostic Cerebral Angiography. *Radiology* 2007; 243: 812–819.

[50] Alsop DC, Detre JA, Golay X, et al. Recommended implementation of arterial spin-labeled perfusion MRI for clinical applications: A consensus of the ISMRM perfusion study group and the european consortium for ASL in dementia. *Magn Reson Med* 2014; 116: 102–116.

[51] Liebeskind DS. Collateral Circulation. Epub ahead of print 2003. DOI: 10.1161/01.STR.0000086465.41263.06.

[52] Zeng J, Fan Y. Correlation Between the Integrity of the Circle of Willis and the Severity of Initial Noncardiac Cerebral Infarction and Clinical Prognosis. 2016; 95: 1–7.

[53] Helle M, Rüfer S, Van Osch MJP, et al. Superselective arterial spin labeling applied for flow territory mapping in various cerebrovascular diseases. *J Magn Reson Imaging* 2013; 38: 496–503.

[54] Lin T, Lai Z, Lv Y, et al. Effective collateral circulation may indicate improved perfusion territory restoration after carotid endarterectomy. *Eur Radiol* 2017; 1–9.

[55] Kaczmarz S, Griese V, Preibisch C, et al. Increased variability of watershed areas in patients with high-grade carotid stenosis. *Neuroradiology* 2018; 60: 311–323.

[56] Okell TW, Schmitt P, Bi X, et al. Optimization of 4D vessel-selective arterial spin labeling angiography using balanced steady-state free precession and vessel-encoding. *NMR Biomed* 2016; 29: 776–786.

[57] Jahanian H, Noll DC, Hernandez-Garcia L. B0 field inhomogeneity considerations in pseudo-continuous arterial spin labeling (pCASL): effects on tagging efficiency and

correction strategy. *NMR Biomed* 2011; 24: 1202–1209.

[58] Luh WM, Talagala SL, Li TQ, et al. Pseudo-continuous arterial spin labeling at 7 T for human brain: Estimation and correction for off-resonance effects using a Prescan. *Magn Reson Med* 2013; 69: 402–410.

[59] Jung Y, Wong EC, Liu TT. Multiphase pseudocontinuous arterial spin labeling (MP-PCASL) for robust quantification of cerebral blood flow. *Magn Reson Med* 2010; 64: 799–810.

[60] Li Y, Mao D, Li Z, et al. Cardiac-triggered pseudo-continuous arterial-spin-labeling: A cost-effective scheme to further enhance the reliability of arterial-spin-labeling MRI. *Magn Reson Med*; 00. Epub ahead of print 2018. DOI: 10.1002/mrm.27090.

[61] Guo J, Meakin JA, Jezzard P, et al. An optimized design to reduce eddy current sensitivity in velocity-selective arterial spin labeling using symmetric BIR-8 pulses. *Magn Reson Med* 2015; 73: 1085–1094.

[62] Shin DD, Liu TT, Wong EC, et al. Pseudocontinuous arterial spin labeling with optimized tagging efficiency. *Magn Reson Med* 2012; 68: 1135–1144.

[63] Verbree J, van Osch MJP. Influence of the cardiac cycle on pCASL: cardiac triggering of the end-of-labeling. *Magn Reson Mater Physics, Biol Med* 2017; 1–11.

[64] Kansagra AP, Wong EC. Quantitative assessment of mixed cerebral vascular territory supply with vessel encoded arterial spin labeling MRI. *Stroke* 2008; 39: 2980–2985.

[65] Chen Z, Zhang X, Yuan C, et al. Measuring the labeling efficiency of pseudocontinuous arterial spin labeling. *Magn Reson Med* 2017; 77: 1841–1852.

[66] Saba L, Yuan C, Hatsukami TS, et al. Carotid Artery Wall Imaging: Perspective and Guidelines from the ASNR Vessel Wall Imaging Study Group and Expert Consensus Recommendations of the American Society of Neuroradiology. *Am J Neuroradiol* 2018; 39: E9–E31.

[67] Liebeskind DS. Collateral circulation. *Stroke* 2003; 34: 2279–2284.

[68] Liebeskind DS, Feldmann E. Fractional Flow in Cerebrovascular Disorders. *Interv Neurol* 2012; 1: 87–99.

[69] Henderson RD, Eliasziw M, Fox AJ, et al. Angiographically defined collateral circulation and risk of stroke in patients with severe carotid artery stenosis. *Stroke* 2000; 31: 128–132.

[70] Bisschops RHC, Klijn CJM, Kappelle LJ, et al. Collateral flow and ischemic brain lesions in patients with unilateral carotid artery occlusion. *Neurology* 2003; 60: 1435–1441.

[71] Hendrikse J, Hartkamp M, Hillen B, et al. Collateral Ability of the Circle of Willis in Patients With. *Stroke* 2001; 2768–2773.

[72] Ramsay SC, Yeates MG, Lord RS, et al. Use of technetium-HMPAO to demonstrate changes in cerebral blood flow reserve following carotid endarterectomy. *J Nucl Med* 1991; 32: 1382–1386.

[73] Schollenberger J, Figueroa CA, Nielsen JF, et al. Practical considerations for territorial perfusion mapping in the cerebral circulation using super-selective pseudo-continuous arterial spin labeling. *Magn Reson Med* 2020; 83: 492–504.

[74] Jensen-Kondering U, Lindner T, van Osch MJP, et al. Superselective pseudo-continuous arterial spin labeling angiography. *Eur J Radiol* 2015; 84: 1758–1767.

[75] Xiao N, Humphrey JD, Figueroa CA. Multi-scale computational model of three-dimensional hemodynamics within a deformable full-body arterial network. *J Comput Phys* 2013; 244: 22–40.

[76] Mukherjee D, Jani ND, Selvaganesan K, et al. Computational Assessment of the Relation Between Embolism Source and Embolus Distribution to the Circle of Willis for Improved Understanding of Stroke Etiology. *J Biomech Eng* 2016; 138: 81008.

[77] Bockman MD, Kansagra AP, Shadden SC, et al. Fluid Mechanics of Mixing in the Vertebrobasilar System: Comparison of Simulation and MRI. *Cardiovasc Eng Technol* 2012; 3: 450–461.

[78] Arthurs CJ, Khlebnikov R, Melville A, et al. CRIMSON: An open-source software framework for cardiovascular integrated modelling and simulation. *PLOS Comput Biol* 2021; 17: e1008881.

[79] Sahni O, Müller J, Jansen KE, et al. Efficient anisotropic adaptive discretization of the cardiovascular system. *Comput Methods Appl Mech Eng* 2006; 195: 5634–5655.

[80] Vignon-Clementel IE, Figueroa CA, Jansen KE, et al. Outflow boundary conditions for 3D simulations of non-periodic blood flow and pressure fields in deformable arteries. *Comput Methods Biomech Biomed Engin* 2010; 13: 625–640.

[81] Xiao N, Alastruey J, Figueroa CA. A systematic comparison between 1-D and 3-D hemodynamics in compliant arterial models. *Int j numer method biomed eng* 2014; 30: 204–231.

[82] Whiting CH, Jansen KE. A stabilized finite element method for the incompressible Navier-Stokes equations using a hierarchical basis. *Int J Numer Methods Fluids* 2001; 35: 93–116.

[83] Kim DE, Park JH, Schellingerhout D, et al. Mapping the Supratentorial Cerebral Arterial Territories Using 1160 Large Artery Infarcts. *JAMA Neurol*. Epub ahead of print 2018. DOI: 10.1001/jamaneurol.2018.2808.

[84] Arthurs CJ, Lau KD, Asrress KN, et al. A mathematical model of coronary blood flow control: Simulation of patient-specific three-dimensional hemodynamics during exercise. *Am J Physiol - Hear Circ Physiol* 2016; 310: H1242–H1258.

[85] Di Achille P, Tellides G, Figueroa CA, et al. A haemodynamic predictor of intraluminal thrombus formation in abdominal aortic aneurysms. *Proc R Soc A Math Phys Eng Sci* 2014; 470: 20140163.

[86] Van Bakel TM, Arthurs CJ, Van Herwaarden JA, et al. A computational analysis of different endograft designs for Zone 0 aortic arch repair. *Eur J Cardio-thoracic Surg* 2018; 54: 389–396.

[87] Nauta FJH, Lau KD, Arthurs CJ, et al. Computational Fluid Dynamics and Aortic Thrombus Formation Following Thoracic Endovascular Aortic Repair. *Ann Thorac Surg* 2017; 103: 1914–1921.

[88] Suh GY, Les AS, Tenforde AS, et al. Quantification of particle residence time in abdominal aortic aneurysms using magnetic resonance imaging and computational fluid dynamics. *Ann Biomed Eng* 2011; 39: 864–883.

[89] Arzani A, Les AS, Dalman RL, et al. Effect of exercise on patient specific abdominal aortic aneurysm flow topology and mixing. *Int J Numer Meth Biomed Engng* 2014; 4179: 280–295.

[90] Zhang H, Fujiwara N, Kobayashi M, et al. Development of a Numerical Method for Patient-Specific Cerebral Circulation Using 1D–0D Simulation of the Entire Cardiovascular System with SPECT Data. *Ann Biomed Eng* 2016; 44: 2351–2363.

[91] Yamada S, Kobayashi M, Watanabe Y, et al. Quantitative Measurement of Blood Flow Volume in the Major Intracranial Arteries by Using 123I-Iodoamphetamine SPECT. *Clin Nucl Med* 2014; 39: 868–873.

[92] Tariq N, Khatri R. Leptomeningeal collaterals in acute ischemic stroke. *J Vasc Interv Neurol* 2008; 1: 91–5.

[93] Li Y, Li M, Zhang X, et al. Clinical features and the degree of cerebrovascular stenosis in different types and subtypes of cerebral watershed infarction. *BMC Neurol* 2017; 17: 166.

[94] Caplan LR, Hennerici M. Impaired clearance of emboli (washout) is an important link between hypoperfusion, embolism, and ischemic stroke. *Arch Neurol* 1998; 55: 1475–1482.

[95] Schollenberger J, Osborne NH, Hernandez-Garcia L, et al. A combined computational fluid dynamics and MRI Arterial Spin Labeling modeling strategy to quantify patient-specific cerebral hemodynamics in cerebrovascular occlusive disease. *bioRxiv* 2021; 2021.01.21.426887.

[96] Miao Z, Liebeskind DS, Lo W, et al. Fractional Flow Assessment for the Evaluation of Intracranial Atherosclerosis: A Feasibility Study. *Interv Neurol* 2016; 5: 65–75.

[97] Ricotta JJ, Aburahma A, Ascher E, et al. Updated Society for Vascular Surgery guidelines for management of extracranial carotid disease: Executive summary. *J Vasc Surg* 2011; 54: 832–836.

[98] Irvine CD, Baird RN, Lamont PM, et al. Endarterectomy for asymptomatic carotid artery stenosis. *BMJ* 1995; 311: 1113–4.

[99] Halliday A, Mansfield A, Marro J, et al. Prevention of disabling and fatal strokes by successful carotid endarterectomy in patients without recent neurological symptoms: randomised controlled trial. *Lancet (London, England)* 2004; 363: 1491–502.

[100] Tonino PAL, De Bruyne B, Pijls NHJ, et al. Fractional Flow Reserve versus Angiography for Guiding Percutaneous Coronary Intervention. *N Engl J Med* 2009; 360: 213–224.

[101] De Bruyne B, Fearon WF, Pijls NHJ, et al. Fractional Flow Reserve–Guided PCI for Stable

Coronary Artery Disease. *N Engl J Med* 2014; 371: 1208–1217.

[102] Makris GC, Nicolaides AN, Xu XY, et al. Introduction to the biomechanics of carotid plaque pathogenesis and rupture: review of the clinical evidence. *Br J Radiol* 2010; 83: 729–735.

[103] Harloff A. Carotid Plaque Hemodynamics. *Interv Neurol* 2012; 1: 44–54.

[104] Nouh A, Hussain M, Mehta T, et al. Embolic strokes of unknown source and cryptogenic stroke: Implications in clinical practice. *Front Neurol* 2016; 7: 1–16.

[105] Liu X, Gao Z, Xiong H, et al. Three-dimensional hemodynamics analysis of the circle of Willis in the patient-specific nonintegral arterial structures. *Biomech Model Mechanobiol* 2016; 15: 1439–1456.

[106] Reorowicz P, Obidowski D, Klosinski P, et al. Numerical simulations of the blood flow in the patient-specific arterial cerebral circle region. *J Biomech* 2014; 47: 1642–1651.

[107] Ren Y, Chen Q, Li Z-Y. A 3D numerical study of the collateral capacity of the circle of Willis with anatomical variation in the posterior circulation. *Biomed Eng Online* 2015; 14: S11.

[108] Long Q, Luppi L, König CS, et al. Study of the collateral capacity of the circle of Willis of patients with severe carotid artery stenosis by 3D computational modeling. *J Biomech* 2008; 41: 2735–2742.

[109] Berg P, Stucht D, Janiga G, et al. Cerebral Blood Flow in a Healthy Circle of Willis and Two Intracranial Aneurysms: Computational Fluid Dynamics Versus Four-Dimensional Phase-Contrast Magnetic Resonance Imaging. *J Biomech Eng* 2014; 136: 1–9.

[110] Holmgren M, Støverud K-H, Zarrinkoob L, et al. Middle cerebral artery pressure laterality in patients with symptomatic ICA stenosis. *PLoS One* 2021; 16: e0245337.

[111] Neidlin M, Büsen M, Brockmann C, et al. A numerical framework to investigate hemodynamics during endovascular mechanical recanalization in acute stroke. *Int J Numer Methods Biomed Eng* 2016; 32: e02748.

[112] Park CS, Alaraj A, Du X, et al. An efficient full space-time discretization method for subject-specific hemodynamic simulations of cerebral arterial blood flow with distensible wall mechanics. *J Biomech* 2019; 87: 37–47.

[113] Fabbri D, Long Q, Das S, et al. Computational modelling of emboli travel trajectories in cerebral arteries: Influence of microembolic particle size and density. *Biomech Model Mechanobiol* 2014; 13: 289–302.

[114] Schollenberger J, Pfaller M, Figueroa AC. *A lumped parameter model of cerebral blood flow regulation: Applications to simulation of carotid endarterectomy*. Master thesis, University of Michigan, 2015.